The peculiar climates of ultra-hot Jupiters

Arcangeli, J.

Publication date
2020
Document Version
Final published version
License
Other

The peculiar climates
of Ultra-hot Jupiters

Jacob Arcangeli

The peculiar climates of Ultra-hot Jupiters

Jacob Arcangeli

The peculiar climates of Ultra-hot Jupiters

Jacob Arcangeli

Contact: jarcangeli92@gmail.com

The peculiar climates of Ultra-hot Jupiters
Thesis, Anton Pannekoek Institute, Universiteit van Amsterdam

Cover by Imogen Arcangeli (imogen.a@hotmail.co.uk)
Printed by Amsterdam University Press

UNIVERSITY OF AMSTERDAM

ANTON PANNEKOEK
INSTITUTE

The research included in this thesis was carried out at the Anton Pannekoek Institute for Astronomy (API) of the University of Amsterdam. This work was funded by the European Research Council (ERC) under the European Union's Horizon 2020 research and innovation programme (grant agreement no. 679633; Exo-Atmos). This work was also supported by the Amsterdam Academic Alliance (AAA) Program.

The peculiar climates of Ultra-hot Jupiters

ACADEMISCH PROEFSCHRIFT

ter verkrijging van de graad van doctor
aan de Universiteit van Amsterdam
op gezag van de Rector Magnificus
prof. dr. ir. K.I.J. Maex
ten overstaan van een door het College voor Promoties ingestelde
commissie, in het openbaar te verdedigen in de Agnietenkapel
op donderdag 15 oktober 2020, te 16:00 uur

door

Jacob Arcangeli

geboren te Verona

Promotiecommissie:

Promotor(es):	Prof. dr. C. Dominik	Universiteit van Amsterdam
Copromotor(es):	dr. J. M. Désert	Universiteit van Amsterdam
Overige leden:	dr. J. L. Birkby	Universiteit van Amsterdam
	prof. dr. A. de Koter	Universiteit van Amsterdam
	prof. dr. I. A. G. Snellen	Universiteit Leiden
	dr. N. Madhusudhan	Universiteit van Cambridge
	dr Y. Miguel	Universiteit Leiden
	prof. dr. M. van der Klis	Universiteit van Amsterdam
	prof. dr. A. L. Watts	Universiteit van Amsterdam

Faculteit der Natuurwetenschappen, Wiskunde en Informatica

Contents

Chapter 1

Introduction

1.1 Exoplanets

1.1.1 The Earth in Context

One of the ultimate goals of the exoplanet field is to understand life in the universe. Earth is a difficult starting place for this problem: We are familiar with Earth as the only planet known to host life, but we can't know yet whether life is an unusual or common occurrence. To begin with we would like to know if Earth-like planets are commonly formed around other stars, and then whether any of these planets would have the right properties and conditions for life, such as water and a temperate climate. These are the key questions of exoplanet science, tackling the formation, the chemistry, and the climates of planets. We cannot address these questions by studying the Earth alone. Fortunately in the last decade we have come to realize the thousands of exoplanets that surround us in our galaxy. The first of these exoplanets was 51-Pegasi b (Mayor & Queloz, 1995), for which the Nobel Prize has been awarded for its discovery, but since then the list of known exoplanets has exploded in number. This has allowed us to place the Earth in a context of planetary systems, where the work to tackle these key questions is well underway.

1.1.2 Exoplanet Diversity

We know of thousands of exoplanets to date (Figure 1.1), having found that on average every other star hosts a planet (Howard et al., 2012; Dressing & Charbonneau, 2013; Batalha, 2014; Silburt et al., 2015). The sheer volume of planets discovered in and of itself might have been surprising, but what was more unexpected was the nature of the planets that were discovered. While potential Earth analogues have been found around other stars (Anglada-Escudé et al., 2016; Gillon et al., 2016; Ment et al., 2019), the majority of known exoplanets are strikingly different to our own solar system. Two key new populations have emerged within the vast quantity of alien worlds.

The first population was that of the Super-Earths, planets a little more massive the Earth but smaller than Uranus or Neptune. These are now thought to be the most abundant exoplanet population, which by chance or otherwise has no presence around our sun (Borucki et al., 2011; Howard et al., 2012; Morton & Swift, 2014; Batalha, 2014; Petigura et al., 2013, 2018; Fulton et al., 2017; Bryson et al., 2020).

The second discovery was the population of hot, Jupiter-like planets. These are gas giants around the mass of Jupiter but typically found within the orbit of Mercury at temperatures of 1500K ($>1200^{\circ}$C) or more. Hot Jupiters are not as common, found around 1% of sun-like stars (Gould et al., 2006; Howard et al., 2012; Santerne et al., 2012; Wright et al., 2012), but they are among the most easily detected systems and are therefore especially accessible to follow-up studies.

Both these populations were unexpected, and both challenged the models that were able to predict the formation of the solar system to now produce a broader range of architectures. While hot Jupiter systems might seem incomparable to our own solar system, some theories predict that Jupiter was only prevented from migrating inwards beyond the terrestrial planets by the influence of Saturn (Walsh et al., 2011). Until recently, it was widely believed that neither gravitational instability nor core accretion could form gas giants at the close in locations where hot Jupiters were found (Rafikov, 2005, 2006). Hence the conclusion was that hot Jupiters must have formed further from their stars and migrated to their present day orbits. Such migration of massive bodies can alter the structure of the entire planetary system, and it may be that Jupiter's wide orbit is what allowed the Earth to survive the turbulent planet formation process.

1.1.3 Through the lens of atmospheres

Exoplanets that are close-in to their host stars are a new regime for planetary physics. These objects are under intense irradiation, and therefore exist in a temperature and composition regime not seen in the Solar System. The main species present in the optical spectra of these hot exoplanets are refractory elements, these are the alkali metals sodium and potassium, as well as molecules in gas phase such as titanium/vanadium oxides (TiO/VO) and water. Together these key species control the energy budget and evolution of close-in planets.

Determining the physical properties of exoplanet atmospheres, and particularly their composition and vertical profiles, is crucial to understand the origin, nature, and evolution of these objects. Key questions have arisen from exoplanet studies, from the question of the formation scenarios to the question of the nature and origin of atmospheres (Charbonneau et al., 2002; Tinetti et al., 2007; Désert et al., 2009; Snellen et al., 2010; Birkby et al., 2013; Sing et al., 2016). Further questions such as on the deviation from specific stellar elemental abundances (Madhusudhan et al., 2014; Kreidberg et al., 2014b; Tsiaras et al., 2016; Barstow et al., 2017; Fu et al., 2017), the control of the temperature in the deeper atmospheres (Deming et al., 2005; Charbonneau et al., 2005), and the origin of thermal inversions in the deeper atmospheres (Hubeny et al., 2003; Knutson et al., 2008; Désert et al., 2008; Huitson

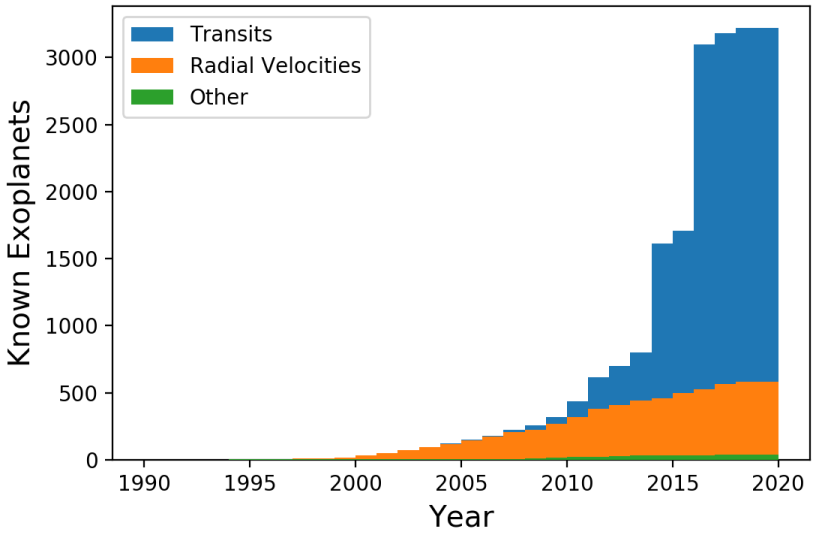

Figure 1.1: Cumulative Histogram of known exoplanets, with the total counts separated by their detection methods at each year. Data taken from TEPCat (Southworth, 2011). The Radial Velocity planets have been detected by their gravitational influence on the motion of their host star through the Doppler effect. Planets found with the Transit method are those that happen to pass between the star they orbit and our line of sight, and are detected by the periodic dimming of their host and are the planets that are focused on in this thesis.

et al., 2012; Diamond-Lowe et al., 2014; Parmentier et al., 2018; Lothringer et al., 2018; Pino et al., 2020) have arise from studies of atmospheres.

Particular highlights from the outstanding questions include understanding the relation between the mass of exoplanets and their atmospheric metallicity as a link to formation (Fortney et al., 2006; Kreidberg et al., 2014b; Wakeford & Sing, 2015), and the influence of clouds on atmosphers and observations (Parmentier et al., 2016; Wakeford et al., 2016). Studying these questions in exoplanets offer an opportunity to detect trends in atmospheric properties (e.g, with temperature, stellar radiation, etc…) and thus to gain a more complete understanding of exoplanet and atmospheric physics.

1.1.4 From formation to atmospheric properties

A key question posed in modern astronomy is how do planets form? In this thesis, we begin to approach this question through the study of close-in giant exoplanet atmospheres. One of the main opportunities afforded by exoplanet atmosphere studies is the chance to constrain theories of planet formation and evolution. This is because the atmospheric composition of a gas-giant contains the fingerprint of its primordial origins. Measuring a planet's atmospheric chemical abundances can therefore help constrain the chemistry, location, and surface den-

sity of solids in the disk where the planet formed, its migration pathway, and even its overall formation mechanism (Lodders, 2004; Mousis et al., 2009, 2012; Öberg et al., 2011; Madhusudhan et al., 2011, 2014; Helled & Lunine, 2014; Marboeuf et al., 2014). Atmospheric water abundance in particular is expected to be an important compositional tracer of planetary origins because water ice is thought to play a major role in planet formation under the core accretion paradigm (Pollack et al., 1996; Owen et al., 1999; Gautier et al., 2001; Guillot & Hueso, 2006; Marboeuf et al., 2008; Johnson et al., 2012; Schoonenberg & Ormel, 2017). However, the water abundance is challenging to determine for the solar system giants because it has mostly condensed out of the observable parts of their relatively cool atmospheres. This puzzle is so important for planet formation theories that the determination of Jupiter's bulk water abundance is a primary goal of the Juno mission, which reached Jupiter in 2016 (Bolton & Bolton, 2010). It is possible to test for the presence of water for the atmospheres of the highly irradiated exoplanets targeted in this thesis because they are much hotter than the solar system planets, and thus the water should be in its gas phase in the observable parts of their atmospheres. Furthermore, theoretical arguments suggest that constituents like water should be well mixed within the photospheres of these planets, and non-equilibrium chemical effects should have a negligible impact on the water abundance (Moses et al., 2011; Parmentier et al., 2013).

Understanding the formation mechanism behind the planets we see can make powerful predictions about their composition and vice-versa. In the case of hot Jupiters, a key question that arises about their formation is how did they reach the close orbits that we find them on? Either they could have formed in-situ, on short orbits, or they could have formed further out before migrating inwards, as we might expect from our own solar system. This range of possible initial positions at which the planet might have formed spans also a range of disk chemistry, due to the temperature of the disk decreasing at increasing radii. In particular one can look at molecules that freeze out of the disk, at what are called ice-lines specific to each molecule, which in the case of H_2O, CO_2, and CO can be traced via the C/O ratio of the planet atmosphere (Figure 1.2, and Öberg et al. 2011; Cridland et al. 2020; Madhusudhan et al. 2016; Madhusudhan 2019 and references therein). Naively for instance, one would expect planets formed close in to have a low C/O ratio, as they would be rich in volatiles such as water and carbon dioxide. However it has been suggested that planets may generally have high C/O ratios (Lodders, 2004; Madhusudhan et al., 2011). In the solar system for example, we are able to do the reverse and estimate the location of the snow line when planetesimal formation took place based on the change in water content of asteroids across the asteroid belt (Martin & Livio, 2012). How the C/O ratio of an exoplanet's atmosphere might be measured is discussed further in Section 1.2.

Formation models for these gas-giant planets typically fall into two broad categories, referred to as core-accretion (Boss 1997, see Durisen et al. 2007 for a review) or gravitational instability models (Perri & Cameron 1974; Pollack et al. 1996, see Chabrier 2014 for a review). Both these theories seek to explain how planets might form from the very early stages of a proto-planetary disk around a star. Gravitational collapse models require some perturbation or instability in the disk to increase the local density enough to trigger a gravitational

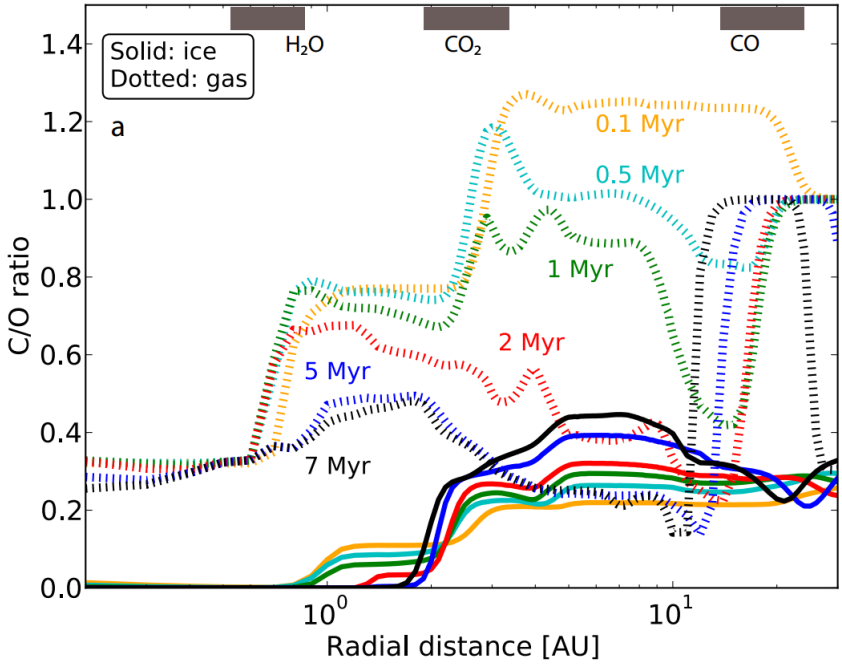

Figure 1.2: C/O ratio of gas and ice as a function of disk radius, shown at different disk ages (from Eistrup et al. 2018). Ice lines are shown by the dark regions at the top of the figure. Here we can see that not only does the location of planet formation in the disk heavily influence the C/O ratio of accreted material, but so does the timing of the planet formation process.

collapse (Toomre, 1964). Core-accretion models instead propose that the core of a planet is built up slowly by aggregating larger dust particles, until it reaches a sufficient mass to gravitationally acrete gas (Lissauer, 1993; Pollack et al., 1996). Core accretion is only likely to occur in the denser regions of the disk, e.g. close in to the star. In the further reaches of the disk we expect only gravitational collapse to be feasible. While it is likely that planets form through a mixture of both of these avenues, there is still great debate over the efficacy of each theory and where each may or may not occur in a disk. A key avenue to distinguishing between these formation pathways is through the signature that each leaves on the newly formed planet's atmosphere, and in particular hot Jupiters are a perfect test case for these theories (Madhusudhan et al., 2014).

1.1.5 Towards brighter stars

While there is a lot of information contained in the atmosphere of an exoplanet, observations of these objects are extremely challenging. Atmospheric signals are, at best 1000x times fainter than the parent star, and close in planets cannot be spatially resolved from their

parents. Hence, even though thousands of exoplanets have been discovered, the number that are amenable to atmospheric studies is much smaller. How accessible a planet is to follow up studies is primarily driven by the host stars brightness, as for faint stars the stellar noise will overwhelm the planet's atmospheric signal. A secondary and similarly important factor is the size of the atmospheric signal, for which hotter and less dense planets are the most favourable for the techniques discussed in this thesis.

After the initial wave of exoplanet detections, dedicated instruments began to come online in order to find the next best and brightest systems, in particular through ground based surveys (WASP: Pollacco et al. 2006; KELT: Pepper et al. 2007, 2012; MASCARA: Snellen et al. 2012). The goal in many cases was to identify targets that were accessible to follow up, and could allow for the testing of atmospheric theories. Surveys to detect transiting exoplanets from the ground typically relied on differential photometry. The differential photometry technique uses a reference star, one of a similar stellar type and brightness, to remove the influence of the Earth's atmosphere on the starlight (e.g. Collier Cameron et al. 2007). This technique has a sweet-spot in target brightness, as nearby stars have no good reference stars close to them on the sky, but more distant stars are increasingly faint. Finally however, a transiting planet detection can only be confirmed after a measurement of it's mass, due to the high incidence of eclipsing binary stars. Mass measurements of exoplanets are typically done via the radial velocity technique, that measures the effect of the planet's mass on the stellar lines via the Doppler effect (Mayor & Queloz, 1995; Marcy & Butler, 1996). In order to obtain accurate planet masses, cooler and therefore less massive stars are preferred as they have more stellar lines with which to measure the Doppler effect. Lastly, the size of the stellar radius is inversely proportional to the smallest planetary signal that can be detected. The upshot of this is that our understanding of more massive and larger stars is much less complete. Hence, most of the newly detected planets were bright but not so bright, and around sun-like or smaller stars.

1.1.6 A new sub-class: the ultra hot Jupiters

There developed a clear gap in the systems observed, as some of the brightest stars which typically have higher masses were not considered ideal candidates for differential photometry. These bright systems were not favourable to exoplanet searches because of a lack of suitable references stars within a restricted field of view. As follow-up studies progressed, such as those of exoplanet atmospheres, it became clear that brighter systems were becoming more and more exciting, as they allowed for further testing of atmospheric theories at a higher precision. Hence, dedicated ground based surveys targetted the brightest stars in our sky using wide fields of view. Examples of these ground based survey such as WASP (Pollacco et al., 2006), KELT (Pepper et al., 2012), MASCARA (Snellen et al., 2012), and HATS (Bakos et al., 2013). Naturally the majority of the bright stars targetted were hot, commonly between F and A type stars, hotter than 6000K and a little more massive than the sun. Among the many classical hot Jupiters, these surveys resulted in a small sub-population of planets being discovered, gas giants on close orbits around hotter and more massive stars (see Figure 1.3). These surveys opened new windows into the exoplanet population, allow-

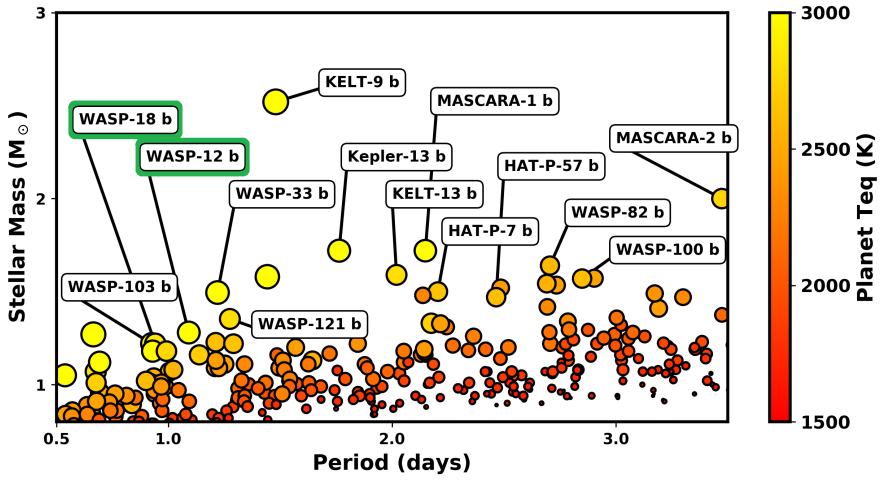

Figure 1.3: Known close-in exoplanets shown against stellar mass. Data from TEPCat (Southworth, 2011). Some key ultra hot Jupiter targets are labelled, and the subjects of this thesis (WASP-12b and WASP-18b) are highlighted in green.

ing for a more comprehensive understanding of planets around stars more massive than the Sun.

These planets discovered around more massive stars also have the hottest dayside temperatures among exoplanets, with the record being held to date by KELT-9b at a dayside temperature of 4500K (Gaudi et al., 2017). Initially these very hot Jupiters were not considered as a separate population, after all they can be considered as the tail end of the hot Jupiter population, and would be expected to have similar formation and evolution histories as their cooler counterparts. Therefore there exists a long history of observations and theory around these planets, before their unique properties were first identified. The first characterizations of these properties are presented in this thesis, the details of which follow in Section 1.4.

1.2 Observing Exoplanet Atmospheres

Many of the bright targets that were discovered remain the perfect candidates for tackling the key questions of planetary science. Atmospheric follow up of key targets is an evolving field, however three main sub-fields have emerged that our outlined below and in Figure 1.4, these are transmission spectroscopy, emission spectroscopy, and phase-curve observations.

1.2.1 Transmission Spectroscopy

Transmission spectroscopy is the most used method to observe exoplanet atmospheres. This technique relies on the primary transit, when the planet passes in front of its stellar host, where the radius of the planet can be measured by the dimming of the stellar light (Char-

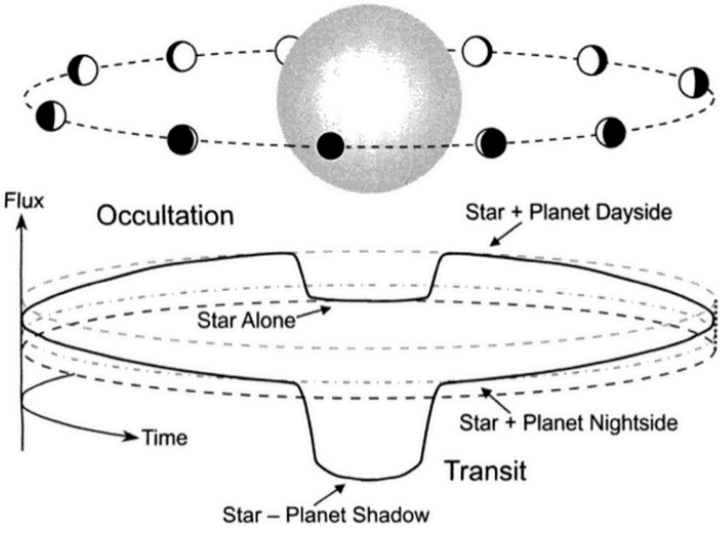

Figure 1.4: Schematic of a full orbit of the planet, demonstrating how the in-eclipse measurement can be used to determine the thermal emission and reflection from the planet. Observations that measure the full orbit of the planet are referred to as phase curves. Image credit: Josh Winn

bonneau et al., 2002; Vidal-Madjar et al., 2003; Tinetti et al., 2007; Swain et al., 2008). Transit depth measurements can be done at multiple wavelengths, producing a transmission spectrum corresponding to the changing transparency of the planet's atmosphere to each wavelength (Sing et al., 2016). The measured spectrum can then be modelled to infer the abundances of key molecules in the atmosphere. While this technique is best suited for hot, puffy atmospheres, it has been successful in targeting cooler planets as well (Bean et al., 2010; Désert et al., 2011a; Berta et al., 2012; Crossfield & Kreidberg, 2017).

1.2.2 Emission Spectroscopy

Emission spectroscopy is the focus of the Chapters presented, as well as its extension in phase curve spectroscopy. Targeting transiting planets, an emission measurement can be obtained by measuring the total flux of the star-planet system inside and outside of secondary eclipse (Deming et al., 2005; Charbonneau et al., 2005; Grillmair et al., 2007). The secondary eclipse is when the planet passes behind the star, and as its light is obscured by the stellar disk what remains is only the star itself. The secondary eclipse can then provide a reference for observations outside of eclipse, with the difference in brightness being due to the emitted or reflected light from the planet.

When this occultation is measured at multiple wavelengths, one can produce what is called the emission spectrum of the planet, which contains information about the thermal struc-

ture and chemistry of the atmosphere. The idea is that the molecular absorption is used to scan the temperature-pressure profile of the atmosphere. Within an atmospheric band, where opacity is high, we probe the temperature structure higher in the atmosphere, while outside the band, where opacity is low, we probe deeper layers. This technique reveals the hemispheric average of the planet's dayside thermal structure when applied to secondary eclipse observations.

The key differences between transmission and emission spectroscopy are the pressures probed. Transmission spectroscopy targets the upper atmosphere, at pressure levels of a millibar or so, as at higher pressures the atmosphere quickly becomes opaque. Emission spectroscopy however targets the deeper layers around pressures of 0.1-1 bar, where the majority of the thermal emission originates.

1.2.3 Phase curves

Observations of an exoplanet as a function of its rotational phase enables complementary measurements of the thermal structure of the planet's atmosphere as a function of longitude. As show in Figure 1.4, a system can be monitored over the full orbit of the planet, referred to as a phase curve. As close-in planets become tidally locked to their hosts, and have permanent day and night side, at each orbital phase we observe new sections of the planet's surface coming into and out of view, from the dayside through quadrature to the nightside. Hence the difference in brightness between any two points in phase can be used to reconstruct the brightness map of the planet's surface (Knutson et al., 2007; Borucki et al., 2009; Snellen et al., 2009).

Phase curves can also be measured spectroscopically. A spectroscopic phase curve measures the spectrum instead of just the brightness at each phase, allowing an extraction of a surface map (or brightness temperature map) in chemistry and temperature structure on top of just temperature (Stevenson et al., 2014c).

Such an inversion, from phase light curve to surface map, can be done in a number of ways. A typical approach is to model the surface of the planet as uniform longitudinal slices, often called the "orange slice" model, or alternatively to separate the phase-curve variation into its sinusoidal components, which can then be inverted to obtain the surface map (Cowan & Agol, 2008; Showman et al., 2008).

1.2.4 Instrumentation

This thesis focuses on studying exoplanet atmospheres of close in gas giant planets using two instruments on two telescopes, at low spectral resolution ($R<1000$), described below. These are space-based instruments, which is of a particular advantage when targeting atoms and molecules, such as water, which can be difficult to observe from the ground due to our atmosphere, such as due to variable water vapour. Ground based instruments have had great success in characterizing exoplanet atmospheres however, in particular using high-resolution techniques to uniquely identify molecular and atomic species (Snellen et al., 2010), dis-

cussed further in Section 1.4. In particular space-based instruments allow us to target the near infra-red (NIR), where the peak of emission for hot planets lies (Figure 1.5).

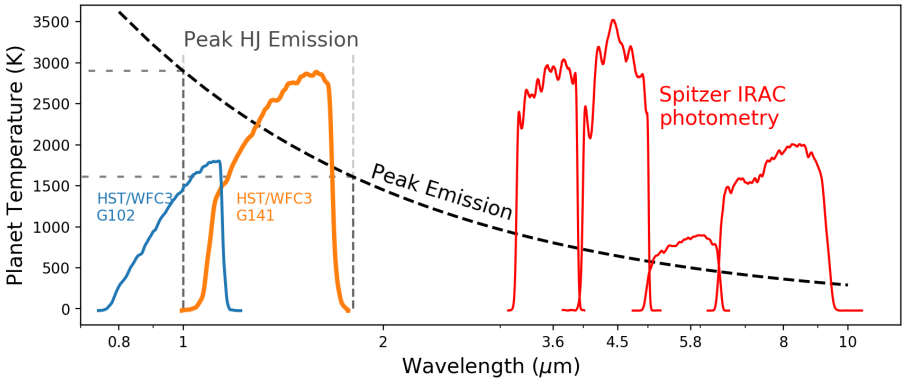

Figure 1.5: Wavelength coverage of space-based instruments taken from their respective documentation, shown over wavelengths of predicted peak planetary emission against planet temperature. The range of hot Jupiter temperatures (1500-3000K) peak in emission exactly in the G141 bandpass of HST/WFC3.

1.2.4.1 The Hubble Space Telescope: WFC3

Some of the standout instruments for characterising exoplanet atmospheres can be found on board of the Hubble Space Telescope (HST). For detecting thermal emission from exoplanets, the Wide Field Camera 3 (WFC3) is the leader in its field, capable of measuring spectra from 0.8-1.7 μm. This wavelength range covers important molecular bands such as water at 1.4μm, while also covering the peak in brightness for objects between roughly 1500-3000K. Coupled with this, HST has the precision to measure abundances of molecules in the spectrum, such as water.

1.2.4.2 Spitzer Space Telescope: IRAC

The Spitzer space telescope was an infrared telescope launched in 2003, into an Earth trailing orbit. Until as recently as January 2020 Spitzer was used to measure photometry in two wavelength bands, at 3.6 and 4.5 μm, but has since been de-activated due to the increasing cost of communication with the telescope. Relevant to this thesis, additional modes were available such as photometry at 5.8 and 8 μm and IR spectroscopy, until the liquid coolant supply was depleted in 2009. Spitzer has been a workhorse for exoplanet atmospheres, with hundreds of transits and eclipses of exoplanets observed, as well as many full-orbit phase curves.

1.2.4.3 Instrumental Challenges

Behind the results coming from these instruments is an extensive body of work understanding and perfecting the data analysis techniques that allow for the subsequent scientific results. Such detailed analysis constitutes a significant part of the work behind thesis. In particular, HST is prone to systematics effects that dominate over the light curves of exoplanets. In recent works, the short term behaviour of the systematics has been well modelled by charge-trapping mechanisms in the detector (Zhou et al., 2017). However, long term systematics in HST are still not fully understood, although they are thought to originate from changes in the temperature of the telescope and the subsequent optical path (Deming et al., 2012; Berta et al., 2012). This is particularly problematic for phase curves, that operate on long timescales, where different systematics or planetary models can lead to different results for the same data (Kreidberg et al., 2018).

1.2.4.4 High Resolution

Low-resolution studies are the focus of this thesis, however there have been simultaneous developments and advancements on atmospheric theories through high resolution spectroscopy. High-resolution studies use a telescopes with increased resolving power, typically R=25,00-100,000 (Birkby, 2018), in order to directly detect and measure spectral lines from an exoplanet (Snellen et al., 2010; Birkby et al., 2013). These planetary lines are separated from the stellar lines by leveraging the relative motion of the star and planet, as their lines are separated in wavelength via the Doppler effect. This technique requires some prior information on the line positions such as from lab experiments, which can be a challenge for some molecules (Hoeijmakers et al., 2015).

There are several advantages to this approach. Firstly molecules can be directly detected in an exoplanet through their unique spectral signatures (Birkby et al., 2013; de Kok et al., 2013; Brogi et al., 2014; Piskorz et al., 2016; Allart et al., 2017; Nugroho et al., 2017; Brogi et al., 2018; Hoeijmakers et al., 2019), which can constrain the temperature profile in the atmosphere (Schwarz et al., 2015; Pino et al., 2020) or the circulation (Snellen et al., 2010; Brogi et al., 2016; Birkby et al., 2017). Secondly the technique naturally extends to non-transiting planets, as the planetary emission can be separated from the star throughout the whole of it's orbit (Brogi et al., 2012; Rodler et al., 2012; Brogi et al., 2013; Lockwood et al., 2014; Piskorz et al., 2017). A key difference between high and low resolution studies are the pressures probed by the observations. Although the exact pressure level is not known for any given observation, high resolution spectra originate from the low pressure atmosphere, but can span many orders of magnitude in pressure within a line. Low-resolution studies typically originate from much deeper in the atmosphere, where the pressure can be measured due to the coupling between the temperature-pressure profile and the observed spectral features.

A clear goal of recent work has been to combine the two approach of high and low resolution spectroscopy, in order to leverage the strengths of each technique (Brogi et al., 2017). This

has seen particular success in the frame of the UHJs, where detections of metal ions and hydrides in the atmospheres of UHJ have provided a new insight into the nature of their atmospheres (Hoeijmakers et al., 2019; Pino et al., 2020).

1.3 Properties of hot Jupiter atmospheres

1.3.1 Atmospheric Chemistry

A hot Jupiter is a gas giant, so the bulk of its atmosphere is made up of Hydrogen and Helium (Seager et al., 1999). In addition most of their other constituents are also in gas phase, such as water, methane, and carbon monoxide (Brown, 2001). While the the range of temperatures that hot Jupiters span is very large (from 1500 K to >3000 K), typically their daysides can be expected to be cloud free, as opposed to their nightsides that may host clouds and condensates (Parmentier et al., 2013; Wakeford et al., 2016; Parmentier et al., 2018; Helling et al., 2019a).

The first step in characterising an atmosphere is to target important, accessible molecules. Water is key to understanding atmospheric chemistry because it is one of the dominant oxygen carrying molecules, with Oxygen being the third most abundant element in the universe. Hence it is a key target of atmospheric characterisation, alongside $CO/CO_2/CH_4$ that dominate Carbon chemistry. Water has been successfully measured in the emission spectra of some of the best exoplanet targets, e.g. a typical hot Jupiter, WASP-43b, shown in Figure 1.6 (Stevenson et al., 2014c).

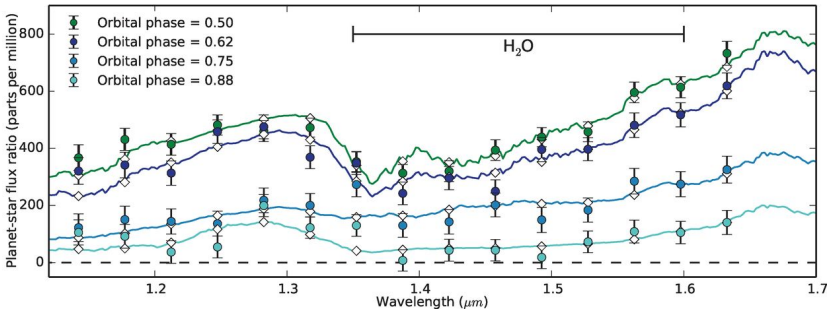

Figure 1.6: Phase resolved spectra of WASP-43b, a $2M_J$ planet on a 0.8 day period around a 4500K K7 star, from Stevenson et al. (2014c). Data were taken with HST/WFC3 G141, shown by coloured points with errorbars. Best fit models are shown at each phase by the corresponding coloured lines. Orbital phase of 0.5 is an average of the planet's dayside around eclipse, whereas orbital phase of 0.75 is at quadrature, when half of the planet's dayside and nightside are seen.

Understanding the full chemical networks of species in an atmosphere would be the goal of any chemical characterization, but water is particularly amenable to detection due to its large broad features in the infra-red (Madhusudhan & Redfield, 2015). Other accessible molecules have similarly been targeted, such as CO in hot atmospheres and CH_4 in cooler planets.

1.3.2 Temperature Structure

Measurements of molecules allow us not only to estimate their abundances in the atmosphere, and hence constrain the metallicity and formation pathways, but also to trace the vertical temperature structure. Measuring the thermal structures of planetary atmospheres provides fundamental diagnostics on how stellar irradiation is absorbed, circulated, and re-emitted (Burrows et al., 2006; Fortney et al., 2008; Showman et al., 2009). Information on the vertical structure can be obtained because the shape and depth of an atmospheric feature is determined by both the abundance of the species and the vertical structure of the atmosphere. As an example, water is a key absorber in the near infra-red, and the spectra in Figure 1.6 show a clear absorption at 1.4μm indicative of a decreasing temperature with increasing height, as the water in the cooler atmosphere absorbs the hot emission from deeper layers (see Figure 1.7).

Due to the intense irradiation that close-in atmospheres are placed under, temperatures structures of exoplanets can vary from the typical adiabatic profiles shown in Figure 1.7. For instance, metal compounds in gas phase can be efficient optical absorbers (Hoeijmakers et al., 2019; Pino et al., 2020), which can result in an increase in temperature at higher altitudes (discussed further in Section 1.4). This hot upper atmosphere would lead to an emission feature rather than an absorption feature in the planet's emission spectrum, e.g. a positive bump of water at 1.4μm due to hot water emission above a cooler background emission from deeper layers.

Hence the vertical temperature structure is not only key to understanding the thermal properties of the atmosphere, but it is required to accurately measure the composition of the atmosphere.

1.3.3 Dynamics & Climate

Phase curves uniquely provide a wealth of information about planetary atmospheres, including longitudinal constraints on atmospheric composition, thermal structure, energy transport, and aerosol formation. In the thermal infrared, the amplitude of the phase variation measures the day-night flux contrast and the phase of peak flux (i.e., hot-spot offset) probes the planet's circulation efficiency at a given pressure level.

Shown in Figure 1.6 are the phase resolved spectra, obtained from three combined full orbit phase curves of WASP-43b. Since the planet is so close in on a period of less than one day, its dayside is tidally locked to permanently face the star, meaning that the planet's orbital phase can be converted to longitude on the planet's surface, and finally into a surface map,

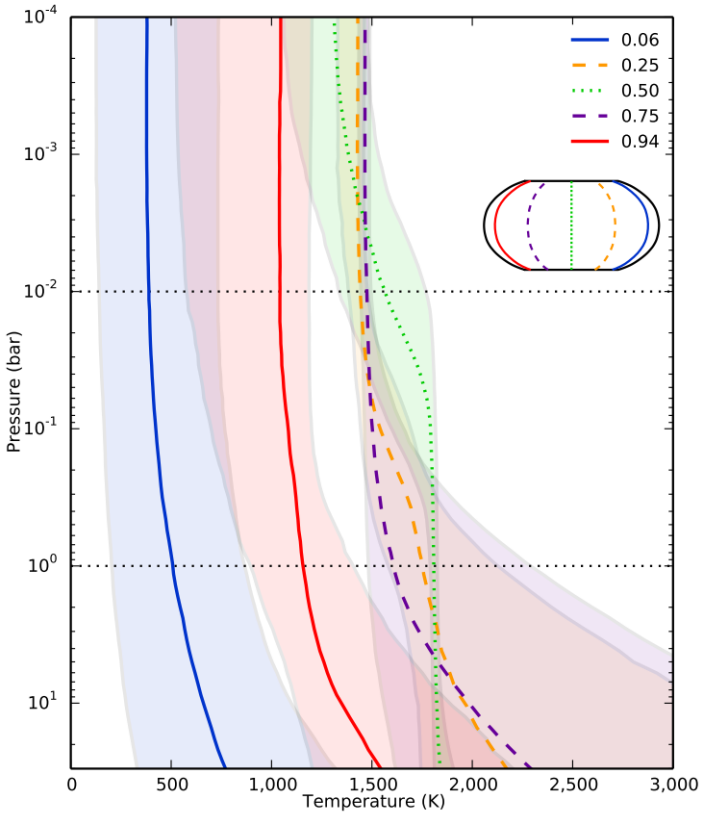

Figure 1.7: Temperature-pressure profiles retrieved from different phases of WASP-43b (Stevenson et al., 2014c).

e.g. Figure 1.8 from Stevenson et al. (2014c). This can be done in the optical (Borucki et al., 2009; Snellen et al., 2009) or in the infra-red with instruments such as Spitzer (Knutson et al., 2007, 2009) or HST (Kreidberg et al., 2018; Arcangeli et al., 2019).

Understanding the atmosphere beyond a dayside average is important to disentangling the chemistry from the climate and vertical structure. This is particularly important when these properties, temperature and chemistry, are expected to change across the atmosphere, something that is intrinsic to hot Jupiters with their permanent dayside and nightside hemispheres (Line & Parmentier, 2016; Feng et al., 2016).

Existing measurements of heat redistribution efficiency in hot Jupiter atmospheres show considerable variation between planets (Cowan et al., 2012; Knutson et al., 2012; Maxted et al., 2013; Zellem et al., 2014; Stevenson et al., 2014b; Wong et al., 2015, 2016). This ranks as one of the biggest mysteries in the field of exoplanet atmospheres. To first order, more highly irradiated planets are predicted to have larger (relative) day/night contrasts because

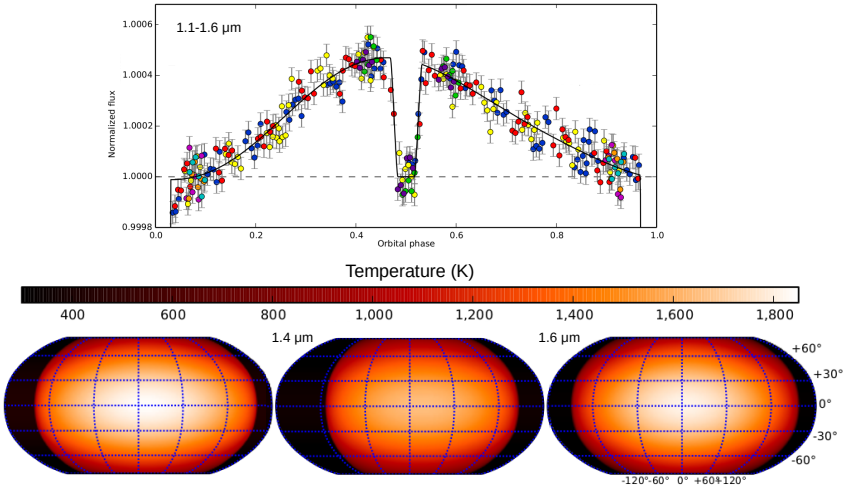

Figure 1.8: Top: Phase curve of WASP-43b observed with HST/WFC3, centred around secondary eclipse. Different coloured points mark data from different epochs. Bottom: Surface temperature maps of WASP-43b at three wavelengths, adapted from Stevenson et al. (2014c).

the short radiative timescales on these planets inhibit efficient heat circulation (Perez-Becker & Showman, 2013; Komacek & Showman, 2016). However, this prediction for hot Jupiter heat re-circulation does not paint the full picture.

Models of hot Jupiter atmospheres actually predicted that the thermal forcing from the day-night temperature contrast should accelerate an equatorial wind, often referred to as a jet, that would act to re-circulate heat from the dayside to the nightside (Showman & Guillot, 2002; Showman & Polvani, 2011). Such a jet is predicted to be as fast as a few km/s, and would result in a shift in the hottest point on the surface of the planet, away from the sub-stellar point. This is a key observable, as the thermal map of a planet measured via a full phase curve can be used to trace the location of such a hot spot.

These brightness offsets have been observed, which when eastward in longitude are indeed attributed to an equatorial jet (Knutson et al., 2012; Cowan et al., 2012). However a more complicated picture has been revealed with a large reverse (westward) offset detected in CoRoT-2b's emission (Dang et al., 2018) and the time-variable offset of HAT-P-7b (Armstrong et al., 2016), currently thought to originate from magnetic or dynamical instabilities.

1.3.4 Atmospheric Modelling

Predictions and inferences from observed spectra are only possible with detailed modelling of the planetary atmosphere. The models of atmospheres relevant to this thesis can be broadly characterized by two features, their degree which ranges from 1D to 3D, and their application, which can be either in statisical retrievals or as forward models.

Retrieval constructs a model of an atmosphere via a statistical fit to the data, producing thousands of models to compare and relying on simplifications in order to make the computational time feasible. Such simplifications might include limited chemical networks or parametrization of physical processes such as heat transport or cloud formation. This then allows for inference when a wide range of models might fit the data, such as considering molecular abundances that might span an order of magnitude. Forward modelling instead is a solution to the full equations, including all known, relevant physics and chemistry. Such models are more predictive in nature, and for instance are used to predict climates in complex atmospheric circulation models, that cannot be simplified parametrically without a significant loss in accuracy.

Adjacent to the type of model is the degree, ranging from 1D to 3D (or climate) modelling. Models for retrieval (and many forward models) are typically in 1D, fulfilling computational limitations while still capturing the vertical structure of the atmosphere. Global climate models (GCMs) instead solve the full or simplified fluid dynamical equations, typically in 3D, and are appropriate for planets with changes in temperature or chemistry with longitude. Due to computational complexity these higher dimensional models cannot yet be used in retrievals, as they take many hours per simulation. The clear advantage of these models is that they can capture physical processes more accurately and make powerful predictions for future observations. However, these 3D forward models cannot actually include the full physics of a system, such as magnetic effects or sub-grid instabilities, and a great deal of the challenge of these models is understanding the underlying cause for any observed feature in a simulated climate.

Understanding of these models is key because it is by challenging these models with observations that we advance our theories. Indeed, our understanding of the ultra hot Jupiter population has been driven by the disconnect between observations of the hottest gas giants and previously existing models, the progression of which is outlined below.

1.4 New Climates: Ultra hot Jupiters

1.4.1 From hot to ultra hot atmospheres

Before the properties of ultra hot Jupiter atmospheres were fully understood, there was an ongoing hunt for thermal inversions in classical hot Jupiters. The expectation for hot Jupiters was that, beyond a temperature of 1800 K or so, all molecular compounds and clouds would evaporate. This included metal compounds (such as TiO and VO) that would evaporate and lead to efficient absorption of stellar light at high altitudes (Hubeny et al., 2003; Fortney et al., 2008). In turn, this would result in an increase in the temperature at high altitudes, contrary to a typically adiabatic temperature decrease. This is analogous to the action of the Ozone layer on earth, where the temperature is higher in the stratosphere due to the absorption of ultra-violet light by O_3.

The first hints of thermal inversions in hot Jupiters emerged from observations with the Spitzer space telescope, comparing emission fluxes using 3.6μm and 4.5μm photometry

(Nymeyer et al., 2011; Deming et al., 2012). The dominant species in the Spitzer bandpasses are CH_4 at 3.6μm and CO at 4.5μm, with H_2O contributing to both bands. At high temperatures, chemical equilibrium dictates that Carbon should preferentially form CO over CH_4, hence an excess in emission at 4.5μm relative to 3.6μm is indicative of CO in emission and therefore a thermal inversion. As this inference relies on only two photometric points, in individual cases it has not been possible to conclusively detect a thermal inversion. Recent work by Baxter et al. (2020) has considered a much larger statistical sample of Spitzer emission measurements, and finds evidence for a transition in temperature, and the emergence of inversions in UHJ atmospheres.

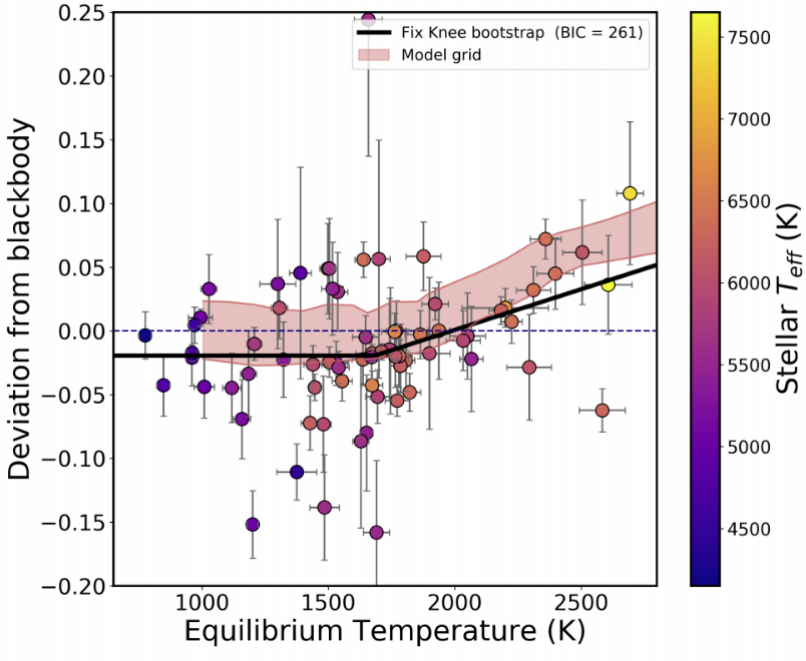

Figure 1.9: A transition between HJ and UHJ from their thermal emission (Baxter et al., 2020), the transition occurs 1700K. UHJ exhibit a thermal inversion and/or inefficiency in their heat advection that is correlated with their dayside temperature.

1.4.2 Challenging Models

The daysides of the hottest atmospheres initially measured with HST were a little surprising, providing a challenge for modelling efforts. Firstly, for temperatures above 2500K, many emission spectra appeared to be flat and close to black-body curves. Secondly, retrievals on these spectra came out with very different abundances than their cooler counterparts (Stevenson et al., 2014a; Haynes et al., 2015; Evans et al., 2017; Sheppard et al., 2017).

This was in part due to the apparent disconnect between the CO emission in Spitzer and the lack of water in emission in HST, that drove retrievals towards high C/O ratios in some cases. This is because a hot atmosphere with a high C/O ratio has most of its oxygen locked up in CO and CO_2, leading to a decreased H_2O abundance which could explain the lack of water seen with HST. These abundances had strong implications for the formation of hot Jupiters, in order to explain for instance why the hottest planets should differ in formation from their cooler counterparts.

A similar hurdle was met when observers targeted spectral features of TiO and VO, in order to detect the species thought to be responsible for the predicted inversions. To date most evidence of TiO has been inconclusive, with upper limits for HD209458b (Désert et al., 2008) or non-detections for WASP-12b (Sing et al., 2013), WASP-19b (Huitson et al., 2013; Espinoza et al., 2018), and WASP-121b (Merritt et al., 2020). Reports of TiO/VO features have been made for WASP-19b (Sedaghati et al., 2017) and WASP-121b (Evans et al., 2016, 2017) although they have since been disputed (Espinoza et al., 2019; Mikal-Evans et al., 2020). So far the strongest evidence of TiO is seen on WASP-33b (Haynes et al., 2015; Nugroho et al., 2017), although the most recent work has not been able to confirm these findings (Herman et al., 2020). Theory can explain the absence of TiO and VO in the atmospheres of such planets, e.g. through cold trapping of these species in the deeper layers (Fortney et al., 2008; Spiegel et al., 2009), which would either imply that inversions should not be so common, or that other species would need to be responsible for inversions seen (Sharp & Burrows, 2007; Lothringer et al., 2018).

What emerged was that key physics was missing from retrievals of these hot daysides, which separated this ultra-hot population chemically from the typical hot Jupiters. During the timeline of this thesis, and also in part thanks to this work, the UHJ atmospheres are now modeled in a different way. Firstly their atmospheres are now known to be heavily effected by thermal dissociation of key species, such as water and TiO. Secondly the opacity from H^- ions is included, which provides a large continuum opacity much like in stellar photospheres. Thirdly, gaseous metals and metal hydrides such as FeH are now thought to be the dominant cause of inversions for the ultra hot atmospheres. Certain models did already account for these effects, such as those derived from stellar models that assumed radiative-convective equilibrium (Barman et al., 2001; Burrows et al., 2008; Fortney et al., 2008), however the full consequences of dissociation and H^- to these ultra-hot atmospheres were not explored.

The literature on the atmospheres of UHJ and these effects has appeared only in the last few years, with more than 50 published papers about UHJ since 2018, and a small Wikipedia entry in January of 2020. While ultra hot Jupiters atmospheres were initially targeted and studied due to their high signal to noise ratio, it was not until the combined efforts of modellers and observers, some of which is presented in this thesis, that their unique properties were identified. In this section are presented some of the highlights from recent work, after which follows the Thesis outline.

1.4.3 Dayside Chemistry

Some early work on ultra hot planets found that H_2 was likely dissociating in their atmospheres (Bell et al., 2017). In a series of papers, starting with (Arcangeli et al., 2018) presented in Chapter 2, this was extended to dissociation of other key molecules such as H_2O and TiO, as models showed they should be similarly dissociated in UHJ photospheres. This was found to be in agreement with observations of the hottest planets (Kreidberg et al., 2018; Lothringer et al., 2018; Mansfield et al., 2018; Parmentier et al., 2018). On top this they found that dissociated H atoms would recombine with electrons released by the thermal ionization of metals to form H^-, a dominant opacity in these and stellar atmospheres. Additionally, the effects of dissociation and subsequent recombination on the climates of ultra hot Jupiters were revealed (Komacek & Tan, 2018), with increased heat transport due to nightside H2 recombination also playing a role (Bell & Cowan, 2018). In summary these results showed the previously assumed equilibrium abundances of certain key molecules did not hold in these hot atmospheres, and therefore many inferences based on perceived deviations of abundances from equilibrium would have to be re-considered.

As an aside, the role of H^- in UHJ atmospheres is very like the role of H^- in the sun, and this similarity even extends to their historical context. In the early 1900s, one of the leading questions concerning solar physics was in understanding what was the missing opacity source in the sun. Modelling of our sun had found that, with all known physics and chemistry accounted for, models fell short of reproducing the amplitude of the solar spectrum by a significant amount (Unsold, 1938; Page, 1939). This is where H^- then stepped in, as it essentially acts as a continuum opacity consisting of a bound-free component at shorter wavelengths and a free-free component at longer wavelengths. Work was being done to calculate the opacity from H^- (Pannekoek, 1930, 1931; Jen, 1933), and with its contribution as a significant opacity source to the sun, modellers were now able to reproduce the solar spectrum (Wildt, 1939; Chandrasekhar, 1945a,b). This story is remarkably similar to the story of UHJ, as the question of why water could not be seen in emission could have been phrased as what was the opacity source that filled in the spectrum below 1.4μm where water is transparent (Parmentier et al., 2018).

One standout ultra hot Jupiter is the the hottest exoplanet to date, Kelt-9b (Gaudi et al., 2017), for which models revealed a peculiar chemistry dominated by ions and dissociated molecules (Kitzmann et al., 2018). This was confirmed by the ground breaking detection of 7 metallic species in various ionization states in the atmosphere of KELT-9b (Hoeijmakers et al., 2019). These detections were carried out using the high-resolution technique, that separates the lines of a species in the planet's atmosphere from the stellar atmosphere via their relative doppler motion. This technique has also been successfully applied to other ultra-hot targets, MASCARA-2b/KELT-20b (Casasayas-Barris et al., 2019) and WASP-121b (Cabot et al., 2020), and for detecting ionized Calcium in KELT-9b and WASP-33b (Yan et al., 2019; Turner et al., 2020).

1.4.4 Nightside & Climate

The climate of UHJs has been the focus of attention in recent years. Spectroscopic phase curves have been observed with HST, that each show large temperature contrasts between the dayside and nightside hemispheres (Kreidberg et al., 2018; Arcangeli et al., 2019), in agreement with earlier results from Spitzer (Maxted et al., 2013). These contrasts can only be reproduced in models when additional physics are included, such as drag sources, that could for instance match the action of a Jupiter-like magnetic field on the already ionized dayside atmosphere. Models of their cloud properties suggest that the nightsides of these planets should indeed be covered in clouds (Helling et al., 2019a,b), despite the additional heat transport expected from H_2 recombination on the nightside (Bell & Cowan, 2018; Komacek & Tan, 2018). It has also been suggested that these clouds are responsible for the apparent homogeneity in nightside temperatures measured for hot Jupiters (Keating et al., 2019). Recent results from the TESS project present the full-orbit optical phase curves of some UHJs, namely WASP-18b (Shporer et al., 2019) and WASP-121b (Bourrier et al., 2019; Daylan et al., 2019). As the planets are so hot, these optical phase curves still target the emission of UHJ, and similarly find large day-night contrasts indicative of weak circulation.

1.4.5 Two archetypes of UHJs

This thesis directly focuses on two ultra hot Jupiter planets, WASP-12b and WASP-18b. WASP-18b is the main subject of this thesis, and can be considered an archetypal UHJ in many ways. This planet was discovered by the WASP survey (Hellier et al., 2009) on a short and mildly eccentric orbit of 0.94 days period around a bright F6 star, leading to a dayside temperature of over 2500K. What marks WASP-18b as unique is its high mass, approximately 10 times the mass of Jupiter, that places it on the boundary between a gas-giant planet and a brown dwarf. In fact, the prediction is that WASP-18b's orbit should decay due to tidal forces, with an estimated one million years until the planet would crash into its host. Follow-up measurements have been made since 2009 to monitor the period of WASP-18b in order to detect any tidal decay but so far the evidence is not conclusive (Wilkins et al., 2017; Patra et al., 2020).

The planet's thermal emission was the target of its first atmospheric studies; using the Spitzer Space Telescope, Nymeyer et al. (2011) obtained four secondary eclipses between 3.6 and 8μm while Maxted et al. (2013) measured the thermal phase curve at 3.6 and 4.5μm. The dayside photometry hinted at a thermal inversion, with an increase in emission at 4.5μm where CO dominates. The data was also consistent with a 3200K blackbody spectrum, although this was physically hard to reconcile. What was certain from this data is that the dayside temperature was too hot for any significant amount of energy to circulate to the nightside. This was confirmed in the study of the phase curves of WASP-18b by Maxted et al. (2013), who saw a large day-night contrast consistent with no redistribution. Furthermore, the magnitude of the dayside brightness meant that the system had to be tidally locked, as expected from theory (Iro & Maxted, 2013).

The next generation of instruments to look at WASP-18b were HST and TESS. Our work, on the eclipse and on the phase curve of WASP-18b, is presented in Chapters 2, 3, and 5.

These are described in more detail in Section 1.5. The Transiting Exoplanets Satellite (TESS) observed WASP-18b for a full month as a part of its all-sky monitoring program (Shporer et al., 2019). This effectively measured a high precision phase curve in the optical, which was found to be consistent with the measured thermal emission in the infra-red, but also identified an additional component to the light curve. This additional component, referred to as stellar ellipsoidal variation, is due to the deformation of the host star by the gravity of the planet. WASP-18b is an extreme case of this, as it is a high mass planet on a close orbit, as we showed that these ellipsoidal variations were also critical for our phase curve measured with HST.

1.5 Thesis Outline

In this thesis, I use observations in the near infra-red with HST/WFC3 and Spitzer to measure and characterize the atmospheres of ultra hot Jupiters. The first example of an Ultra hot Jupiter being defined with an explanation of its chemistry is presented in Chapter 2. In this chapter we observe the dayside emission spectrum of WASP-18b, and find that previous modelling efforts of this and other such hot systems were lacking key physics. We include these effects in our models, namely the effects of dissociation on molecular species such as water and TiO, as well as the continuum opacity provided by the negative hydrogen ion H-. We find that we can match the observed data with a solar composition atmosphere, in line with cooler gas giants.

In Chapter 3 we continue our study of WASP-18b through its full-orbit phase curve observed in the NIR with HST/WFC3, where we observe a large day-night contrast indicating very poor atmospheric circulation. We find that the nightside is actually below our detection limits, due to both the low temperature and the uncertainty on the long-term instrument systematics. Compounding these effects we also detect evidence of ellipsoidal variations in the star due to the gravitational field of the planet, that confirm independent measurements with the TESS satellite in the optical (Shporer et al., 2019). We compare our results to circulation models of the atmosphere and find that we again require additional physics to explain the data, in this case through an atmospheric drag term. We explore what the origins of such a drag might be and find that it is consistent with Lorentz-force drag on the ionized winds by a Jupiter-like magnetic field.

Chapter 4 details a new technique that we developed for analyzing spectroscopic phase curves. This technique allows us to extract unpublished archival spectra of WASP-12b, another UHJ, for which only a partial phase curve was observed. We obtained the first constraints on the climate of WASP-12b and explore how our new technique could be used to observe partial phase curves in the future.

Finally in Chapter 5 we apply our new technique to our previously analyzed phase curve of WASP-18b, and show that we are able to measure spectra at different orbital phases and recover the thermal variation of the planet. This new extraction reveals spectral variations that were not accessible with classical methods.

Chapter 2

H- Opacity and Water Dissociation in the Dayside Atmosphere of the Very Hot Gas Giant WASP-18b

Jacob Arcangeli, Jean-Michel Désert, Michael R. Line, Jacob L. Bean, Viven Parmentier, Kevin B. Stevenson, Laura Kreidberg, Jonathan J. Fortney, Megan Mansfield, Adam P. Showman

ApJ Letters, 2018, Volume 855 Number 2, L30

Abstract

We present one of the most precise emission spectra of an exoplanet observed so far. We combine five secondary eclipses of the hot Jupiter WASP-18 b ($T_{day} \sim 2900$ K) that we secured between 1.1 and 1.7 μm with the WFC3 instrument aboard the Hubble Space Telescope. Our extracted spectrum (S/N=50, R$\sim$40) does not exhibit clearly identifiable molecular features but is poorly matched by a blackbody spectrum. We complement this data with previously published Spitzer/IRAC observations of this target and interpret the combined spectrum by computing a grid of self-consistent, 1D forward models, varying the composition and energy budget. At these high temperatures, we find there are important contributions to the overall opacity from H^- ions, as well as the removal of major molecules by thermal dissociation (including water), and thermal ionization of metals. These effects were omitted in previous spectral retrievals for very hot gas giants, and we argue that they must be included to properly interpret the spectra of these objects. We infer a new metallicity and C/O ratio for WASP-18 b, and find them well constrained to be solar ([M/H]$= -0.01 \pm 0.35$, C/O < 0.85 at 3σ confidence level), unlike previous work but in line with expectations for giant planets. The best fitting self-consistent temperature-pressure profiles are inverted, resulting in an emission feature at 4.5 μm seen in the Spitzer photometry. These results further strengthen the evidence that the family of very hot gas giant exoplanets commonly exhibit thermal inversions.

planets and satellites: atmospheres — planets and satellites: gaseous planets

2.1 Introduction

Hot Jupiters are the easiest exoplanets to study because they are hot enough to have most or all of their atmospheric constituents in gas phase. From the growing number of known exoplanets, the population of very-hot hot Jupiters has emerged (Sudarsky et al., 2000). This subset spans a range of dayside temperatures from 2500-4600 K, with the hottest being as hot as the photosphere of a K-dwarf star (KELT-9b; Gaudi et al. 2017). These extreme planets are currently being discovered by ground-based surveys that focus on bright stars. Several important questions have emerged from the study of these highly irradiated planets, including the influence of stellar irradiation on their inflated radii and mass loss rate, their atmospheric composition, and the frequency and origin of stratospheric thermal inversions.

Hubeny et al. (2003) first proposed the possibility of a bifurcation in the thermal structure of giant exoplanet atmospheres. Strong irradiation combined with efficient optical absorbers in the atmosphere (such as TiO and VO in gas-phase) could cause an inversion layer in the temperature-pressure profile (Fortney et al., 2006, 2008; Burrows et al., 2008; Parmentier et al., 2015).

Recent observations of some of these extreme hot giants have revealed temperature inversions in their atmospheres (WASP-33 b: Haynes et al. 2015, WASP-121 b: Evans et al. 2017, WASP-18 b: Sheppard et al. 2017). Nevertheless, for all these studies, the retrieved metallicities and abundances are much higher than expected for a solar composition (e.g. VO 1000x solar for WASP-121 b, metallicity $\sim$300x solar with a C/O$\sim$1 for WASP-18 b). This is surprising for such massive gas giants, as their expected formation channels imply that their metallicities should be close to their host stars', as observed in their cooler counterparts (e.g., Kreidberg et al. 2014a; Benneke 2015; Line & Parmentier 2016).

In this paper, we argue that chemistry and opacity sources that are well known to operate at high temperatures from stellar astrophysics are key to the interpretation of very hot gas giant atmospheres. In particular, some of the primary sources of opacity on the daysides of these atmospheres will thermally dissociate at sufficiently low pressures and high temperatures. A second consideration is the effect of thermal ionization, whose electrons provide the seeds for bound-free and free-free interactions with atomic hydrogen that generate H^- opacity (see Section 2.3.2). While these effects are included in some models of very hot gas giants, in particular those that assume radiative-convective equilibrium, (e.g., Barman et al. 2001; Burrows et al. 2008; Fortney et al. 2008), their consequences for spectral retrieval have not yet been explored.

In this context, we present a new analysis and interpretation of observations obtained with the Hubble Space Telescope Wide Field Camera 3 (HST WFC3) and Spitzer Infrared Array Camera (IRAC) of the dayside emission spectrum of WASP-18 b. WASP-18 b (Hellier et al., 2009) is a 10 $10M_J$ planet that orbits a bright F6 host (Vmag=9.3) on a short period (0.94 days), and has an equilibrium temperature of 2700K. In Section 2.2 we present the observa-

tions and data analysis. In Section 2.3 we discuss the effect of thermal dissociation and H^- opacities on the interpretation of this emission spectrum.

2.2 Observations and Data Reduction

2.2.1 Observations

Our team observed five secondary eclipses of WASP-18b with 24 orbits of the HST as part of a larger Treasury program (GO-13467), including a phase-curve presented in a separate paper (Arcangeli et al. in prep.). We concentrate here on the secondary eclipse observations. The data were obtained with HST/WFC3, with the G141 grism, covering 1.1 to 1.7μm, using the spatial scanning technique in both directions. Individual pixels in the spectrum reached a maximum flux level of 30,000 electrons, below 40% of full-well saturation, where the pixel response is linear.

The first two eclipses were taken using the 256x256 pixel subarray (SPARS10, NSAMP=12, 74s exposures), however the spectrum was seen to leak outside of this subframe. Subsequent data used the 512x512 subarray (SPARS10, NSAMP=16, 112s exposures) with the same scan rate. We remove part of the second eclipse's final orbit, due to a loss of fine-guidance.

2.2.2 Data reduction and analysis

We developed a custom data reduction and analysis pipeline following the methods outlined in Kreidberg et al. (2014b). We first form subexposures from each full exposure by subtracting consecutive non-destructive reads. We calibrate the wavelength solution using a direct image taken at the start of each visit. We apply a wavelength-dependent flat-field correction and remove cosmic rays using a local median filter. We calculate the average sky background by masking the spectra on each subexposure, iteratively clipping outlier pixels. We finally apply an optimal extraction algorithm (Horne, 1986) to maximise the signal-to-noise from each subexposure.

The reduced light curves are dominated by time-dependent systematics characteristic of HST observations. We parametrise these using the $\mathrm{model\text{-}ramp}$ technique with a single exponential in time and a linear visit-long slope. We remove the first orbit of each visit from our analysis. The second orbit is parametrised with a separate ramp amplitude. We compare the $\mathrm{model\text{-}ramp}$ technique with a common-mode correction and find we reach the same precision in each of the light-curve fits.

We fit for the instrument systematics, the eclipse-depth, and eclipse time simultaneously for a total of 7 free parameters for each of the white light curves. We then bin the data into 14 wavelength channels and fit again in each channel whilst maintaining the ramp timescale and eclipse time fixed to the white-light curve values. The remaining system parameters are fixed to literature values from Southworth (2011). We combine the five extracted secondary eclipse spectra since we find that each are consistent within one sigma. The residuals from

the white light curve fits range from 1.05x to 2x the photon noise limit. The precision reached in the spectroscopic fits is less than 1.2x photon noise for each bin.

In order to estimate the errors on our fitted parameters and identify the degeneracies in the model we use a Markov chain Monte Carlo approach using the open-source EMCEE code (Foreman-Mackey et al., 2013). We test convergence by employing the Gelmaan-Rubin diagnostic for each chain of 10,000 steps with 400 walkers. Our final precision on the spectroscopic eclipse depths is 20 ppm per wavelength bin in the combined spectrum, achieving a signal-to-noise ratio of 50 at a resolution of R$\sim$ 40. Our combined spectrum is consistent with Sheppard et al. (2017).

2.3 Results & Discussion

The combined WFC3 emission spectrum (show in Figure 2.1) does not exhibit spectral features expected from molecules such as H_2O or TiO. We complement the WFC3 emission spectrum with four Spitzer/IRAC data points already published (Nymeyer et al., 2011; Maxted et al., 2013), after ensuring that the system parameters are consistent, and we present below several scenarios to explain this combined spectrum.

2.3.1 Fitting a blackbody spectrum

We first test whether the WFC3 emission spectrum is consistent with a simple blackbody spectrum, which would be caused by an isothermal atmosphere over the pressures probed. We find a best fit blackbody temperature of 2890$\pm$47 K, using a PHOENIX stellar model of T=6400K, logg=4.5, and [M/H]=0.0 for the star. However, this is a relatively poor fit to the data, with a reduced χ^2 of 3.1.

The Spitzer/IRAC photometric points at 3.5, 5.8 and 8.0 μm lie on the blackbody spectrum extrapolated from our WFC3 data, but the planet's flux at 4.5 μm is larger by 2σ, suggesting the presence of emission features (see Figure 2.1). In this wavelength range the dominant opacity sources are CO and H_2O, and spectral features would appear in emission only if the temperature-pressure profile of the atmosphere were inverted, and not isothermal. However the lack of water spectral features at 1.4 μm could appear to be at odds with this conclusion. Previous studies have explained WASP-18b's spectrum with a high C/O ratio that can deplete the gas-phase water and remove its spectral features whilst allowing for a non-isothermal atmosphere (Sheppard et al., 2017). In the following section, we present an alternative explanation taking into account the key changes in opacity at these high temperatures, due to molecular dissociation, thermal ionization, and the presence of H^- ions, while requiring nominal solar metallicity and C/O.

2.3.2 Opacity sources in very hot gas giant exoplanet atmospheres

The dominant opacity sources in the near infrared (NIR) for hot Jupiters are H_2O, CO, and metal hydrides and oxides. However, for the very-hot hot Jupiters (T$>$ 2500 K), a significant

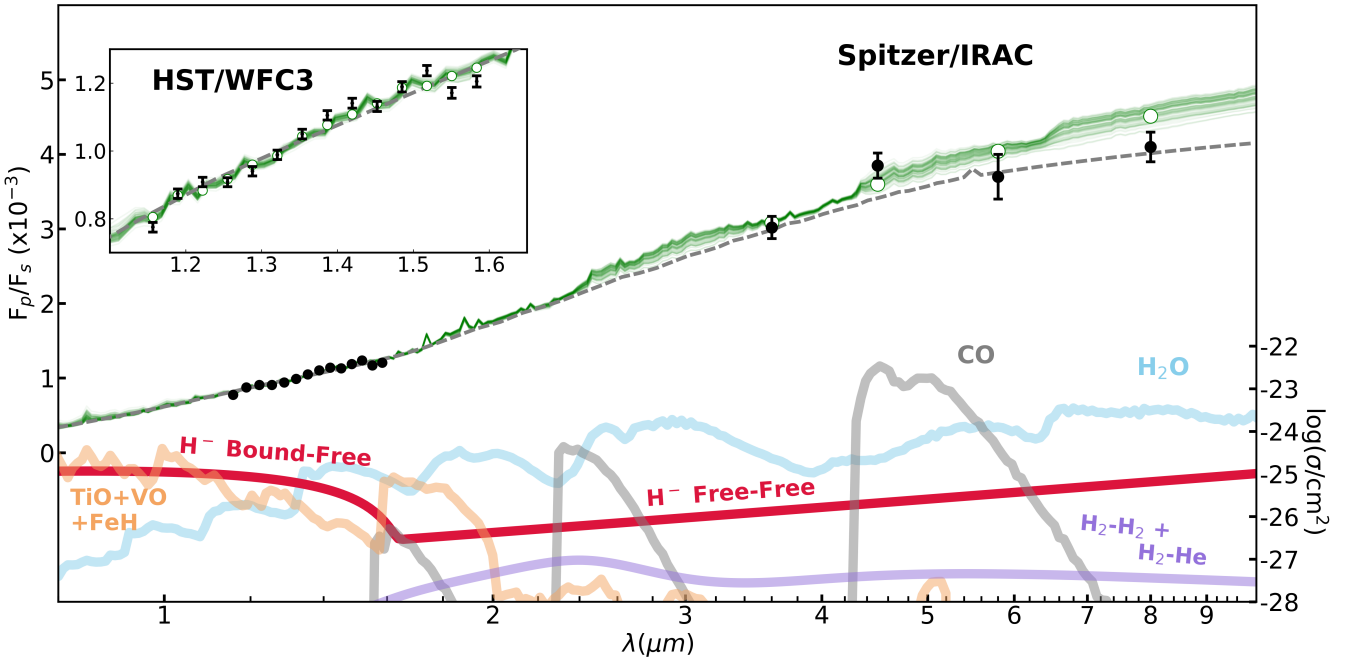

Figure 2.1: Dayside eclipse spectrum (black points) from this work and previous Spitzer observations compared to best-fit model spectrum (white circles). The best-fit model has a reduced chi-squared of 2.0. In green are 100 samples from the posterior of the model spectrum derived from the grid retrieval, and in grey the best-fit blackbody spectrum to the WFC3 data of 2890±47 K. Dominant opacity cross sections weighted by their molecular abundances (log(σ)) are shown for key molecules, taken at a pressure level of 0.33 bar (the peak of the WFC3 emission).

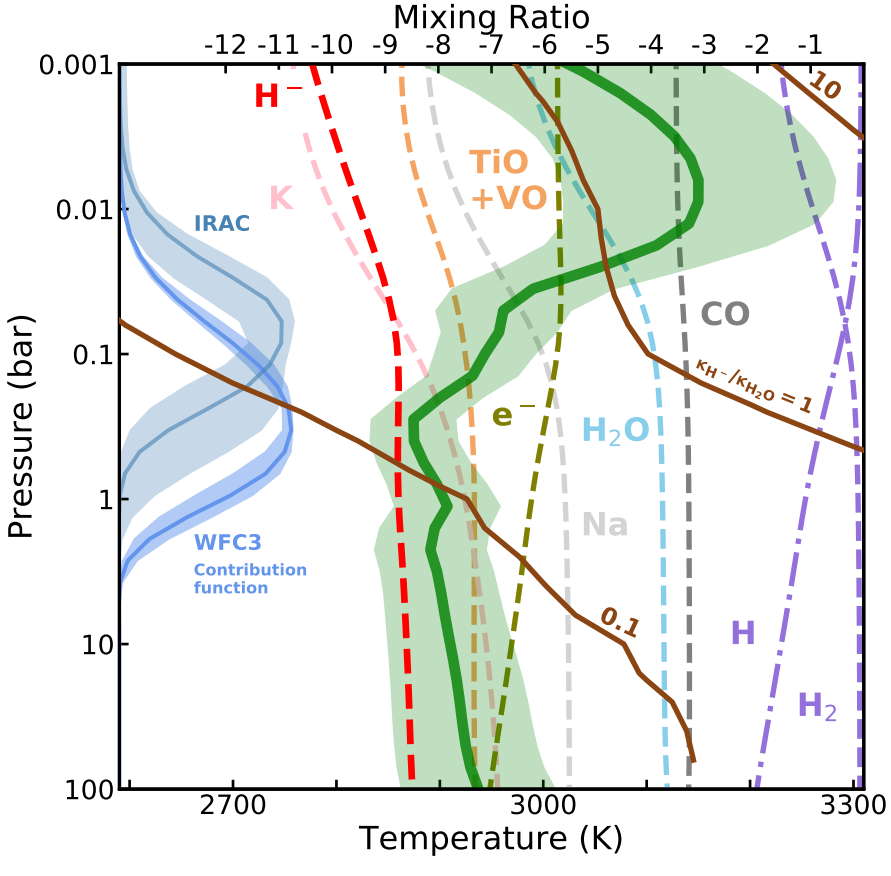

Figure 2.2: Best fit T-P profile shown in green with 1σ error contours. Flux contribution functions are shown on the left for HST/WFC3 and Spitzer/IRAC in blue with 1σ regions. Dashed lines show the logarithm of the mixing ratios for key species at different pressures. Lines in brown denote contours of the ratio between the bound-free opacity of H^- at 1.25μm and molecular gas opacity, mainly from H_2O and TiO.

fraction of water also thermally dissociates at low pressures (Parmentier et al., 2018). In cool stellar photospheres with similar temperatures, large water absorption features can still be observed in their spectra as the increased pressure at the photosphere due to their higher surface gravities prevents dissociation (Kirkpatrick et al., 1993). However, hot Jupiters have lower surface gravities, and consequently photospheres at lower pressures (around 0.1 bar for WASP-18 b), thus their spectra should be depleted in water beyond 2700 K. Carbon monoxide is harder to thermally dissociate, and should be present for temperatures below 4000 K, as expected in WASP-18 b. Furthermore, while the cross-section of water increases, the line contrast weakens at higher temperatures (e.g., Burrows et al. 1997). Hence, it is inherently harder to identify spectral features of water at high temperatures.

Opacities from the negative hydrogen ion H^- are relevant at temperatures between 2500-8000 K (e.g., Pannekoek 1931; Chandrasekhar 1945a; Lenzuni et al. 1991), hence they are important for very highly irradiated exoplanets (Figure 2.1). Atomic hydrogen is produced through thermal dissociation of molecular hydrogen at these high temperatures (e.g., Bell et al. 2017), along with electrons from the metal ionization (see Figure 2.2). Therefore, we argue that the hottest gas giants will show significant opacity from H^- ions on their daysides. We study the importance of H^- with planet mass and temperature in a companion paper (Parmentier et al. in prep.).

2.3.3 Atmospheric modelling including H^- opacities and molecular dissociation

We produce a newly developed cloud-free grid of 1D self-consistent radiative-convective-thermochemical equilibrium models to interpret the data (ScCHIMERA, Self-consistent CHIMERA, Line et al. 2013). We use the Toon et al. (1989) two-stream source function technique under the hemispheric mean approximation to solve for the infrared radiative fluxes at each atmospheric layer combined with a convective adjustment scheme in the deeper atmosphere. The incident stellar flux is modelled as pure attenuation at a disk averaged airmass of $1/\sqrt{3}$. The molecular, ion, and condensate abundances are derived using the NASA CEA2 Gibbs-free energy minimization routine (Gordon & McBride, 1994) given the elemental abundances scaled from Lodders et al. (2009) via the metallicity, [M/H], and carbon-to-oxygen ratio, C/O, while accounting for the depletion of elements due to condensate rain-out. We implement the line-by-line cross section database described in Freedman et al. (2008, 2014) with in the correlated-K "resort-rebin" framework described in Lacis & Oinas (1991); Mollière et al. (2015) and Amundsen et al. (2016) at a constant resolving power of 100 between 0.3 and 200 μm. The code has been validated against analytic solutions and agrees to within 3% and against the brown dwarf models of Marley et al. (2010). Bound-free and free-free opacities are taken from John (1988) and Bell & Berrington (1987), respectively. The grid is parametrised with a scaling factor to the stellar flux ($0.75 \leq f \leq 2.5$) to account for the unknown albedo and day-to-night heat transport (such that when f=1 there is complete day-night redistribution and when f=2 only the dayside re-radiates), the metallicity ($-1 <$[M/H]< 2), and carbon-to-oxygen ratio ($0.1 <$C/O< 10 with finer sampling between 0.75 and 2). Parameter estimation is performed over the grid using the EMCEE package

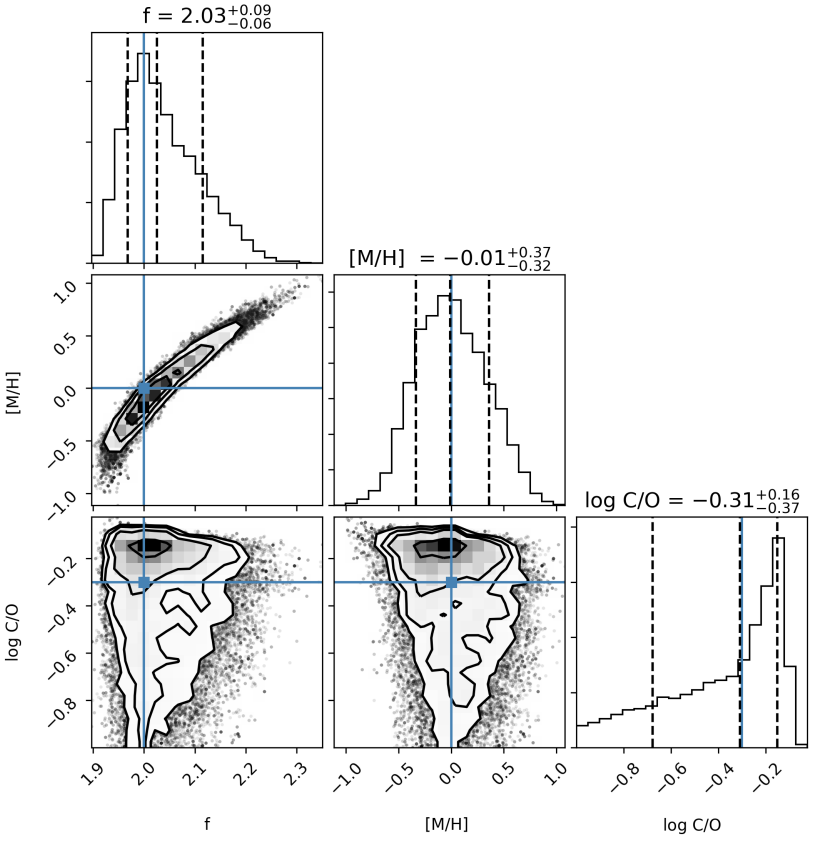

Figure 2.3: Posterior distributions from the grid retrieval. Forward models calculated varying log(C/O), [M/H] and f (redistribution factor). The extracted metallicity and C/O ratio are consistent with solar values (plotted in blue), f is consistent with no day-night redistribution.

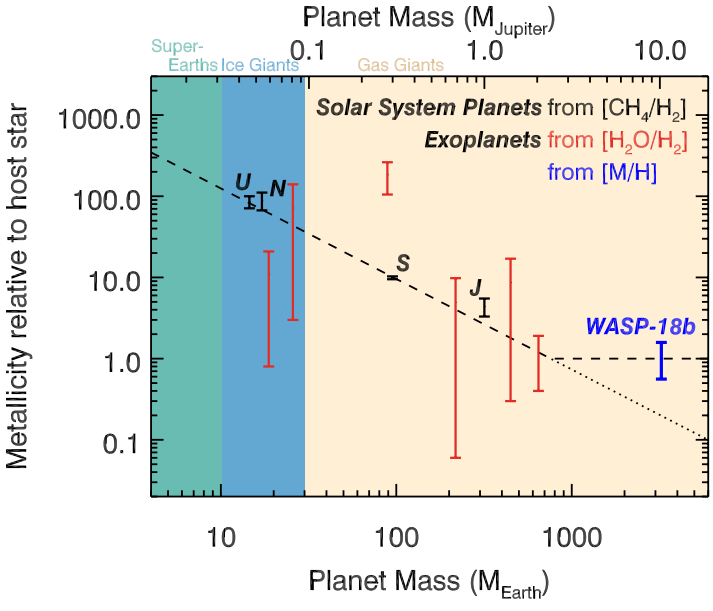

Figure 2.4: Mass-metallicity plot of the solar system planets including known exoplanet metallicity estimates from measured water abundances (Mansfield et al. in prep. and references therein). For the most massive planets, the metallicity should not follow a log-linear relationship but should approach the metallicity of the host star, as seen in WASP-18 b where the stellar metallicity is 0.11 ± 0.08 (Torres et al., 2012)

.

(Foreman-Mackey et al., 2013) via interpolation of the spectra along the grid dimensions, binned to the appropriate WFC3 and Spitzer resolution elements/profiles. The grid resolution is fine enough that interpolation errors are negligible.

We achieve a best fit with a reduced chi-squared of 2.0. We found that, when both H^- opacities and dissociation effects were not included, our retrievals were pushed to high C/O in order to explain the lack of water features, as seen in other studies (e.g, Sheppard et al. 2017). A pairs plot of the posterior distributions is shown in Figure 2.3. The metallicity is constrained to be solar ($[M/H] = -0.01 \pm 0.35$). A high C/O ratio is ruled out; we retrieve C/O< 0.85 at 3σ confidence, also consistent with solar. Our retrieved value of f$=2.03 \pm 0.08$ is consistent with minimal day-night redistribution expected for such a hot planet (Perez-Becker & Showman, 2013) and measured by Maxted et al. (2013).

2.3.4 WASP-18 b's atmospheric metallicity, composition, and thermal structure

We compare the retrieved metallicity of WASP-18 b to the measured metallicities of solar system giants and exoplanets in Figure 2.4 and show that WASP-18 b agrees with the expec-

tation that the metallicities of the most massive planets should approach the metallicities of their host stars.

The tight constraint on metallicity, despite the absence of spectrally resolved molecular features, comes in part from the dependence of H^- on metal fraction. The ionization of metals is the dominant source of free electrons that generate H^- opacity in the atmosphere, and so there is a direct link between the H^- continuum level and the abundance of metals. In particular, this is driven by the abundance of metals that are the dominant sources of free electrons (Na, K, and Ca; Longstaff et al. 2017). However, the complex relationship between the chemistry and the temperature structure as well as their joint effects on the spectrum make it difficult to attribute the retrieved metallicity solely to the H^- continuum.

The nominal self-consistent temperature pressure profiles (Figure 2.2) show a thermal inversion with temperature increasing with altitude at pressures between 0.1-0.01 bar. The inverted T-P profiles are also required to fit the emission feature at 4.5 μm, due to CO and H_2O, as observed with Spitzer (Nymeyer et al., 2011; Maxted et al., 2013). This inversion in our models is caused by high altitude absorption of optical stellar light by TiO and VO, and reduced cooling due to the dissociation of water. Vertical cold trapping of TiO can act to remove this species from the atmosphere of hot Jupiters (e.g., Désert et al. 2008), but not for planets with equilibrium temperatures above $\sim$1900 K (Parmentier et al., 2016). Horizontal cold trapping could still remove inversions from gas giants with high surface gravities (Parmentier et al., 2013; Beatty et al., 2017), however we do not see this in WASP-18 b as our modelling favours an atmosphere with a TiO driven inversion. In order to test the presence of the inversion we perform a second grid retrieval, but with the opacities of TiO and VO removed. Practically, this removes the temperature inversion for the cases where the C/O < 0.8. For higher C/O, oxygen-poor atmospheres are naturally depleted in TiO/VO so they can no longer be the source of the inversion. By comparing the Bayesian Information Criterion (BIC) we found that the models including TiO and VO were favoured (ΔBIC=6.5) over those without, at odds with the retrieval by Sheppard et al. (2017). Even though TiO/VO are present in our model, their features are not seen in the WFC3 bandpass as they are damped by the H^- continuum while also being partially dissociated (seen in Figure 2.1). We finally compare the BIC between the best-fit model spectrum and the blackbody fit and find that the best-fit model to the combined HST/WFC3 and Spitzer/IRAC data is favoured over the isothermal atmosphere (ΔBIC=12). Hence, our best fit favours a dayside model atmosphere with a solar metallicity and C/O ratio, and with a thermal inversion.

The abundance of water in the atmosphere is expected to be partially depleted by dissociation (see Figure 2.2). While water is not dissociated at the pressure levels probed by the WFC3, dissociation of water higher in the atmosphere (below 0.1 bar) removes its emission feature at 1.4 μm. If dissociation were not present, the line centre of emission would originate from higher in the atmosphere where the temperature is greater. We therefore attribute the the lack of water emission features both to an increased continuum opacity from H- and to decrease in line opacity by dissociation of water higher in the atmosphere. The final spectrum between 1.1-1.7 μm therefore appears featureless as it is a sum of broad, partially-depleted water emission at 1.4 μm and H^- bound-free opacity between 1.1-1.4 μm

(see also Parmentier et al. in prep.). However, the dominant effect in the case of WASP-18 b is the increased continuum opacity from H- over the thermal dissociation of water (brown contours, Figure 2.2).

Another effect of water dissociation at low pressures is that it reduces the ability of the atmosphere to cool in this region (Mollière et al., 2015). Hence in our models, even though the partial dissociation of TiO reduces the heating of the upper atmosphere, the atmospheric cooling efficiency remains lower than the heating efficiency, producing a thermal inversion.

2.4 Consequences for the family of very hot giant exoplanets

Our results for WASP-18 b have consequences for the new family of very hot gas giants, where extrapolation from cooler planets can be misleading (WASP-33 b: Haynes et al. 2015, WASP-103 b: Cartier et al. 2017, WASP-18 b: Sheppard et al. 2017, WASP-121 b: Evans et al. 2017). We find that the important impact of opacity both from H^- formed from metal ionization and from the reduced abundance of species, including water, due to thermal dissociation is key to the interpretation of very hot gas giant atmospheres. An evidence for this is that when including H^- opacity, the metallicity and C/O of WASP-18 b are no longer super-solar, but drop to solar values. This is expected for typical formation scenarios of such a massive planet. Our result implies that the metallicity and C/O of other recently found metal-enriched very hot gas giants could also drop to solar values when H^- opacity is considered.

Interestingly, almost all of the very hot gas giants probed so far are best explained with the presence of a thermal inversion. Indeed, the primary diagnostic of these thermal inversions is a flux excess at 4.5 μm (Knutson et al., 2010). This implies that the hottest exoplanets exhibit a common behaviour in their temperature structures, whose origin could be due to optical absorbers such as TiO/VO. Our modelling suggest that the WFC3 observations probe the region near the tropopause that is quasi-isothermal, and appears to produce blackbody-like spectra due to the combined effects of dissociation and H^- opacity. Thus, we postulate that transition regions in classes of hot Jupiters could occur around temperatures near 2500 K (HAT-P-7 b, Mansfield et al. in prep.), below which H^- opacity becomes less significant, and near 1800 K, below which TiO and VO condense.

We thank Christiane Helling and Mickael Bonnefoy for useful discussions, and Eliza Kempton for providing feedback on the manuscript. J.M.D. acknowledges that the research leading to these results has received funding from the European Research Council (ERC) under the European Union's Horizon 2020 research and innovation programme (grant agreement no. 679633; Exo-Atmos). J.M.D acknowledges support by the Amsterdam Academic Alliance (AAA) Program. Support for program GO-13467 was provided to the US-based researchers by NASA through a grant from the Space Telescope Science Institute, which is operated by the Association of Universities for Research in Astronomy, Inc., under NASA contract NAS 5-26555. J.L.B. acknowledges support from the David and Lucile Packard Foundation. M.R.L. acknowledges the ASU A2D2 Saguaro and Agave computer clusters used for the bulk of the grid model computations.

Wavelengths μm	Fp/Fs ppm	Error ppm	Model ppm	Wavelengths μm	Fp/Fs ppm	Error ppm	Model ppm
1.140-1.173	775	20	805	1.436-1.469	1131	21	1140
1.173-1.206	874	20	870	1.469-1.501	1190	21	1187
1.206-1.239	908	20	883	1.501-1.534	1237	21	1192
1.239-1.271	908	19	917	1.534-1.567	1171	23	1221
1.271-1.304	940	19	959	1.567-1.600	1205	24	1245
1.304-1.337	989	20	986	3.6	3020	150	3081
1.337-1.370	1050	20	1043	4.5	3850	170	3601
1.370-1.403	1105	20	1077	5.8	3700	300	4043
1.403-1.436	1141	21	1108	8.0	4100	200	4512

Table 2.1: Extracted secondary eclipse spectrum, including photometric Spitzer/IRAC points from Maxted et al. (2013) and Nymeyer et al. (2011) and best fit model from our grid-retrieval, convolved to the resolution of the data. Eclipse depths and 1σ errors for HST/WFC3 were obtained using MCMC analysis on each of the spectroscopic light curves.

Chapter 3

Climate of an Ultra Hot Jupiter: Spectroscopic phase curve of WASP-18b with HST/WFC3

Jacob Arcangeli, Jean-Michel Désert, Vivien Parmentier, Kevin B. Stevenson, Jacob L. Bean, Michael R. Line, Laura Kreidberg, Jonathan J. Fortney, Adam P. Showman

Astronomy & Astrophysics, Volume 625, Article 136

Abstract

We present the analysis of a full-orbit, spectroscopic phase curve of the ultra hot Jupiter WASP-18b, obtained with the Wide Field Camera 3 aboard the Hubble Space Telescope. We measure the planet's normalized day-night contrast as >0.96 in luminosity: the disk-integrated dayside emission from the planet is at 964±25 ppm, corresponding to 2894±30 K, and we place an upper limit on the nightside emission of <32ppm or 1430K at the 3σ level. We also find that the peak of the phase curve exhibits a small, but significant offset in brightness of 4.5±0.5 degrees eastward.

We compare the extracted phase curve and phase resolved spectra to 3D Global Circulation Models and find that broadly the data can be well reproduced by some of these models. We find from this comparison several constraints on the atmospheric properties of the planet. Firstly we find that we need efficient drag to explain the very inefficient day-night re-circulation observed. We demonstrate that this drag could be due to Lorentz-force drag by a magnetic field as weak as 10 Gauss. Secondly, we show that a high metallicity is not required to match the large day-night temperature contrast. In fact, the effect of metallicity on the phase curve is different from cooler gas-giant counterparts, due to the high-temperature chemistry in WASP-18b's atmosphere. Additionally, we compare the current UHJ spectroscopic phase curves, WASP-18b and WASP-103b, and show that these two planets provide a consistent picture with remarkable similarities in their measured and inferred properties.

However, key differences in these properties, such as their brightness offsets and radius anomalies, suggest that UHJ could be used to separate between competing theories for the inflation of gas-giant planets.

3.1 Introduction

Ultra hot Jupiters (UHJs) are gas giants on short orbital periods, typically around early type stars, with dayside temperatures of 2500 K or more. Bright star surveys, such as WASP (Pollacco et al., 2006), KELT (Pepper et al., 2007, 2012), MASCARA (Snellen et al., 2012), are specialised for finding these planets as they are some of the best targets for testing atmospheric theories. This is principally because their high temperatures makes them ideal targets for atmospheric spectroscopy. They also make for convenient chemical laboratories as all of their atmospheric constituents are expected to be in gas phase on their daysides (Parmentier et al., 2016).

Recent works in the near infrared, supported by observations with the Hubble Space Telescope (HST), have identified the key physics and chemistry that operate at these high temperatures, which can bias retrievals that have been honed on cooler planets. In particular, the dissociation of molecules at low pressures and high temperatures, as well as the opacity of H^- and other molecules strongly influence UHJ spectra (Bell et al. 2017; Arcangeli et al. 2018; Kitzmann et al. 2018; Kreidberg et al. 2018; Lothringer et al. 2018; Mansfield et al. 2018; Parmentier et al. 2018).

UHJs are expected to be tidally locked, ensuring that their daysides are always heated by their host star while their nightsides are permanently dark. Dayside emission spectra have shown that the majority of the incoming stellar flux must be re-emitted from the daysides of these planets, rather than re-distributed to the nightsides or reflected (e.g. Charbonneau et al. 2005; Deming et al. 2005; Désert et al. 2011c,b). However, these inferred dayside properties are not representative of their global atmospheres, and an understanding of these planets requires consideration of their full 3D atmospheres (Line & Parmentier, 2016; Feng et al., 2016). To that end, phase-curve observations allow us to resolve the longitudinal variation in temperature on a planet, and constrain its atmospheric circulation (Knutson et al., 2007; Borucki et al., 2009; Snellen et al., 2009). Spectroscopic phase curves, with instruments such as HST, allow us to further break the degeneracies between composition and temperature-structure from the day to the nightside of hot Jupiters (Stevenson et al., 2014c; Kreidberg et al., 2018).

Phase-curve observations measure key observables, namely the day-to-night contrast of the planet and the brightness offset from the substellar point, that inform the relative balance of wind recirculation and dayside re-radiation (Cowan et al., 2007). Circulation in hot Jupiters, to first order, can be seen as a balance of two key timescales. These are the radiative and advective timescales, that between them control how efficiently incident dayside flux can be re-distributed to the nightside of the planets (Showman & Guillot, 2002).

Large brightness offsets have been observed in thermal phase curves of hot Jupiters, pointing toward longitudinally asymmetric temperature distributions. The majority of these planets

have temperatures hotter east of the substellar point (see Knutson et al. 2012; Cowan et al. 2012; Parmentier & Crossfield 2018). These eastward offsets are attributed to fast equatorial winds, and are reproduced in first order by Global Circulation Models (GCMs). In these models, it is shown that a super-rotating equatorial jet can form in a hot Jupiter atmosphere and efficiently re-circulate energy from the dayside to the nightside (Showman & Guillot, 2002; Showman & Polvani, 2011). Several planets exhibit westward brightness offsets, the majority of which are dominated by reflected light. Hence these offsets are probing the cloud distribution which is anti-correlated with the temperature map. There are two exceptions to this: HAT-P-7b exhibits a time-variable phase-curve offset (Armstrong et al., 2016), and CoRoT-2b exhibits a strong westward offset in it's Spitzer phase curve (Dang et al., 2018). The time variable offset of HAT-P-7b may be explained by an oscillation of the equatorial wind triggered by MHD effects (Rogers, 2017). However, magnetic interactions are unlikely to explain the case of CoRoT-2b (Hindle et al., 2019), whose brightness offset may originate from asynchronous rotation (Rauscher & Kempton, 2014). The question remains how the observed circulation patterns extend from the classical hot Jupiters to the population of Ultra hot Jupiters, where the additional chemistry and physics that has been identified will influence their circulation.

Due to the high temperatures encountered in UHJ atmospheres, a third timescale is expected to be important, namely the dissipative, or drag, timescale. Strong drag is predicted to occur in the photospheres of UHJ, as their atmospheres should be partially ionized, leading to magnetic braking of waves on the dayside by the planetary magnetic field that acts to impede the formation of an equatorial jet (Perna et al., 2010a). While magnetic braking is not the only source of drag expected to occur in these atmospheres, its strength depends on the ionization fraction and therefore temperature of the atmosphere. Hence the expectation is that highly irradiated objects should have larger day-night contrasts, which is supported by several observations (Komacek et al., 2017; Parmentier & Crossfield, 2018).

An ideal test case for these theories is the planet WASP-18b (Hellier et al., 2009), which has a high equilibrium temperature of 2413K (Southworth et al., 2009) at a period of 0.94 days, placing it firmly in the population of ultra hot Jupiters. In particular, it has a high mass of 10 M_{Jup}, occupying the extreme end of the planetary mass regime. This mass places it close to the brown-dwarf regime, who are known to host magnetic fields with a range of field strengths. A planetary magnetic field could have several effects on the planet's observed phase curve and properties: on the day-night contrast through a magnetic drag (Perna et al., 2010a), on the brightness offset through magnetic instabilities (Rogers & Komacek, 2014; Dang et al., 2018), or on the radius through Ohmic dissipation (Batygin & Stevenson, 2010).

In this work, we present an analysis of the spectroscopic phase curve observed with HST Wide Field Camera 3 (WFC3), the third spectroscopic phase curve with HST to be published after WASP-43b and WASP-103b (Stevenson et al., 2014c; Kreidberg et al., 2018). In Section 2 we explain the observations and data reduction methods used. In Section 3.3 we present the results of the white-light phase curve fitting and phase-resolved emission spectra. In Section 3.4 we describe the Global Circulation Models used to interpret these results, and the broad properties of WASP-18b that are inferred from this comparison. In Section 3.5

we further discuss the importance of drag and it's effect on Ohmic dissipation, as well as comparing models with different compositions. We also place the results of this work in context with with previous analyses of spectroscopic phase-curves, in particular comparing to the UHJ WASP-103b. A final summary of our conclusions is presented in Section 3.6.

3.2 Observations and Data Reduction

3.2.1 Observations

We observed one phase curve of the hot Jupiter WASP-18b with the Hubble Space Telescope (HST), Cycle 21 Program GO-13467 (PI J. Bean). This phase-curve observation used a total of 18.5 HST orbits over two consecutive visits, covering 2 secondary eclipses and one primary transit of the system. The data were obtained with the Wide Field Camera 3 (WFC3) aboard HST with the G141 grism, covering 1.1 to 1.7μm. Details of the observations can be found in Arcangeli et al. (2018) along with a full analysis of the dayside spectrum. In this work we focus on the spectroscopic phase curve. These visits were taken using the 512x512 subarray (SPARS10, NSAMP=15, 112s exposures) in the bi-directional spatial scanning mode, with a half orbit break just before the last secondary eclipse due to a necessary gyro-bias update. We used our custom data reduction pipeline on the intermediate ima outputs, outlined in Arcangeli et al. (2018).

3.2.2 Systematics correction

The reduced light curves are dominated by instrument systematics which must be removed in order to extract the planet signal and system parameters (see Figure 3.1). We parametrise the orbit long systematics with a single exponential in time and the visit long systematics with a quadratic function in time, as these have been shown to match well the instrument systematics intrinsic to HST observations (Stevenson et al., 2014c; Kreidberg et al., 2014b). Consistent with previous analyses, we remove the first orbit of the visit due to the extreme ramp-amplitude, as well as the half-orbit before the second eclipse due to poor sampling of the ramp. We parametrise the phase curve with a simple two sinusoid model, which is analogous to a Spherical Harmonics model of degree 2. Kreidberg et al. (2018) show that, while the Spherical Harmonics model performs best for the data they analyzed, different phase-curve models can lead to very different temperature maps for the same data. This is due to the intrinsic degeneracy between the measured signals, that can lead to different temperature maps for the same planet (Cowan et al., 2012). For the case of WASP-18b, the large mass of the planet should cause significant tidal deformation of the stellar host. The magnitude of this effect is poorly constrained theoretically due to the uncertainty on the stellar density distribution (see Section 3.3.2). This introduces another degeneracy in the extraction of the planet's signal, hence we choose not to explore different phase-curve models, and only constrain the day-to-night contrast and brightness offset of the planet's phase curve, as they remain consistent between different phase-curve models (Kreidberg et al., 2018). Finally, we do not include the reflected light component in our models, as

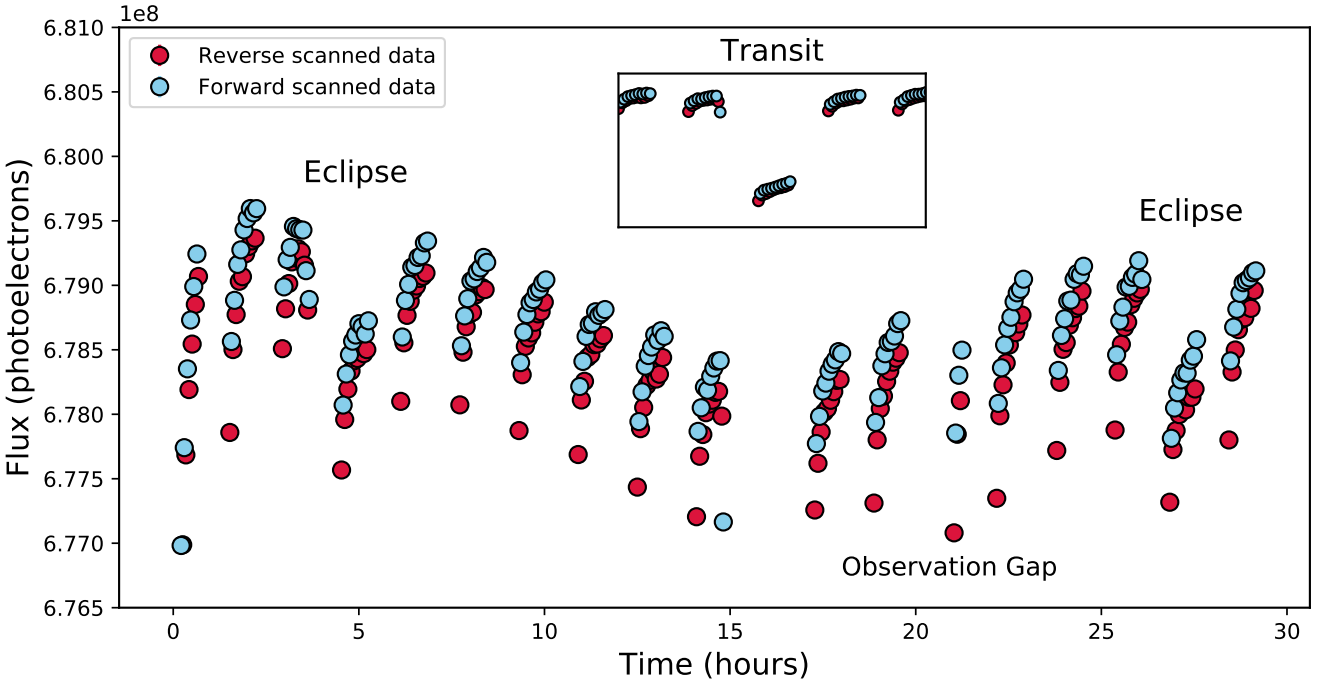

Figure 3.1: Raw observed phase curve of WASP-18b, before removal of systematics and stellar variation. The transit is shown in the inset. The observations cover two eclipses to establish a baseline, with one transit in the middle of the observations. There is an additional half-orbit gap in the observations at 20 hours due to a gyro bias update. Clear orbit-long systematics can be seen, as well as a visit-long slope, on top of the phase-curve variation. The two colours signify the exposures taken from each of the two spatial scan directions, where there is an offset due to the fixed read-out pattern of the detector.

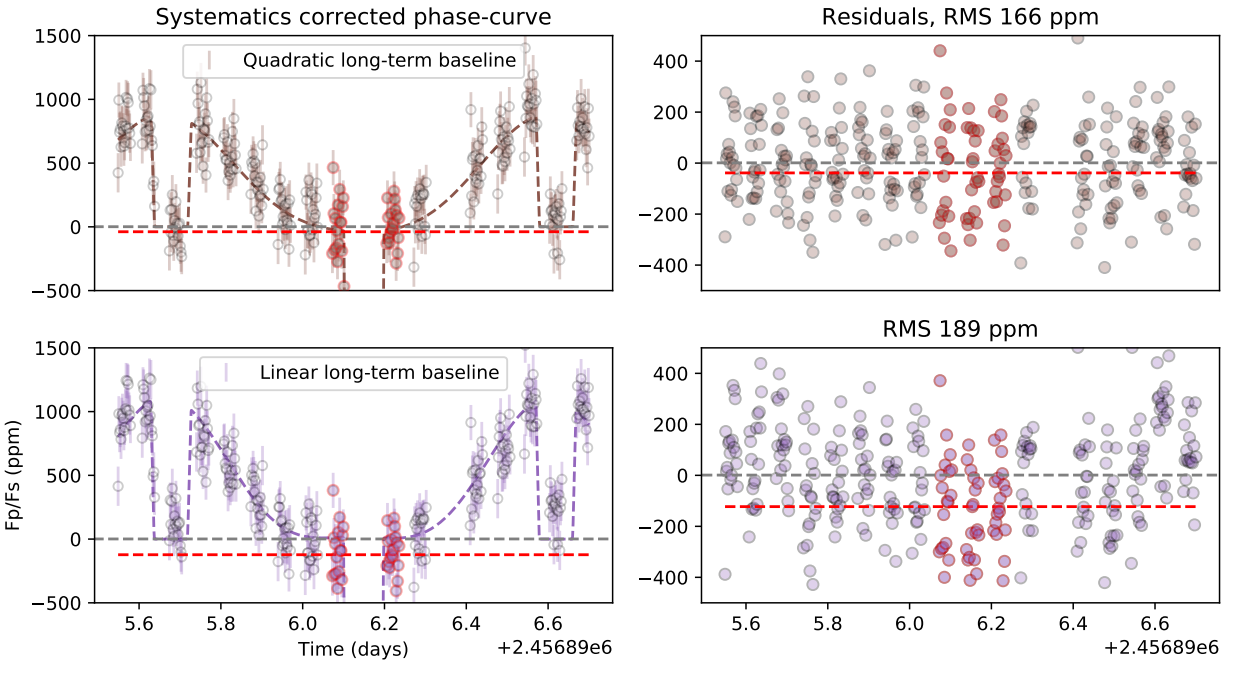

Figure 3.2: Effect of systematic, long-term slope model on extracted phase curve. Left panels: systematics corrected phase curve and best-fit model for the wavelength bin 1.27-1.30 μm. Right panels: the same residuals plotted in time. The red line is the mean of the nightside residuals. In both panels, the exposures used to calculate the nightside residuals are outlined in red. Using a linear visit-long systematics model degrades the precision of the light curve, introduces visible systematics in the residuals, and results in a significant negative nightside flux.

the albedo of the planet is found to be $A_g < 0.057$ (Shporer et al., 2019), which should contribute to <5% of the total planetary flux at these wavelengths.

We first test our ability to detect the nightside flux in this data by fixing the in-eclipse fluxes to the baseline stellar flux level, and allowing the nightside level to be completely free. We found that we were unable to detect the nightside flux of the planet at a significant level, and in many cases the measured nightside of the planet was below the flux of the star, requiring a negative contribution from the planet which is unphysical (e.g. Keating & Cowan 2017). This is, in part, because the signal of the nightside is expected to be very small compared to the amplitude of the systematics, Fp/Fs<30 ppm for a nightside temperature of 1400K not unexpected for such a system (Perez-Becker & Showman, 2013). Hence, we opted to enforce that the phase-curve model should never fall below the in-eclipse flux, after correcting for systematics and ellipsoidal variations. A stronger constraint would be to enforce that the brightness map of the planet should be non-negative (Keating & Cowan, 2017). Since odd map harmonics discussed in Keating & Cowan (2017) are not constrained by our data, as they cannot be seen in the phase light curve, and their inclusion or exclusion can change the brightness map of the planet, we opt to only enforce that the phase light curve remain non-negative. We choose not to discuss the brightness map of the planet, as the conversion from phase light curve to brightness map is not unique (Cowan & Agol, 2008). We verify that, for our best fit parameters, the brightness map can also be made non-negative with the inclusion of odd map harmonics, and hence our results do not require an unphysical brightness map.

In order to reduce the number of degeneracies in our models, we explored the possibility of a linear visit long systematics model rather than a quadratic model. We found that the fit quality of the linear slope model was worse at all wavelengths when compared to the quadratic model, both with and without a non-negative phase-curve prior. The linear slope also strongly favoured a negative nightside flux when the nightside was set free (shown in Figure 3.2). Here the quadratic slope model resulted in a nightside flux of -107±46 ppm (consistent with zero at the 3σ level) whereas the linear slope model found a nightside flux of -321±24 ppm. Finally, the residuals between the best-fit linear-slope model and the data showed clear systematic trends in time, indicating that the model was not fully capturing the data.

$$
\begin{aligned}
M(t) = & \Big\{ \Big[1 + \boldsymbol{E_C} \sin(4\pi(\phi(t) - E_\phi)) \\
& \quad + D_C \sin(2\pi(\phi(t) - D_\phi))\Big] * T_0(t) \\
& + \Big[\boldsymbol{c_{fp}} + \boldsymbol{c}_1 \cos(2\pi(\phi(t) - \boldsymbol{c}_2)) \\
& \quad + \boldsymbol{c}_3 \cos(4\pi(\phi(t) - \boldsymbol{c}_4))\Big] * \boldsymbol{E}_0(t) \Big\} \\
& * \boldsymbol{C_{scan}} * \left(1 + \boldsymbol{V}_1 t + \boldsymbol{V}_2 t^2\right) * \left(1 - \boldsymbol{R_{orb}} e^{-t_{orb}/\boldsymbol{\tau}}\right)
\end{aligned} \tag{3.1}
$$

Equation 3.1 shows the full model fitted to the data, where fitted parameters are shown in bold (ϕ is the orbital phase of the planet at a given time, t is the time since the beginning of

the visit, and t_{orb} is the time since the beginning of an orbit). $T_0(t)$ and $\boldsymbol{E}_0(t)$ are the transit and eclipse models respectively, calculated using the batman package (Kreidberg, 2015), where we fit for the mid-eclipse time ($\boldsymbol{dt}1$) and eclipse depth (through the phase curve parameters). The stellar variations are parametrised by the magnitude of the ellipsoidal variations ($\boldsymbol{E_C}$), fixed to reach its minimum at transit and eclipse ($E_\phi = 0$), while the Doppler boosting signal is fixed to our calculated value of 22 ppm (see Section 3.3.2). The planet signal is modelled by a two-component sinusoid, consisting of 5 free parameters ($\boldsymbol{c_{fp}}$, $\boldsymbol{c}_{1-4}$). Finally, the instrument systematics are parametrised by the model-ramp approach (Kreidberg et al., 2014b; Stevenson et al., 2014b). This consists of a quadratic visit-long slope ($\boldsymbol{C_{scan}}, \boldsymbol{V}_1, \boldsymbol{V}_2$) and an exponential decay in time for each orbit ($\boldsymbol{R_{orb}}, \boldsymbol{\tau}$). $\boldsymbol{C_{scan}}$ is the only parameter that is different for each scan direction, and both scan directions are fitted simultaneously. The exponential ramps in each orbit of HST are seen to be stable in time, but are significantly larger in the first orbits of a visit. We therefore allow the first two orbits of the visit, as well as the first orbit after the half-orbit gap, to be fitted with their own ramp amplitudes whilst fixing the other ramp amplitudes to all be equal. We therefore fit for 4 $\boldsymbol{R_{orb}}$ for each light-curve ($\boldsymbol{R}_{1-4}$).

For each of the wavelength dependent light-curves, the ramp timescale, the ellipsoidal variation, and the eclipse time are fixed to the white-light curve values ($\boldsymbol{\tau}, \boldsymbol{E_C}, \boldsymbol{dt}1$). The remaining parameters are fitted for each channel. We experiment with allowing the ellipsoidal variations to be fitted at each wavelength with a gaussian prior determined by the white-light curve fit, and our results remain consistent. This leads to a total of 16 free parameters for the white-light curve fits and 13 free parameters per spectroscopic channel. We fix the remaining system parameters, such as the period and planet/star radius ratio, to values from Southworth et al. (2009).

The rms of the residuals of the spectroscopic phase-curve fits is between 10-30% above photon-noise for all bins. The resulting white-light curve fit is shown in Figure 3.3 in black and the systematics-corrected data are shown in blue. We find that the residual rms of the best fit to the white-light curve is significantly above photon noise (105 ppm, or 65 ppm above), similar to Kreidberg et al. (2018). We include a table of our best-fitting parameters in the appendix as well as a corner plot of the posteriors from the white-light curve fit.

3.2.3 Estimation of Errors

In order to estimate the errors on our fitted parameters and identify the degeneracies in the model we use a Markov-Chain Monte Carlo approach using the open-source `emcee` code (Foreman-Mackey et al., 2013). Each of the parameters are given flat priors within an acceptable range. We test the inter and intra chain convergence by employing the Gelmaan-Rubin diagnostic for each of our runs. We run chains of 2,000 steps with 50 walkers to achieve convergence over all parameters.

3.3 Results

3.3.1 Observed phase-curve properties

The extracted white-light phase curve shows a large day-to-night contrast, with a peak at 964±25 ppm just before secondary eclipse and a minimum <32 ppm at 3σ level of confidence just before the primary transit (see Figure 3.3). We find that day-night contrast is >0.96 in luminosity, defined here as the difference between the dayside and nightside phase-curve amplitude divided by the dayside amplitude. The peak of the phase curve comes before the secondary eclipse, with a 4.5±0.5 degree offset of the brightest point eastward in phase. We fit a blackbody for the planet to the dayside spectrum obtained with HST/WFC3, and find a dayside temperature of 2894±30 K. We place an upper limit on the nightside temperature of 1430 K at the 3σ level. For the spectrum of the star, we use the ATLAS9 model atmospheres grid (Castelli & Kurucz, 2004), propagating uncertainty on the stellar effective temperature and planet-star radius ratio, taken from Hellier et al. (2009). These uncertainties on the system parameters correspond to a systematic uncertainty of 25 K on the planet temperature.

These results are consistent with previous phase curves of WASP-18b by Maxted et al. (2013) using Spitzer photometry at 3.6 and 4.5 μm. They find no evidence of a brightness offset, at a 1σ precision of 5 & 9 degrees in their respective channels, and are unable to detect the nightside of the planet.

We extract the emission spectrum of the planet at different orbital phases (show in Figure 3.4). We find that the phase-resolved spectra do not exhibit identifiable molecular features of water expected at these wavelengths. The spectra closely resemble blackbody emission at all phases, with decreasing temperature away from the secondary eclipse as expected for a tidally locked planet. This is likely explained by the dayside flux as measured by Arcangeli et al. (2018) dominating the emission spectrum at all phases due to the large day-night luminosity contrast (see also Parmentier et al. 2018, Fig. 10).

We additionally measure the offset of the brightest point in the phase curve in each of our 14 wavelength bins (shown in Table 3.1) and find that the offset remains constant with wavelength within our uncertainties. We therefore combined the measured offset from each wavelength bin to calculate a white-light curve offset of 4.5±0.5 degrees eastward in longitude. These brightness offsets are not directly equivalent to hot-spot offsets in the thermal map of the planet, as they measure the offset in integrated hemispheric brightness (Cowan & Agol, 2008; Schwartz et al., 2017). In future discussions we compare only to the brightness offset seen in our data, as the inversion from the light curve to a longitudinal brightness map is not unique.

3.3.2 Ellipsoidal variations

We explored the effects of tidal deformation of the star by the planet and of the planet by the star. Since the mass of the planet is large at 10 M_{Jup}, and the planet is only separated

Wavelengths μm	Eastward Offset degrees	Error degrees
1.14-1.17	5.1	2.5
1.17-1.21	2.8	2.6
1.21-1.24	3.8	2.1
1.24-1.27	6.3	2.1
1.27-1.30	5.4	2.0
1.30-1.34	6.8	2.4
1.34-1.37	4.5	1.9
1.37-1.40	2.5	1.7
1.40-1.44	6.8	2.0
1.44-1.47	3.3	1.6
1.47-1.50	5.8	1.7
1.50-1.53	5.1	1.9
1.53-1.57	3.4	1.7
1.57-1.60	1.6	1.3
1.14-1.60	4.5	0.5

Table 3.1: Measured brightness offsets for each spectroscopic phase curve. The offsets at each wavelength are consistent with the mean of 4.5±0.5 degrees to within one or two sigma.

by 3.6 Stellar radii from the star, both can have a significant impact on the observed phase curve.

We use the equations supplied in Leconte et al. (2011a) and estimate that the stellar ellipsoidal variations are of order 200 ppm, or 400 ppm peak-to-peak. The size of these variations is uncertain due to the uncertainty on the stellar density distribution. Since the ellipsoidal variations operate on the same timescale as our phase-curve model, they are a significant source of degeneracy. We include the magnitude of the ellipsoidal variations in our fits and remove them from our final light curves. The fitted magnitude of the stellar ellipsoidal variation is 201±26 ppm in the white-light curve, with a phase offset fixed such that the minima are at secondary eclipse and transit (shown as the cyan curve in Figure 3.3). We fixed the magnitude of the ellipsoidal variations to the white-light curve values in each of the spectroscopic phase curves.

Interestingly, our measurement of the stellar ellipsoidal variation is consistent with the independent measurement of the ellipsoidal variations by Shporer et al. (2019) to within the 1σ confidence level. Shporer et al. (2019) measured the amplitude of the ellipsoidal variations as 194±7 ppm using observations from the *TESS* spacecraft in the optical. Additionally the dayside emission of WASP-18b measured with *TESS* is consistent with our dayside emission spectrum, as discussed in Shporer et al. (2019). However, while the planetary emission at other phases is consistent within the errorbars of Shporer et al. (2019) and this work, the differences in how the planetary signal is extracted make a comparison difficult. For instance the nightside flux in *TESS* is measured at -24 ppm, whereas our approach enforces

that the nightside signal is non-negative. We do not fix our ellipsoidal variations to the more precise measurement from Shporer et al. (2019) in order to allow us to compare the two results as independent measurements. We do however test our analysis using their value of EC=194±7ppm, and find our conclusions unchanged. The most significant effect of including their more precise measurement is an increased precision on the phase curve at quadrature, where the ellipsoidal variations peak.

We estimate the inverse effect, the tidal deformation of the planet by the star, using the tables supplied in Leconte et al. (2011b) for a $10M_J$ planet under high irradiation. We find that the expected size of the planet's variations are only an effective 0.25% in radius, equivalent to 5ppm in the final light curve, which should be negligible at our precision and is well within the errors on the measured radius of the planet of $\pm 6\%$ (Southworth et al., 2009). We also estimate the effect of doppler boosting due to the radial velocity of the star on these light-curves to be about 22 ppm (Mazeh & Faigler, 2010), and include it in our models fixed to this value. This is also consistent with the measurement of 24±6 ppm by Shporer et al. (2019).

An additional effect of the ellipsoidal variations is that they may offset any measurements of the transit or eclipse depths when unaccounted for (e.g. Cowan et al. 2012). This effect is mitigated in the case of WASP-18b, as the planet's phase-curve variation within the HST/WFC3 bandpass is by coincidence nearly equal in magnitude to the ellipsoidal variations over the duration of the eclipse. We estimate the difference in the retrieved eclipse depths, when the phase-curve and ellipsoidal variations are fixed to our best-fit values versus when they are unaccounted for, and modelled as instrument systematics. When these effects are not accounted for, we find a relative change in eclipse depth of only 3 ppm over the whole spectrum, well below the precision of the data, and a systematic over-estimate of the eclipse depths (offset) of about 20 ppm or ∼2% of the depth. These changes are within the 1-sigma errors of Arcangeli+2018. However, we stress that for other planets where these effects do not necessarily cancel, it has been shown that their treatment can significantly affect inferred eclipse depths (Cowan et al., 2012; Kreidberg et al., 2018).

3.4 Comparing the phase curve of WASP-18b to Global Circulation Models

3.4.1 Global Circulation Models

To interpret our data and determine the physical origin of the observed signals, we compare the extracted phase curve and spectra to 3D Global Circulation Models (GCMs). We produced a sample of circulation models, exploring the effects of changing drag and metallicity as these have been shown to determine the broad behaviour of hot Jupiter phase curves (Showman & Polvani, 2011; Kataria et al., 2015). Here drag refers to any dissipative mechanism that can act to slow down wave propagation and reduce windspeeds.

The atmospheric circulation and thermal structure were simulated using the SPARC/MITgcm model (Showman et al., 2009). The model solves the primitive equations in spherical

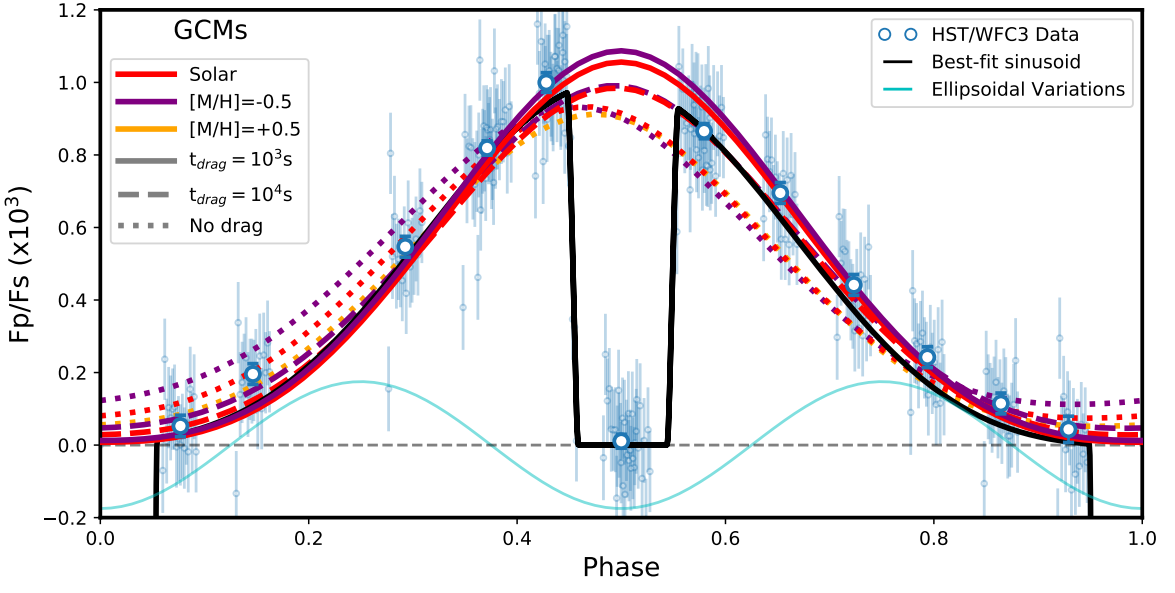

Figure 3.3: Systematics-corrected HST/WFC3 white-light phase curve of WASP-18b (blue points) compared to suite of Global Circulation Models (coloured curves). In black is the best-fit model used to parametrize the planet signal, with two sinusoidal components for the phase-curve variation. In cyan are the stellar ellipsoidal variations, that have been subtracted from the phase curve (see Section 3.3.2). GCMs shown are parametrized by 3 drag timescales indicated by line-styles and by 3 metallicities indicated by colours (-0.5, 0.0, and +0.5 relative to solar).

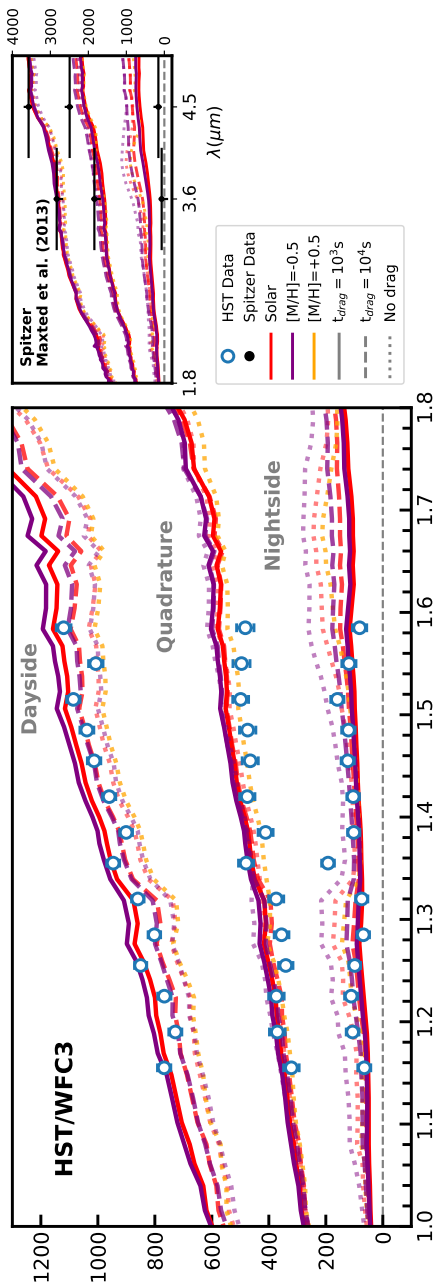

Figure 3.4: HST/WFC3 phase-resolved spectra at three different phases (dayside, nightside, and quadratures) compared to range of GCMs. Spitzer points are taken from the best-fit sinusoidal phase-curve model by Maxted et al. (2013), where the nightside was fixed to zero flux, with errorbars taken from their eclipse depth measurements. The phase bins shown are three broad bins: "Dayside" refers to orbits between phases 0.4-0.45 and 0.55-0.6, "Quadrature" to the average of phases 0.25-0.3 and 0.7-0.75, and "Nightside" to phases 0.05-0.25 and 0.75-0.95. The same binning is used for the GCM spectra shown.

geometry using the MITgcm (Adcroft et al., 2004) and the radiative transfer equations using a state-of-the-art one dimensional radiative transfer model (Marley & McKay, 1999). We use the correlated-k framework to generate opacities, based on the line-by-line opacities described in Visscher et al. (2006); Freedman et al. (2014). Our initial model assumes a solar composition with elemental abundances of Lodders & Fegley (2002) and the chemical equilibrium gas phase composition from Visscher et al. (2006). These calculations take into account the presence of H^- opacities and the effect of molecular dissociation on the abundances, shown to be important for this class of planet (Arcangeli et al., 2018; Kreidberg et al., 2018; Mansfield et al., 2018; Parmentier et al., 2018; Bell & Cowan, 2018). Additional heat transport by H_2 recombination is not included in our models (Bell & Cowan, 2018). We used a timestep of 25s, ran the simulations for 300 Earth days, averaging all quantities over the last 100 days. The above modelling process is the same as that described in Parmentier et al. (2018), using the WASP-18 system parameters from Southworth et al. (2009).

We include additional sources of drag through a Rayleigh-drag parametrisation with a single constant timescale per model that determines the efficiency with which the flow is damped. We vary this timescale between models from $t_{drag} = 10^{3-6}s$ (efficient drag), as well as a no drag model with $t_{drag} = \infty$. While all the models are radiatively dominated on the dayside, our range of drag strengths cover the transition from a drag-free, wind circulation case to a drag-dominated circulation. This can be seen from the short radiative timescale of the dayside photospheres of our models, $t_{rad} \sim 10^{2-3}$s, estimated using Eq. 10 from Showman & Guillot (2002) for a simple H_2 slab atmosphere. This is significantly shorter than other relevant timescales, such as the advective timescale at the equator, calculated as the ratio of the equatorial windspeed over the planet radius. The advective timescale is on the order of 10^4s in our no drag model rising to 10^6s in our efficient drag model ($t_{drag} = 10^3$s), as the model atmospheres transition to drag-dominated circulations.

3.4.2 Comparison of GCMs to data

To first order, all of our Global Circulation Models show a large day-night contrast and small or no brightness offset, and broadly reproduce the observed phase curve of WASP-18b. We find however that our baseline, solar-composition model with no additional drag sources fails to match the size of the day-night contrast in the phase-curve data (Figure 3.3). This baseline model both under-predicts the dayside flux and over-predicts the nightside flux of the planet. However, models with additional sources of drag, parametrised by a short drag timescale, are able to match better the dayside and nightside flux of the planet. All of our efficient drag models match well the day-night contrast of the planet. We therefore find that we require additional drag sources to explain our observed day-night contrast of WASP-18b. We discuss the possible physical origins of this additional drag in Section 3.5.1.

When generating our GCMs, we held the system parameters fixed to literature values. We were not able to explore their full uncertainties as generating one model is already computationally expensive. However, uncertainties on the system parameters will lead to an additional uncertainties on the inferred best-fit models. Since the differences between the

efficient drag models are so small, we cannot statistically choose between these models (see Table 3.2). Nevertheless, models with inefficient or no drag fail to reproduce the day-night contrast seen in the data and therefore the overall shape of the phase curve. Hence we can conclude that we require some additional source of efficient drag to explain our observed phase curve, and the best-fitting models are those with $t_{drag} = 10^3$s or 10^4s.

We test whether enhanced or depleted metallicity might also explain the large day-night contrast without the need for additional drag sources (Kataria et al., 2015). We find however that the effect of changing metallicity alone, in our models of WASP-18b, is too small to explain the observations (see Figure 3.3), but the effect of metallicity on the phase curve is different for these hot planets compared too cooler objects (see Section 3.5.3).

We also compare our GCMs to phase-resolved spectra extracted from the spectroscopic phase curve, as this allows us to study the wavelength dependence of our data. As seen in Figure 3.4, we find that the spectra are best matched by the efficient drag models. The phase-resolved spectra are dominated by thermal emission from the dayside due to the large day-night luminosity contrast.

Model t_{drag} (s)	Model [M/H]	$\Delta\chi^2$	$\Delta\chi^2$ per datum
10^3	-0.5	37	0.2
10^4	-0.5	0	0.0
no drag	-0.5	137	0.6
10^3	0.0	23	0.1
10^4	0.0	7	0.0
no drag	0.0	73	0.3
no drag	+0.5	70	0.3

Table 3.2: Table of the fit quality between our circulation models and the measured phase curve of WASP-18b, relative to the best fitting model. Fit quality here is measured by the χ^2 between the data and the circulation model.

3.5 Discussion

3.5.1 Drag in Global Circulation Models

3.5.1.1 Sources of drag

We infer the presence of an efficient drag source in the atmosphere of WASP-18b from our comparison to Global Circulation Models. We explore the origins of this drag, which could originate from a variety of sources, such as turbulence and instabilities (Goodman, 2009; Li & Goodman, 2010; Youdin & Mitchell, 2010), or hydrodynamic shocks (Dobbs-Dixon

et al., 2010; Rauscher & Menou, 2010; Heng, 2012; Fromang et al., 2016). Alternatively, for hot planets whose atmospheres are partially ionized, magnetic fields may influence the circulation and create a magnetic drag (Perna et al., 2010a; Batygin et al., 2013; Komacek et al., 2017). Magnetic drag, sometimes called "ion drag", is caused by the collision between the bulk neutral flow and the ionic component of the flow. Since the ionic component is subject to Lorentz forces but the neutral component is not, these ions can act as a drag and eventually dominate the circulation under the right conditions (Zhu et al., 2005).

Alkali metals in the dayside atmosphere of WASP-18b should be significantly thermally ionized (Arcangeli et al., 2018; Helling et al., 2019a). Thus, if WASP-18b were to host a magnetic field, its circulation would be influenced by magnetic drag. We use the formula described in Perna et al. 2010a (here Equation 3.2) to estimate what might be the efficiency of magnetic drag on this planet, parametrised through the timescale t_{drag}.

$$t_{drag} \sim \frac{4\pi\rho \cdot \eta(n_e)}{B^2 cos\theta} \quad \text{Perna et al. (2010a)} \tag{3.2}$$

This timescale t_{drag} is the timescale on which kinetic energy is dissipated by magnetic drag in the atmosphere. We calculated the ionization fraction in local chemical equilibrium for our circulation models with a modified version of the NASA CEA Gibbs minimization code (e.g. Gordon & McBride, 1994; Parmentier et al., 2018). This ionization fraction (n_e) is used to compute η, the resistivity, defined in Perna et al. (2010a). B here is the magnetic field strength, ρ is the density of the atmosphere, and $\pi - \theta$ is the angle between the magnetic field and the flow (assumed here that $\theta = 0$ for the case of maximal efficiency).

We find that we can match a t_{drag} of order 10^3s at the substellar point, rising to 10^4s elsewhere on the dayside, with a magnetic field strength of B=10 Gauss . The nightside drag timescale from our models is much longer, as the nightside is too cold for thermal ionization. This estimate shows that the short drag timescale inferred from our GCMs could reasonably be due to Lorentz forces. However, the inhomogeneity also highlights that our Rayleigh-drag parametrisation does not capture the full effects of magnetic drag, as for instance a magnetic drag timescale should vary throughout the atmosphere.

3.5.1.2 Limitations of Rayleigh drag parametrisation

In our GCMs, drag is parametrized by a simple Rayleigh drag (Komacek & Showman, 2016) which aims to approximate any additional drag sources by one single dissipative timescale throughout the planet, without the need for finer resolutions or full MHD calculations. This parametrization is shown in Equation 3.3, where the drag force per unit mass, $\mathcal{F}_{drag}$, is given as $\boldsymbol{v}$, the velocity of the flow, divided by t_{drag}, a single constant drag timescale.

$$\mathcal{F}_{drag} = -\frac{\boldsymbol{v}}{t_{drag}} \tag{3.3}$$

In the context of magnetic drag, this parametrization has three key problems. The first is that the magnetic drag is direction-dependent with respect to the magnetic field (Batygin et al., 2013) seen as the θ term in Equation 3.2. The second is that the strength of drag is spatially inhomogeneous, i.e. it is weaker in cooler regions where there is less ionization, such as the nightside hemisphere (Rauscher & Menou, 2012). Finally, the atmospheric circulation itself can induce a toroidal magnetic field that is larger in amplitude than the dipole field of the planet, that can change both the strength and the direction of the Lorentz force (Rogers & Komacek, 2014). All these aforementioned effects are not accounted for in our models which could limit our accuracy in predicting the shape of the phase curve.

3.5.2 Effect of a planetary magnetic field

3.5.2.1 Magnetic Circulation

Batygin et al. (2013) explored further the effect of the directionally-dependent Lorentz-force on atmospheric circulation. Our GCMs with very efficient drag exhibit longitudinally symmetric day-night flow patterns (top panel of Figure 3.5), as efficient drag shuts down Rossby and Kelvin waves in the dayside atmosphere that are responsible for the typical equatorial jet formation (Showman & Polvani, 2011). However Batygin et al. (2013) suggest that this should only occur on objects with low magnetic fields, typically with B<0.5 Gauss in strength. They predict that the majority of highly irradiated gas giant atmospheres should be dominated by zonal jets (Showman & Polvani, 2011), such as those seen in our drag free models (bottom panel of Figure 3.5). This is due to Lorentz-forces that act perpendicular to the magnetic field lines leading to circulation patterns with zonal jets, rather than simply damping the existing flow as in the Rayleignash-drag parametrization (Batygin et al., 2013). In contrast, without considering magnetic effects, drag due to other schemes such as the Kelvin-Helmholtz instability should lead to a symmetric day-night flow with no brightness offset. In this context, the presence of a brightness offset in our data might be an indication that magnetic effects are responsible for the observed circulation on WASP-18b, and therefore favour a magnetic drag scenario.

Magnetic drag should affect the circulation of cooler planets more than the Ultra hot Jupiters. As discussed in Perna et al. (2010a) for HD209458b (T_{eq}=1460K), magnetic drag may act to limit the wind speeds, but will not completely shut down re-circulation for magnetic fields with B<30 Gauss or so. This is because there is a direct dependence of the magnetic drag timescale on the resistivity of the atmosphere (see Equation 3.2). This resistivity depends strongly on the local temperature through the ionization fraction, which drops sharply even across the dayside of WASP-18b (see Helling et al. 2019a, Figure 6).

3.5.2.2 Ohmic dissipation in WASP-18b

Another consequence of a planetary magnetic field is Ohmic dissipation which has been proposed as a mechanism to explain hot Jupiter inflation (Batygin & Stevenson, 2010; Perna

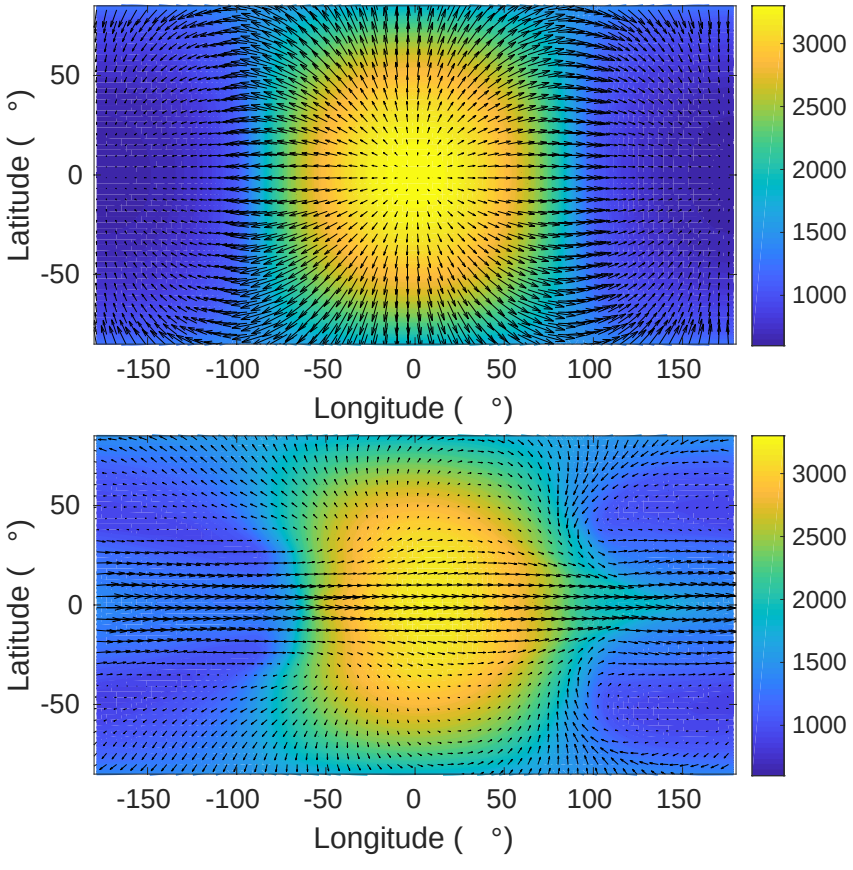

Figure 3.5: Temperature and wind maps of WASP-18b taken from GCMs at a pressure level of 0.2 bar for two cases of drag.
Top: Efficient drag model ($t_{drag} = 10^3$s), where the circulation is day-to-night and longitudinally symmetric.
Bottom: No drag model, the circulation to the nightside is more efficient and driven by an equatorial jet.

et al., 2010b; Menou, 2012). Here we consider what the effect of Ohmic dissipation would be on the measured radius of WASP-18b.

In the specific case of WASP-18b, there are two additional factors affecting the radius inflation by Ohmic dissipation due its high temperature and large mass. The first is that heating due to Ohmic dissipation should be less efficient in the presence of efficient drag, as the zonal winds that drive Ohmic dissipation are reduced in speed (Menou, 2012). The second is that inflation by Ohmic dissipation should be less efficient for higher mass planets (Huang & Cumming, 2012). This is because the depth at which Ohmic power is deposited depends on the scale-height of the atmosphere, and energy should be deposited higher in massive planet atmospheres than less massive planets. This would reduce the effect of any additional heating by Ohmic dissipation on the observed radius of massive planets.

These effects combined predict that WASP-18b should not be significantly inflated by Ohmic dissipation. Using predictions from Thorngren & Fortney (2018), a 10 M_J planet should have a maximum radius of 1.21 R_J when inflation effects are not taken into account. The measured radius of WASP-18b is consistent with this value within one sigma (1.204 ± 0.035 Maxted et al. 2013). The effect of inflation on the radius of high mass planets is harder to detect (Miller et al., 2009), however we can conclude that WASP-18b does not deviate from the scenario predicted by Ohmic dissipation. In Section 3.5.5, we show that we can lift some of this degeneracy between mass and inflation efficiency by comparing to a lower mass UHJ, WASP-103b.

3.5.3 Effect of Atmospheric Metallicity on the phase curve of WASP-18b

Previous work has shown that changes in atmospheric metallicity can affect global circulation in hot Jupiter atmospheres (Showman et al., 2009; Kataria et al., 2015). For instance, increasing the metallicity in a classical hot Jupiter model typically acts to reduce the planet's nightside emission (e.g. WASP-43b, Kataria et al. 2015). This is because, as the metallicity increases, the abundances of molecular species increase leading to stellar light being absorbed higher in the atmosphere, at lower pressures. The radiative timescale is shorter at lower pressures, leading to less efficient heat circulation to the nightside of the planet (Showman et al., 2009). Additionally, as more incident energy is re-irradiated from the dayside, the brightness temperature of the dayside increases with increasing metallicity for a classical hot Jupiter model (Kataria et al., 2015).

WASP-18b resides in a hotter regime, where for instance gas phase TiO becomes an important chemical species. For WASP-18b, an increase in atmospheric metallicity changes the abundance ratio of gas phase TiO vs H_2O above the photosphere (Parmentier et al., 2018). While TiO absorption increases the temperature above the band-averaged WFC3 photosphere, the temperature at the WFC3 photosphere decreases, as correspondingly less stellar light reaches photospheric pressures. Hence the planet's dayside is dimmer in the WFC3 bandpass in the higher metallicity case, but should be brighter in emission shorter than $1 \mu m$, inside the TiO bandpass. The reverse effect is seen when the metallicity is de-

creased: the temperature of the WFC3 photosphere is hotter but the nightside re-circulation is more efficient, leading to an increase in emission at all phases in the WFC3 bandpass.

Neither an enhancement or depletion of ± 0.5 in metallicity relative to solar is sufficient to match the observed phase curve of WASP-18b without including efficient drag in our models. However, there is a strong dependence of the nightside temperature with metallicity in our no-drag models (see Figures 3.3 and 3.4).

3.5.4 Constraints on the Redistribution

The redistribution efficiency determines the amount of flux that is re-emitted from the dayside versus the amount of flux that is carried to the nightside. It can be defined through the ratio of the dayside temperature and the equilibrium temperature of the planet: $f = (T_d/T_{eq})^4$. Here $f = 2$ refers to the dayside-only redistribution case, while $f = 2.67$ refers to the no-redistribution case (where the dayside reaches the maximum temperature). The redistribution efficiency can be used as a simple measure of the atmospheric circulation regime. We show the redistribution efficiencies for each of our GCMs in Figure 3.6 as the coloured points. All of our GCMs have redistribution factors between $2.2 < f < 2.5$.

These models for WASP-18b show that the redistribution efficiency is strongly dependent on metallicity in the case of no or weak drag. This can be seen as the steep dependence of redistribution efficiency with metallicity for the left-most points in Figure 3.6 (the weak drag regime). The origin of this effect is described in Section 3.5.3. For models with efficient drag, the dependence of redistribution on metallicity is greatly reduced. In these models the circulation becomes drag dominated and inefficient at all pressures, hence the effect of metallicity is less pronounced.

Typically the redistribution efficiency cannot be estimated solely from the dayside emission, as there is a known degeneracy between the albedo and the redistribution efficiency (Cowan & Agol, 2011). For UHJs, while the albedos are expected to be very small, we illustrate that the uncertainty on the equilibrium temperature limits any conclusions that could be drawn from the dayside alone. The redistribution efficiencies calculated in Arcangeli et al. (2018) adopted fixed stellar parameters during the retrieval process, fixing $T_{eq} = 2477$ K. This is offset from our GCMs, calculated using slightly different stellar parameters, leading to $T_{eq} = 2385$ K. We correct for this offset and include a systematic uncertainty of $\Delta f = \pm 0.18$ from $\Delta T_{eq} = \pm 44K$ (Southworth et al., 2009). In Figure 3.6, we plot these modified metallicity/redistribution contours from Arcangeli et al. (2018). Here we see that the uncertainty on T_{eq} dominates over the retrieved errors, and needs to be included when retrieving the redistribution from the dayside alone.

3.5.5 Comparison of two Ultra hot Jupiters

Spectroscopic phase curves with HST/WFC3 have been published for 3 exoplanets so far, WASP-43b (Stevenson et al., 2014b), WASP-103b (Kreidberg et al., 2018), and WASP-18 (this work). Of these planets, WASP-18b and WASP-103b both belong to the class of Ultra

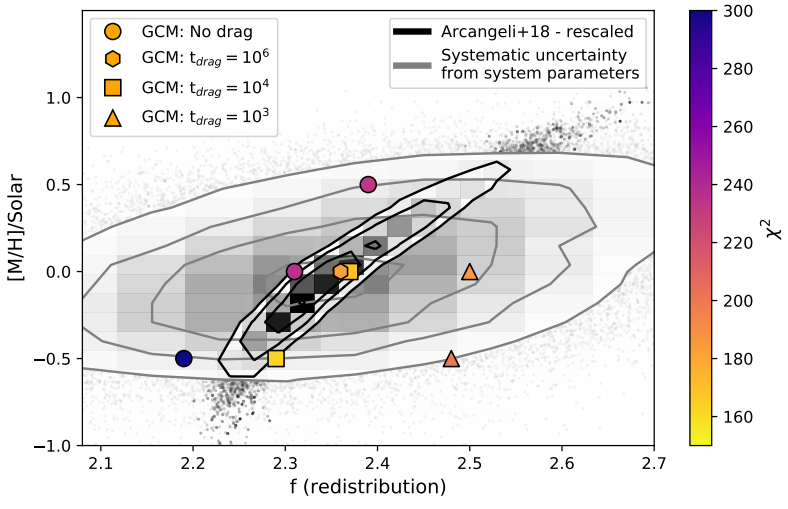

Figure 3.6: Metallicity as a function of redistribution efficiency, comparing 1D modelling to our 3D GCMs. GCM outputs are shown by coloured markers, where marker styles indicate the drag strength in each model: from right to left t_{drag}=10^3s (triangles), 10^4s (squares), 10^6s (hexagon), and no-drag (circles). Markers are also coloured by χ^2 between the corresponding GCM phase curve and our HST/WFC3 phase curve. Retrieved redistribution efficiencies from Arcangeli et al. (2018) are shown by black contours, while in grey are the same contours including a systematic uncertainty on the equilibrium temperature of 44 K.

hot Jupiters, while WASP-43b is in a cooler regime (T_{eq} = 1370 K). The inferred properties, spectra, and phase curves of these two UHJs have many similarities (see Table 3.3). However, key differences between these planets remain, namely their masses, their radius anomalies, and their measured brightness offsets.

The differences between these two planets can shed further light on their atmospheric properties. A first major difference is in their observed circulations: WASP-18b has a small but significant phase-curve offset whereas the phase curve of WASP-103b appears longitudinally symmetric. In the simple picture of circulation as a balance of the radiative and advective timescales (Showman & Guillot, 2002), we would expect the day-night contrast of WASP-18b to be lower than WASP-103b, as the brightness offset should correspond to moderately efficient wind-driven circulation. However the observed day-night contrast of WASP-18b is larger than WASP-103b, in conflict with this simple picture. As suggested in Section 3.5.1, the observed offset of WASP-18b may be the result of a magnetic field, and an offset may not be present on WASP-103b if the planet were to host a weaker magnetic field, as might be expected from its lower mass (Yadav & Thorngren, 2017).

The second major difference is that WASP-103b is very inflated, while WASP-18b is consistent with a non-inflated model (see Section 3.5.2.2). The radius of WASP-103b should be about 1.10 R_{Jup} when no inflation mechanism is present (Thorngren & Fortney, 2018). From the results of Miller et al. (2009), an additional constant heat source of 10^{29} erg s^{-1} could

System Parameters

System	WASP-18	WASP-103
Planet Mass M_J	10.43±0.54	1.49±0.09
Planet Radius R_J	1.17±0.07	1.55±0.05
Planet T_{eq}	2413±44 K	2508±73 K
Orbital Period	22.6 h	22.2 h
Stellar T_{eff}	6400±100 K	6110±160 K
Inferred Properties		
Day-night contrast	$>$ 0.96	0.93
Brightness offset	$-4.5^{\circ} \pm 0.5$	-0.3°±0.1
Planet Metallicity	-0.01 ± 0.35	1.36 ± 0.36
Dayside Photosphere	0.33 bar	0.01 bar
Radius Anomaly	0%	41%

Table 3.3: Comparison of measured and inferred properties of the WASP-18 and WASP-103 Ultra hot Jupiter systems. System parameters are taken from Hellier et al. (2009); Southworth et al. (2009); and Southworth et al. (2015). Values in bold are from this work. Other inferred properties are taken from Arcangeli et al. (2018); Kreidberg et al. (2018). Photospheric pressures here are the median contributing pressures of the dayside spectra over the HST/WFC3 G141 bandpass. The radius anomaly shown is the difference in radius between the measured value and the non-inflated model as a percentage of the measured radius taken from Thorngren & Fortney (2018).

explain the inflated radius of WASP-103b. For this same additional heating, an inflated WASP-18b would have a radius of 1.3R_{Jup} (Miller et al., 2009). This is marginally larger than the observed radius of WASP-18b by 2σ. Thus WASP-18b appears slightly less inflated than WASP-103b despite being around an almost identical star and at the same dayside temperature. One inflation mechanism that can explain this difference is Ohmic dissipation as, for a fixed additional heating, it is less efficient and inflating the radii of a higher mass planet (Huang & Cumming, 2012).

These two differences both highlight that there is a greater complexity behind the observed properties, such as the phase curve properties, in particular in the role that magnetic fields might play on the circulation or radius inflation. Importantly, we can use planets such as the UHJs as a test for inflation theories, as they occupy a parameter space where inflation models differ (Sestovic et al., 2018; Thorngren & Fortney, 2018)

3.6 Conclusions

We observed one full orbit phase curve of the ultra hot Jupiter WASP-18b. We find the peak signal from the dayside at an effective temperature of 2894±30 K and do not detect the nightside of the planet, placing an upper limit of 1430K at 3σ. We find a large day-night-

contrast of >0.96 in luminosity and a small offset of the brightest point from the substellar point by 4.5 ± 0.5 degrees.

We compare the extracted spectroscopic phase curve with Global Circulation modelling and find that the data can be best reproduced by models with efficient drag. Models without additional drag sources fail to reproduce the day-night contrast seen in our data, hence we require an additional drag source to explain the observed day-night contrast. We also find that the behaviour of the phase curve of WASP-18b with metallicity is different from cooler planets, owing to the high temperature chemistry of TiO and water in the atmosphere of WASP-18b. In addition to this, we show that a metallicity enhancement or depletion in our models is not sufficient to match the observed day-night contrast without the presence of efficient drag.

We explore the origin of this efficient drag, and show that it could be due to Lorentz forces on ionized metals in the atmosphere from a magnetic field as weak as 10 Gauss. The effect of a magnetic field on the circulation may also explain the small brightness offset seen in our data, however our models do not explore the full dependence of the circulation on magnetic effects, which will require further studies.

Furthermore, we compare our results to the recently published phase curve of WASP-103b (Kreidberg et al., 2018). We find that the two planets are consistent with the expectation that more massive planets should be less inflated, and support the theory of Ohmic dissipation as an inflation mechanism. However, their different circulations point to a more complicated picture and suggest that other fundamental properties of these systems, such as their magnetic fields, may be different.

We thank N. Cowan for their thorough referee report that greatly improved the clarity of this work. We also thank D. Thorngren for providing tables of predicted planet radii used in this work, and C. Helling for many fruitful discussions. J.M.D. acknowledges that the research leading to these results has received funding from the European Research Council (ERC) under the European Union's Horizon 2020 research and innovation programme (grant agreement no. 679633; Exo-Atmos). J.M.D acknowledges support by the Amsterdam Academic Alliance (AAA) Program. Support for program GO-13467 was provided to the US-based researchers by NASA through a grant from the Space Telescope Science Institute, which is operated by the Association of Universities for Research in Astronomy, Inc., under NASA contract NAS 5-26555. J.L.B. acknowledges support from the David and Lucile Packard Foundation.

3.7 Appendix

Fit parameter	Best fit value	Error
c_1	5.004e-04	5.060e-06
c_2	-1.041e-02	5.553e-03
c_3	7.539e-05	2.856e-05
c_4	-7.993e-03	7.545e-03
fp	9.701e-04	1.133e-05
E_C	1.847e-04	2.935e-05
$C_{scan,f}$	6.791e+08	2.280e+04
$C_{scan,r}$	6.783e+08	2.248e+04
V_1	-2.252e-03	4.915e-05
V_2	1.467e-03	4.034e-05
τ	8.402e-03	1.510e-04
Δt	4.171e-03	5.049e-03
$R_{orb,1}$	1.943e-03	3.004e-05
$R_{orb,2}$	1.038e-03	2.658e-05
$R_{orb,3}$	1.275e-03	9.025e-06
$R_{orb,4}$	1.695e-03	2.651e-05

Table 3.4: Best fit values resulting from the white-light curve fit. Variables are defined below Equation 3.1. Flat priors were placed on all the parameters within acceptable physical ranges. An additional prior was used, ensuring that the minimum of the phase curve (calculated with c_{1-4} and fp) was non-negative.

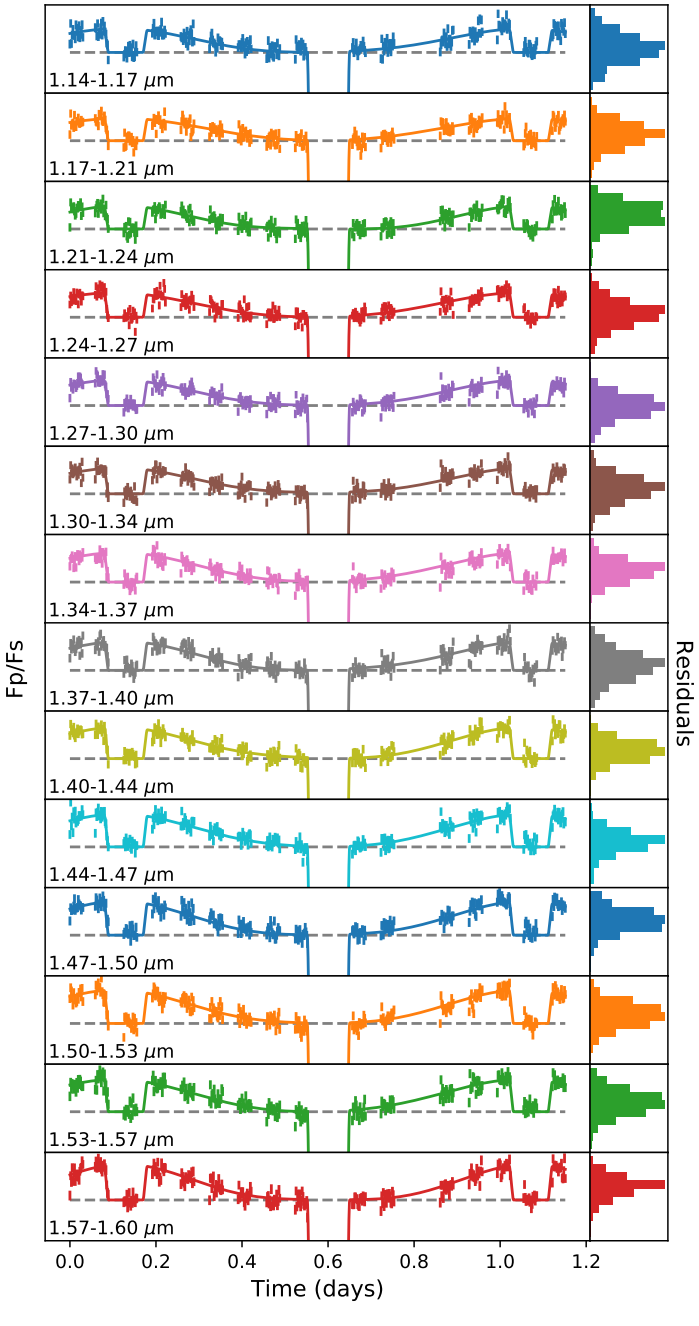

Figure 3.7: Extracted spectroscopic phase curves shown with histograms of residuals. Solid curves indicate fits to the data.

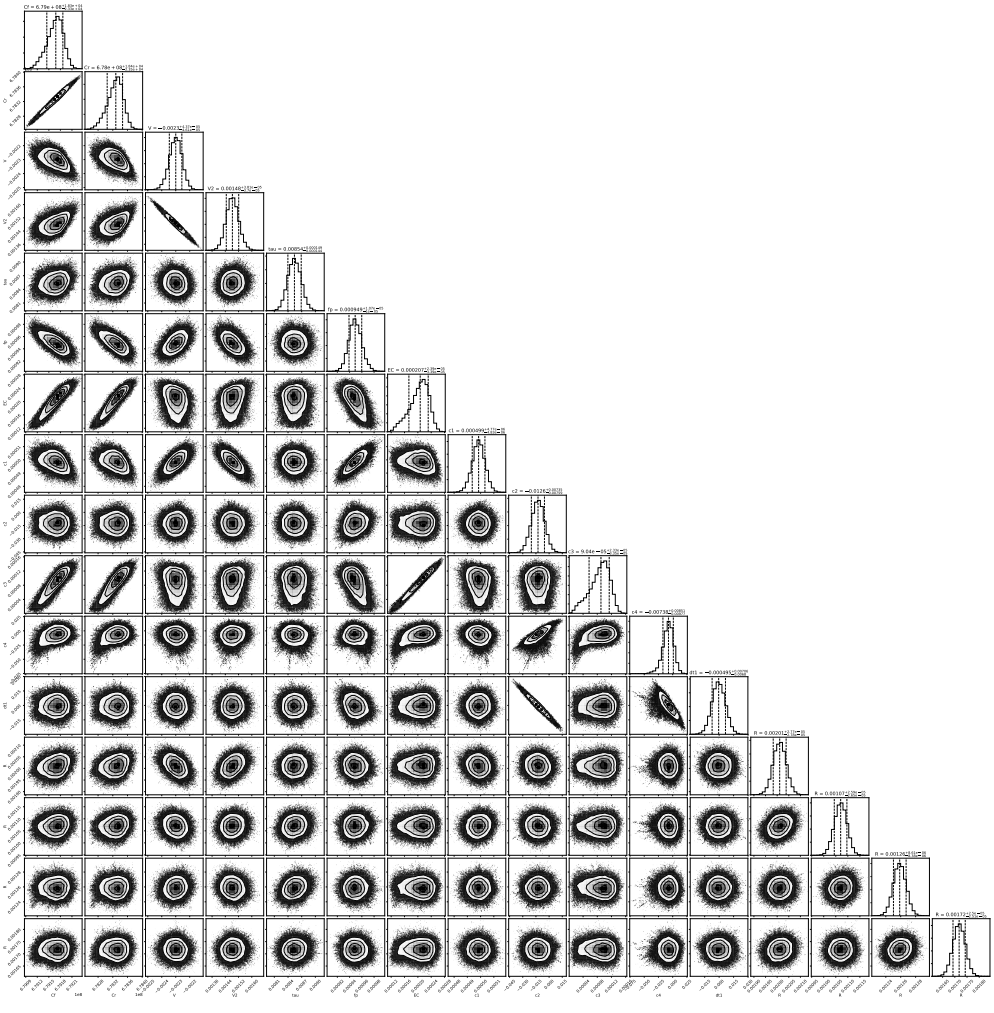

Figure 3.8: Corner plot of posteriors for the white-light curve fit. Result of 10000 steps per 50 walkers. Generated using corner.py (Foreman-Mackey, 2016). Histogram titles show means and $\pm 1\sigma$ confidence intervals of the samples.

Chapter 4

A new approach to spectroscopic phase curves: The emission spectrum of WASP-12b observed in quadrature with HST/WFC3

Jacob Arcangeli, Jean-Michel Désert, Vivien Parmentier, Shang-Min Tsai, Kevin B. Stevenson

submitted to A&A

Abstract

We analyze emission spectra of WASP-12b from a partial phase curve observed over three epochs with the Hubble Space Telescope, covering eclipse, quadrature, and transit respectively. Since the 1.1 day period phase curve was only partially covered over three epochs, traditional fits to the planet flux and instrument systematics cannot recover the thermal emission away from the secondary eclipse. To analyse this partial phase curve, we introduce a new method, based on a common-mode corrections. We are able to recover for the first time the emission spectrum of the planet WASP-12b at quadrature up to an additive constant. The dayside emission spectrum is extracted in a similar manner, and both emission from the dayside and from quadrature are used to constrain the energy budget of the planet.

We present our technique for analysing partial or full phase curves from HST/WFC3 using common mode methods. Our new method removes the achromatic instrument and stellar variability, and uses the measured stellar spectrum in eclipse to then retrieve a relative planetary spectrum in wavelength at each phase. Importantly, and unlike previous phase curve analyses, this technique does not assume a functional form for the planet's emission with phase and does not require a full orbit phase curve. We find that should positional drift between visits be well controlled, this technique allows for the possibility of partial phase

curves. This technique becomes powerful to study new regimes in exoplanetary systems such as for longer period planets. While full phase curves still remain the best technique for studying thermal emission at different longitudes, this technique offers an independent compliment to traditional phase-curve fits.

Our new technique will be ideally suited for observations with JWST, as the telescope will have even better pointing precision than HST. This technique will allow for further 3D studies of atmospheres beyond the few phase curves that will be taken with JWST of only the shortest period planets.

4.1 Introduction

Measuring the thermal emission of planets provides key insights into the nature of their atmospheres, from their temperature structures to their compositions. The daysides of close-in transiting planets are the perfect examples of this, both because of the large signals emitted from their hot daysides, but also technically because an eclipse establishes a baseline from which to measure a planet's emission (Charbonneau et al., 2005; Deming et al., 2006). The natural extensions to dayside emission measurements are phase curves, where again the in-eclipse flux acts as a baseline from which to measure thermal emission throughout the planet's whole orbit, thus probing the longitudinal temperature structure and chemistry (Knutson et al., 2007; Borucki et al., 2009; Snellen et al., 2009). The Hubble Space Telescope Wide Field Camera 3 (HST/WFC3) has allowed the expansion from photometric phase curves to spectroscopic phase curves in order the measure the phase-resolved spectra of hot planets on short periods (Stevenson et al., 2014c; Kreidberg et al., 2018; Arcangeli et al., 2019).

Phase curve observations are time consuming since they rely on monitoring continuously the reflected or emitted light from an exoplanet during its full orbit about its host star. Due to their expensive nature and some technical limitations, phase curves have been limited to planets on short ($\sim$1 day) periods. In principle measurements of exoplanet spectra at various longitudinal phases without obtaining a complete phase curve, so called partial phase curves, are interesting for many scientific purposes. For example, partial phase curves are a unique opportunity to study the circulation on longer period planets, or simply can be used to reduce the time required to observe planet's on short periods. However, using current techniques at low spectral resolution, reflected or emitted light can only be measured when a baseline eclipse is present in each visit. Specifically, measurements away from the dayside, such as at quadrature or of the nightside, are inaccessible outside of full phase curves. Therefore a new approach to systematics removal is required to observe partial phase curves and longer period planets in the future.

A common problem to phase curve observations is that instrument systematics can operate on the same timescale as the full orbit of a close in planet, typically one to two days in period (Stevenson et al., 2014c). For HST, while short term systematics are well fit by charge trap models (Zhou et al., 2017), the long term systematics are thought to originate from changes in the thermal properties and optical path of the telescope, and are not well pre-

dicted. In fact different models of the long term systematics and thermal emission can lead to differences in the inferred atmospheric properties (Kreidberg et al., 2018; Arcangeli et al., 2019). Traditionally these systematic corrections are handled by using continuous monitoring of the planet as it orbit it's parent star, from eclipse to eclipse. This is done assuming the planet is tidally locked and that we therefore return to the same planet's hemisphere when observing consecutive eclipses. Recent work has highlighted methods for dealing with these systematics, such as by observing multiple phase curves over different epochs to help characterize the systematics (Stevenson et al., 2014c; Kreidberg et al., 2018) or by extending the phase curve to re-establish a baseline eclipse (Arcangeli et al., 2019). However both these approaches require additional observing time, and limit the targets for which this technique can be applied to very short orbital periods.

We present here a new approach to phase curve extraction, relying on common-mode methods, that allows us to extract the emission from WASP-12b at different phases, including quadrature. Our new method removes the achromatic instrument and stellar variability, and uses the measured stellar spectrum in eclipse to then retrieve a relative planetary spectrum in wavelength at each phase. We apply our new method to the perfect test case for these issues: the partial phase curve of WASP-12b observed with HST/WFC3 at three different epochs over five days in 2011. Of these data, the dayside emission spectrum and the transmission spectrum have been published (Swain et al., 2013), but the emission at quadrature remains inaccessible to current methods.

Interestingly, WASP-12b is part of an emerging class of exoplanets referred to as the Ultra hot Jupiters (UHJ), distinguished by their extremely hot dayside temperatures resulting in dissociation and ionization dominated chemistry (Bell et al., 2017; Arcangeli et al., 2018; Kitzmann et al., 2018; Kreidberg et al., 2018; Mansfield et al., 2018; Parmentier et al., 2018; Mikal-Evans et al., 2019; Baxter et al., 2020). This makes the emission different planetary phases extremely valuable, as it can be used to constrain the climate and atmospheric dynamics of the planet, as well as probe the planet's chemistry beyond the muted features in the dayside spectrum.

We outline the data and our method in Section 4.2 and explore the accuracy of the technique. Our results for WASP-12b are described in Section 4.3, along with a comparison to 3D forward models. We discuss the implications of our results and possible future applications in Section 4.4, and conclude in Section 4.5.

4.2 Data and Methods

4.2.1 HST Data

Our data set is the partial phase curve of WASP-12b, from April 2012 (Program 12230, PI M.R. Swain, Swain et al. 2013). These data consist of 3 visits: 5 orbits taken around transit, 5 orbits taken around secondary eclipse, and 2 orbits taken in quadrature (between transit and secondary eclipse). The raw data are shown in Figure 4.1 and described in Table 4.1. Together these visits constitute coverage of just over half of the phase curve of WASP-12b,

with each visit taken within the same 5 day period. The transmission spectrum and eclipse were published in Swain et al. (2013), Mandell et al. (2013), and Stevenson et al. (2014b,a) while the visit taken in quadrature is unpublished. Each of the visits were taken in staring mode with the same instrument setup, including a fixed orientation of the telescope.

Start time	Observation	Planet phase
2011-04-11 07:15	Quadrature	0.18 to 0.27
2011-04-12 00:48	Transit	-0.15 to 0.12
2011-04-15 19:50	Eclipse	0.32 to 0.60

Table 4.1: Table of observed visits and corresponding planet phases.

4.2.2 Method

In order to extract the planet signal we use a two step correction. First we use a common-mode correction to remove instrument systematics, and second we compare the extracted spectra at each orbit to the stellar spectrum measured in eclipse to measure the planet spectra. For the first step we divide each spectroscopic light curve by the white-light curve (integrated over the full wavelength range), removing any common-mode systematics. In the second step we divide the spectra of each orbit by a reference spectrum of the star, taken during secondary eclipse and processed in the same way. This produces a relative spectrum of the planet at each phase up to an additive constant. We refer to these spectra as relative spectra, relative here referring to them being relative in wavelength, as their absolute flux levels are removed by the common-mode correction. Spectra are not extracted for the first orbit of each visit, as they are seen to exhibit stronger systematics than subsequent orbits.

Below we illustrate the applied method. The raw data $L_{\lambda,t}$ and w_t, the spectroscopic light curves and white light curve respectively, can be expressed by the formulae below.

$$\begin{aligned} L_{\lambda,t} &= S_{\lambda,t} * [F_{\lambda,t}^{star} + F_{\lambda,t}^{planet}] \\ w_t &= s_t * [f_t^{star} + f_t^{planet}] \end{aligned} \tag{4.1}$$

Here, $S_{\lambda,t}$ and s_t are the unknown systematic effects and the $F_{\lambda,t}$ and f_t are the spectra and white-light flux output respectively, of either the star or the planet. We assume that the star remains constant in time over the visit, with the exception of the in-transit data which we exclude, e.g. $f_t^{star} = f^{star}$ and $F_{\lambda,t}^{star} = F_{\lambda}^{star}$.

One can therefore use the white-light curve to divide out the unknown time-dependent systematic component. We now assume that $S_{\lambda,t} = s_t * s_\lambda$, effectively the assumption that the systematics in the white light curve are representative of each wavelength bin, often referred to as a common mode. We separately test the validity of this assumption in Section 4.2.5. Dividing Equations 4.1 becomes:

$$L'_{\lambda,t} = L_{\lambda,t}/w_t = s_\lambda * [F^s_\lambda + F^p_{\lambda,t}]/[f^s + f^p_t] \tag{4.2}$$

Where $L'_{\lambda,t}$ are now the common-mode corrected light curves. Evaluating Equation 4.2 at $t = t_{eclipse}$ gives:

$$L'_{\lambda,t=t_{ecl}} = s_\lambda * F^s_\lambda / f^s \tag{4.3}$$

Where F^s_λ is the stellar spectrum, and f^s is the white-light flux in eclipse.

Hence using the in-eclipse data we can measure the spectrum of the star multiplied by the remaining wavelength dependent systematics. Using this we can finally obtain the emission spectrum of the planet. This is done by dividing the spectra from the corrected light-curve ($L'_{\lambda,t}$) at each time by the in-eclipse stellar spectrum.

$$\begin{aligned} L'_{\lambda,t}/L'_{\lambda,ecl} &= [F^s_\lambda + F^p_{\lambda,t}]/F^s_\lambda * f^s/[f^s + f^p_t] \\ &= [1 + F^p_{\lambda,t}/F^s_\lambda] * [1 + f^p_t/f^s]^{-1} \\ &= q(t) + F^p_{\lambda,t}/F^s_\lambda + \mathcal{O}((F^p/F^s)^2) \\ &\sim q(t) + F^p_{\lambda,t}/F^s_\lambda \end{aligned} \tag{4.4}$$

Where $q(t)$ is some time dependent residual that is removed by measuring the spectra at each time relative to the first spectral bin. This last step of ignoring higher order terms only holds for systems where the variability of the star is sufficiently small, which we discuss in Section 4.2.7.

4.2.3 Comparison to classical eclipse spectroscopy

When applied to the secondary eclipse data of WASP-12b, our method is substantially different from the classical method, such as that used in Stevenson et al. (2014b). Since we do not fit for the depth of the eclipse, but rather use the out of eclipse data to measure the spectrum of the planet, our method is more akin to current spectroscopic phase curve extractions (Stevenson et al., 2017; Kreidberg et al., 2018; Arcangeli et al., 2019). There are still key differences between our approach and a typical phase curve extraction, as we do not assume a functional form for the planet's emission with phase, nor for the systematics, nor do we recover the absolute spectrum of the planet at each phase, only the relative spectrum in wavelength. This approach is chosen so as to the spectra at each phase in the same manner, from the dayside spectrum to the nightside and quadrature spectra, as in this case neither a classical eclipse depth measurement nor a phase curve fit can be applied to the whole data set due to the observations being spread over five days. Hence this approach should be considered a complement to the existing extraction of the dayside emission and transmission spectra.

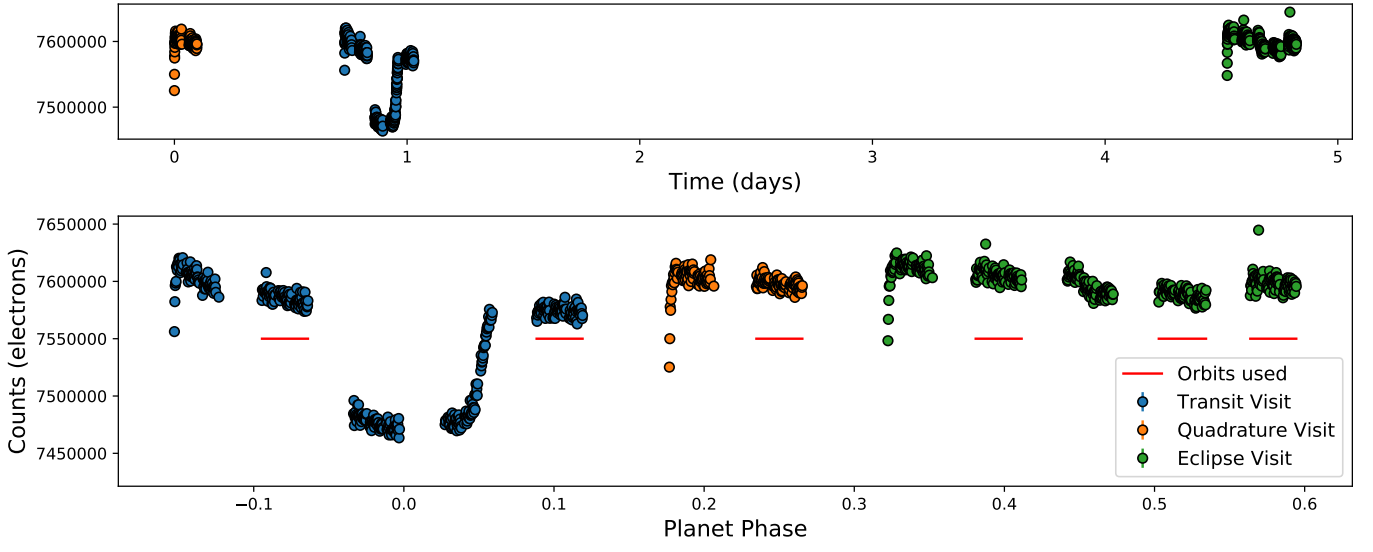

Figure 4.1: Top: Raw phase curve plotted in time. Bottom: Raw phase curve phase folded to the period of the planet. The orbits used in the analysis are marked by a red line.

Our approach has consequences for how we compare to circulation models (such as those present in Section 4.3.2). A typical dayside eclipse depth measurement is normally compared to the magnitude of the phase curve at phase 0.5, as the eclipse depth is an average of the planet's emission across the dayside. In our approach, we extract the relative emission spectra before and after eclipse, and therefore compare to the circulation models at phases just before and just after eclipse. This technique is then also applicable to every other phase of the planet's emission, with the exception of the in-transit data, as each phase can be directly compared to the same phase in the models.

4.2.4 Pointing Offsets

Shifts of the spectra in wavelength can dominate the systematics of light curves observed with HST/WFC3 (Wakeford et al., 2016; Tsiaras et al., 2016, 2019). On top of this, our technique relies on the stellar spectrum remaining constant between visits, which requires that the position of the spectrum on the detector also remains constant, or can be accurately reconstructed from a shifted spectrum. Since the IR WFC3 pixel flat-field is uncertain at the 1% level, and the spectrum observed is under-sampled (see Deming et al. 2013), measuring and interpolating any shifted spectra back to a reference position on the detector is increasingly difficult for larger positional shifts. Typically $<$15 mas drift (0.11 pixels) in the x-position is optimal for exoplanet studies using the spatial scanning mode (Stevenson & Fowler, 2019).

We first assess the possible effect of shifts on our spectra by measuring the position of the dispersed spectrum on the detector for each exposures. We take the flat-field corrected raw images and perform a column-sum to produce a raw spectrum for each exposure. We then produce a reference spectrum from the average of all the raw spectra, and cross-correlate between this and each of the raw exposure spectra to measure their positional shifts on the detector. The measured offsets, in pixels along the x-axis, are shown in Figure 4.2.

For the transit visit, we find that there is a significant offset in x-position relative to the other visits, greater than 0.1 pixels. If uncorrected, this offset produces a slope in the extracted spectra which we estimate to be a few times 0.1% (1000 ppm). In principle the transit spectra could be interpolated back to remove this slope, however in practice the uncertainty on the flat-field and the under-sampling of the spectrum limit the accuracy of this interpolation, leading to an additional 100-500ppm uncertainty on the transit spectrum. We re-interpolate the spectra obtained during the transit visit to the reference in-eclipse exposure, and plot the results in Figure 4.3. Here we see that the emission spectrum close to transit is dominated by large variations between bins above the expected noise level, and is not usable.

We also measure the positional shift of the spectrum on the detector between the quadrature orbit and the in-eclipse orbit to be negligible at 0.0011 pixels precision, seen in Figure 4.2. This translates to an uncertainty of 11 ppm per pixel from the flat-field correction, which is well within the errors on the quadrature spectrum. Hence we can conclude that the positional drift induced systematics should be negligible for the quadrature spectrum.

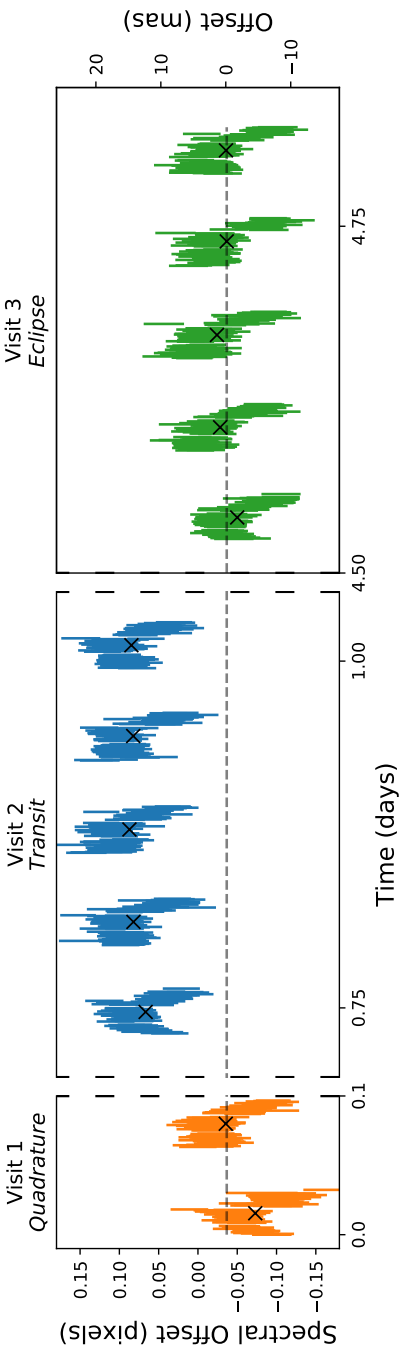

Figure 4.2: Offset of spectrum position in the dispersion direction relative to average over all exposures as described in Section 4.2.4. The x-axis shows the time, in days, since the first exposure with line breaks between different visits. Coloured lines indicate offset for each exposure with 1σ uncertainties. Black crosses are the average offset for each orbit, with the horizontal dashed line set to the quadrature orbit offset for visual reference.

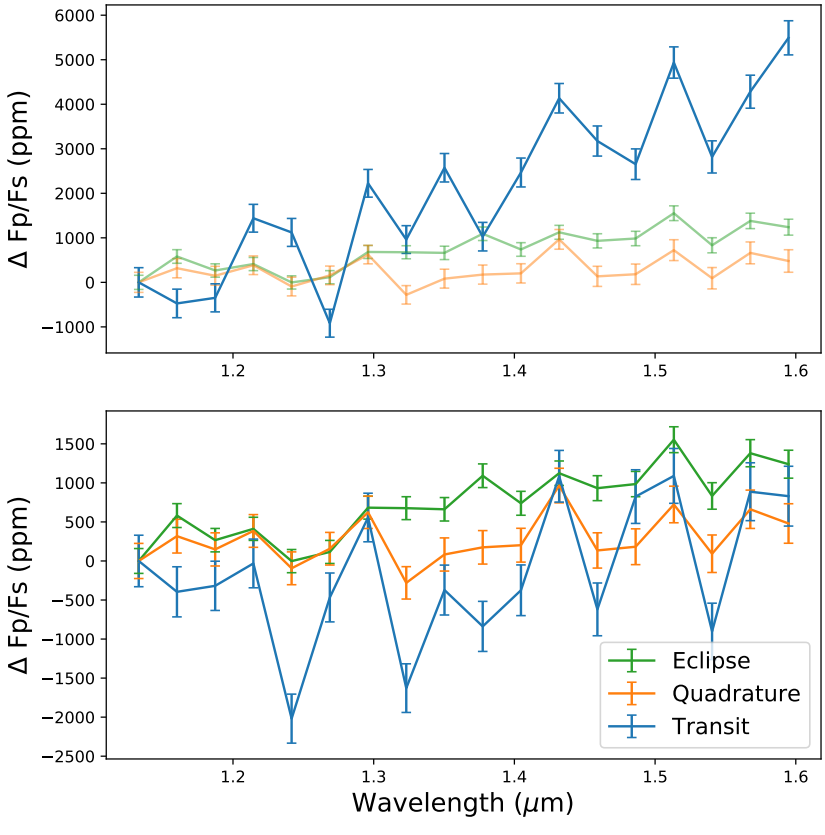

Figure 4.3: Top: Common-mode corrected exoplanet spectra with propagated 1-σ errorbars as described in Section 4.2.2. The transit spectrum extraction in blue is referred to as the nominal extraction. Bottom: The same spectra, except for the nominal transit spectrum which has been re-interpolated by the measured positional shift (computed in Section 4.2.4). The systematic spectral slope is largely removed but residual noise is still clearly present in the spectrum in the form of variation between spectral bins with amplitude larger than the expected errors or planet's signal.

4.2.5 Residual Noise

We estimate the quality of our systematic correction by comparing the systematics-corrected in-eclipse orbit to a flat line at each wavelength. As the star alone is observed during this orbit and should remain constant, the scatter between the exposures within the in-eclipse orbit shows the level to which the systematics correction was successful on a short baseline.

We measure the scatter between the exposures at each wavelength for increasing number of wavelength bins, shown in Figure 4.4. For each wavelength bin, we divide by a reference white-light curve from the sum of the other wavelength bins, and examine the residuals. We then measure the scatter of the residuals at each wavelength, and report the average scatter for each wavelength bin size. We find that the average scatter reaches close to photon noise precision, around 20% above photon noise, for 15 or more wavelength bins during the eclipse. We choose to bin by 6 pixels, corresponding to 18 total wavelength bins over the full spectrum, to maximise the signal to noise of our final spectra, while maintaining the precision better than 20% above photon noise.

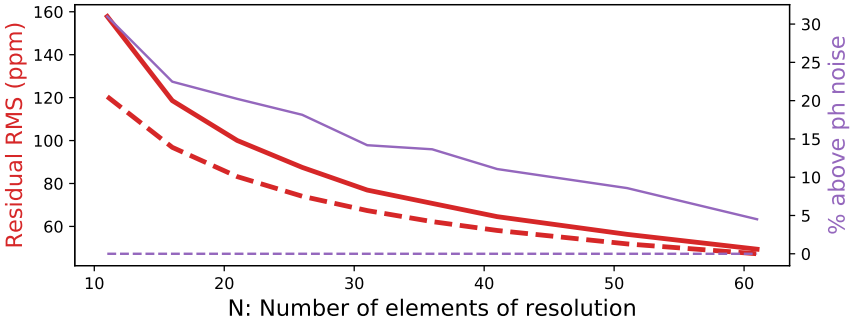

Figure 4.4: Measured scatter of the residuals of the lightcurve taken from the in-eclipse orbit and normalized by the white-light curve for various sizes of wavelength bins (decreasing number of wavelength bins towards the right). The scatter represents the average rms of the residuals from the lightcurve across the wavelength bins for each choice of binning. The left y-axis shows the residual rms, plotted as the thick red lines, while the right y-axis shows the scatter as a percentage of the photon noise limit, plotted as the thin purple lines. Dotted lines show the expected photon noise limit in each case.

4.2.6 Dilution Correction

The WASP-12 system has been found to include a faint companion binary system (WASP-12B/C) to the main star (WASP-12A) (Bergfors et al., 2011, 2013; Crossfield et al., 2012). We correct our extracted planet spectra for the dilution by the companion stars, following the methods outlined in Stevenson et al. (2014b,a). This correction is done by measuring the ratio of the stellar spectra by simulating a range of models, accounting for their offset in position on the WFC3 detector. We then divide their contribution from each of our spectra, which can be found in Table 4.4 and is roughly equivalent to a slope of about 100ppm across the whole wavelength range.

4.2.7 Stellar Variability

We asses the impact of any variability in the spectra of either WASP-12A or its companion stars WASP-12B/C on our final planet spectra. We use an extraction window that contains the flux from WASP-12B+C as well as WASP-12A, as the spectra bleed into each other on the detector (see Figure 4.5), hence the variability of the companions needs to be considered. While any photometric variability in the stars is removed by the common mode correction, changes to the stellar spectra are not and could be left as residuals in our final planet spectra.

We estimate the variability of the WASP-12 system over the course of our observations by comparing the second orbit of each visit. In Figure 4.6, we plot the second orbit of each visit minus the average of the second orbits across all visits. This subtraction removes the orbit-ramp that is constant between orbits. The spread between the visits at this stage is approximately 0.13% (top panel of Figure 4.6), however a large fraction of this variability is expected to be due to the planet's own changing emission. We remove the predicted contribution from the thermal emission of WASP-12b, with the resulting stellar contribution shown in Figure 4.6, based on our nominal circulation model presented in Section 4.3.2. The remaining spread between visits is 0.08%, which is close to the photon noise limit, with the remaining variation consisting of a combination of changes in systematics and stellar variability between visits. Since the planet model is uncertain, we adopt a conservative upper limit of 0.1% on the variability of the WASP-12 stars within our observing window.

We estimate the impact that 0.1% variability in the brightness of the WASP-12 system would have on our planet spectra. Assuming starspot temperatures of 300K cooler than the stellar surface of WASP-12A (Kreidberg, 2015), a 0.1% change in brightness could be achieved by a 0.6% change in spot covering fraction between visits. This would result in a change to the slope of the spectrum of the system of 50-100 ppm. Equivalently, a 1% change in the brightness of the companions WASP-12BC would result in a 0.1% change in the brightness of the system, leading to a similar slope in the extracted spectra of 50-100 ppm between visits. An additional slope of this magnitude or lower would be well within the uncertainties on the estimated blackbody temperatures, within 150-200 K, and would not change the results of this work.

4.3 Results

4.3.1 Extracted Emission Spectra

We apply our new method to extract the longitudinally-resolved spectra from spectroscopic phase curves to the partial phase curve of WASP-12b. We extract the dayside spectrum before and after eclipse, as well as, for the first time, the quadrature spectrum of the planet (see Figure 4.7 and Table 4.3). We find that the emission spectra from the dayside before and after eclipse are consistent, and hence we combine them into one spectrum that we refer to as the eclipse or dayside spectrum, although we note this spectrum is not derived using classical eclipse spectroscopy. We first fit the spectra with black-body curves to estimate their corresponding temperatures from their spectral slopes. The best-fit dayside black-body

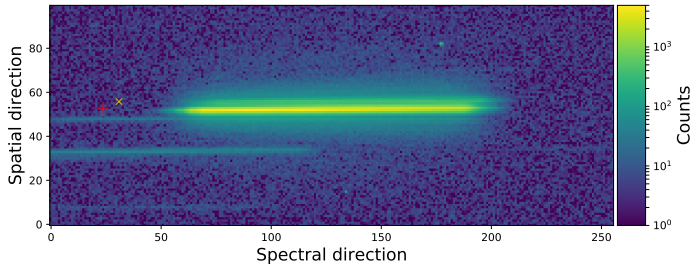

Figure 4.5: Cutout 2D image of a single representative exposure. The bright spectrum in the centre is that of WASP-12A. Directly superimposed on that is the combined spectrum of WASP-12B+C, seen as the faint trace above the main trace. Below these two are spectra of faint background stars. The locations where the non-dispersed direct images would fall are marked as crosses, red for WASP-12A and yellow for WASP-12BC.

is at 3186±410 K at a reduced χ^2_r of 2.73, and the best-fit quadrature black-body is significantly cooler at 2124±314 K with a χ^2_r of 1.77. Our extracted spectra show a decrease in slope between eclipse and quadrature, equivalent to a decrease in brightness temperature of 1062±516 K, and suggestive of weak redistribution.

4.3.2 Comparison to models

We compare our data to global circulation models (GCMs) of the atmosphere of WASP-12b. The atmospheric circulation and thermal structure were simulated using SPARC/MITgcm (Showman et al., 2009), further details on the models can be seen in Parmentier et al. (2018). We produced two self-consistent forward models, one at a solar composition and one with 2x enhanced optical opacities. The 2x enhanced optical opacity model was chosen to explore the effect of larger temperature inversions at low pressures. We also post-process our solar composition model with different opacities and physics removed, to test the effects of H-, dissociation, and molecular opacities on our model spectra.

Since our measured spectra are only known relative to a spectral bin, we choose to normalize the spectra from both the data and models by subtracting the average level, shown in Figure 4.8. We find that there is a relative agreement between the observed quadrature spectrum and each of the models, while the observed eclipse spectrum appears slightly steeper than the models. We discuss the possible source of this difference in Section 4.4.1.

4.3.3 Comparison to dayside emission studies

We can also compare our extracted dayside emission spectrum to previously published work using the same data (Swain et al., 2013; Stevenson et al., 2014a). The three dayside emission spectra are shown in Figure 4.9. We can see that in general there is a good agreement between the spectra, with slight differences due to the choice of binning. This is notable because our approach is very different to the two previous works. In classical secondary eclipse studies, such as Swain et al. (2013); Stevenson et al. (2014a), the dayside emission

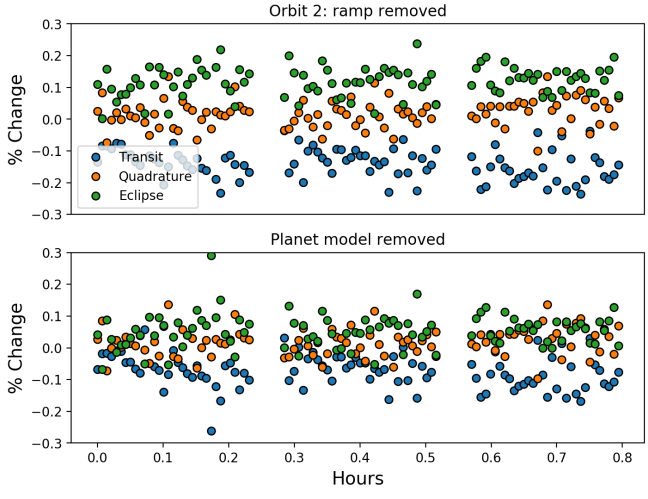

Figure 4.6: Brightness of exposures taken during the second orbit of each visit, coloured by the corresponding visit and measured relative to an average across all three visits, discussed further in Section 4.2.7. The exposures are plotted in hours since the beginning of the orbit. Top: Exposures from the second orbits as a percentage change from the average second orbit across all visits. Bottom: Same exposures with the predicted planetary contribution removed.

is measured from the difference between the out-of-eclipse orbits and the in-eclipse orbits. This is therefore an estimate of the emission from the full dayside at planetary phase 0.5. Our method instead measures the emission spectrum of the planet at phases ∼0.46 and 0.58, relative to a spectral bin. We find these spectra to be consistent, likely due to being dominated by the same hotspot, and therefore combine them into a single relative emission spectrum for the dayside.

We also show the absolute spectra extracted by (Stevenson et al., 2014a) compared to our circulation models in absolute (Figure 4.10). Here we can see that none of the models are able to match both the slope and the absolute brightness of the spectrum.

4.4 Discussion

4.4.1 Emission spectra of WASP-12b compared to circulation models

We compare our data to a range of circulation models. Broadly our data matches well the model prediction of decreasing temperature from eclipse to quadrature, due to the minimal day-night redistribution of flux. Our extracted quadrature spectrum provides a constraint on the temperature through the measured blackbody temperature of 2124±314 K, but is not precise enough to distinguish between our generated models.

Our relative dayside spectrum has the slope of a blackbody spectrum at 3186±410K, in agreement with the absolute emission spectrum obtained by Stevenson et al. (2014a). The comparison of both extractions of the dayside spectrum to our nominal circulation model re-

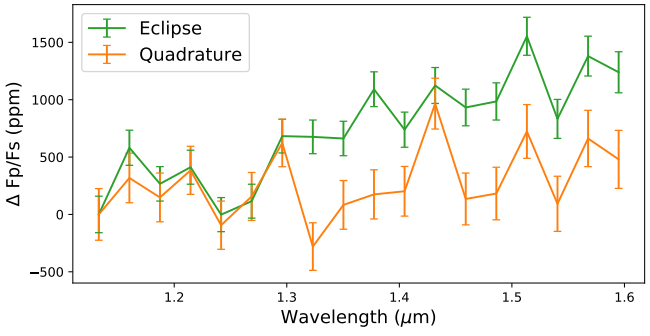

Figure 4.7: Extracted emission spectra from quadrature and eclipse for WASP-12b, normalized to the first spectral bin.

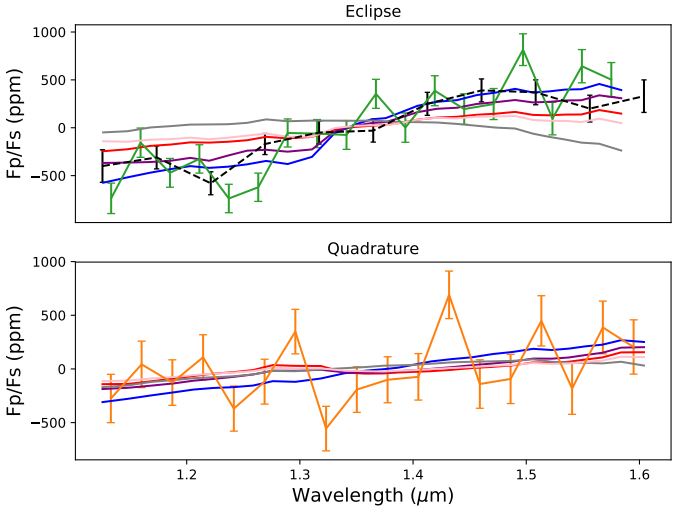

Figure 4.8: Comparison of extracted exoplanet spectra to GCM results. All measured spectra and models are normalized by the average of the spectrum across the bandpass in order to allow a comparison to our relative spectra. Top: The data are shown for the eclipse (in green) as well as the dayside spectrum extracted by Stevenson et al. (2014, in black). Bottom: the extracted quadrature spectrum (in orange). For both panels the models are shown for solar composition (red), no-dissociation (blue), no H- (purple), no molecular opacity (grey), and 2x optical opacity (pink).

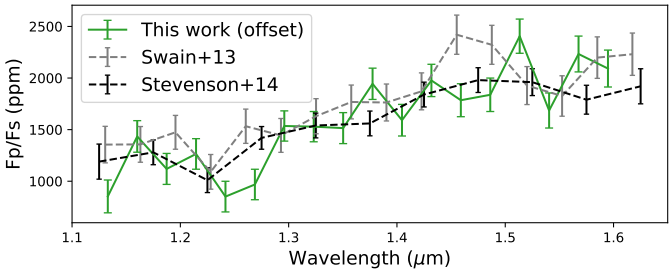

Figure 4.9: Comparison of our dayside emission spectrum to previous works, all extracted from the same data with different pipelines and techniques (see Section 4.2.2; Stevenson et al. 2014a; Swain et al. 2013). Our extracted relative spectrum has been offset to match the absolute level of Stevenson et al. (2014a). All of the works are within good agreement, with additional slight differences arising due to the choice of binning.

veals a steeper spectrum than the models (Figure 4.9, 4.10). This slope seen in the data may be indicative of additional physics present in the climate of the planet that are not accounted for in our models, such as non-equilibrium chemistry. We briefly explore two possible physical effects that could be responsible for this increased slope, an increased temperature and non-equilibrium water abundances.

One explanation for the steeper slope seen in the dayside spectrum could be a genuinely hotter dayside temperature, caused for instance by a steeper temperature/pressure profile than predicted by our models. Each of our models exhibits a temperature inversion due to a combination of optical absorbers and reduced cooling by thermal dissociation (Lothringer et al., 2018; Parmentier et al., 2018) although a temperature inversion on WASP-12b has not been strongly detected (Kreidberg, 2015). Hence a steeper T/P profile could originate from an increase in optical opacity at low pressures, either due to a metallicity enhancement or non-equilibrium abundances. We produced an additional circulation model with a 2x enhancement of optical opacities, mimicking an enhancement of metal compounds in the upper atmosphere (e.g. TiO), and forcing the temperature pressure profile to be more strongly inverted. We see however that the increased temperature at low pressures causes a net loss in flux from the emission spectrum at wavelengths redder than 1.4μm (see the pink curve in Figure 4.10). This is due to the increased dissociation of water at higher temperatures. This dissociation causes the observed water emission to be observed from deeper layers, below the inversion, where the atmosphere is cooler. Hence it is not likely that an increase in the local temperature could cause the observed increased steepness of the emission spectrum, as the chemical response by dissociation to that increased temperature acts to reduce the slope of the spectrum.

Another explanation could be non-equilibrium processes. Our models compute the dissociation fraction of water assuming equilibrium chemistry. However the transport of cool gas from the nightside of the planet to the hot dayside could increase the contribution of water to our spectra if the dissociation of water is slower than its advection. We estimate timescales for the thermal dissociation of water (since photo-dissociation is not expected

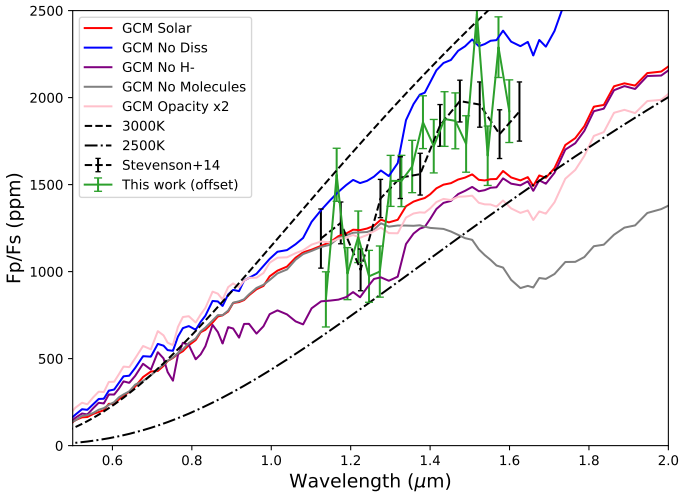

Figure 4.10: Emission spectrum of WASP-12b as measured by HST/WFC3 (absolute measurement) compared to global circulation models and blackbody emission curves. The Solar (red) and 2x Optical Opacity (pink) models are self-consistent forward models. The remaining models include post-processing changes to the solar model. No dissociation (blue) has no dissociation of molecules, No H- (purple) has no H- opacities, No molecules (grey) has no molecular opacities resulting in an H- continuum spectrum.

at 0.1 bar levels) using the methods of Tsai et al. (2018). To first order the dissociation and recombination timescales are equal as they are evaluated at equilibrium. We find that the rate-limiting reaction for water dissociation in this case is the thermal dissociation of H_2 to produce H atoms. This reaction produces H atoms, which allows water to dissociate through the very fast reaction of H + H_2O -> OH + H_2. Hence the timescale for the thermal dissociation of hydrogen is the same as the timescale for the dissociation of water at these temperatures.

We compare our estimated dissociation timescale to the advective timescale in our models. In this context the advective timescale is the ratio of the planet's radius to the magnitude of the UV components of the wind speed, as the vertical wind speeds are small. Figure 4.11 shows contours of the logarithm of the ratio between the advective (wind) timescale and our calculated Hydrogen dissociation timescales, plotted here over the background temperature map, at three different pressures. In this figure, it can be seen that the dayside advective timescale is always >100x slower than the dissociation timescale, and typically between $10^3 - 10^6$x slower. Regions of the map with timescale ratios close to zero or negative can only be seen in the cooler regions of the atmosphere, where dissociation will not take place. Therefore any parcel of dissociated gas that could be carried to these regions to remain out of equilibrium would cross many contours, resulting in all of the dissociated gas recombining. Hence we conclude that it is likely water and H_2 reach their equilibrium dissociation fractions in the atmospheres of UHJs despite the winds of a few km/s. Globally the dayside advective timescale is much longer than typical thermal dissociation timscales, suggesting

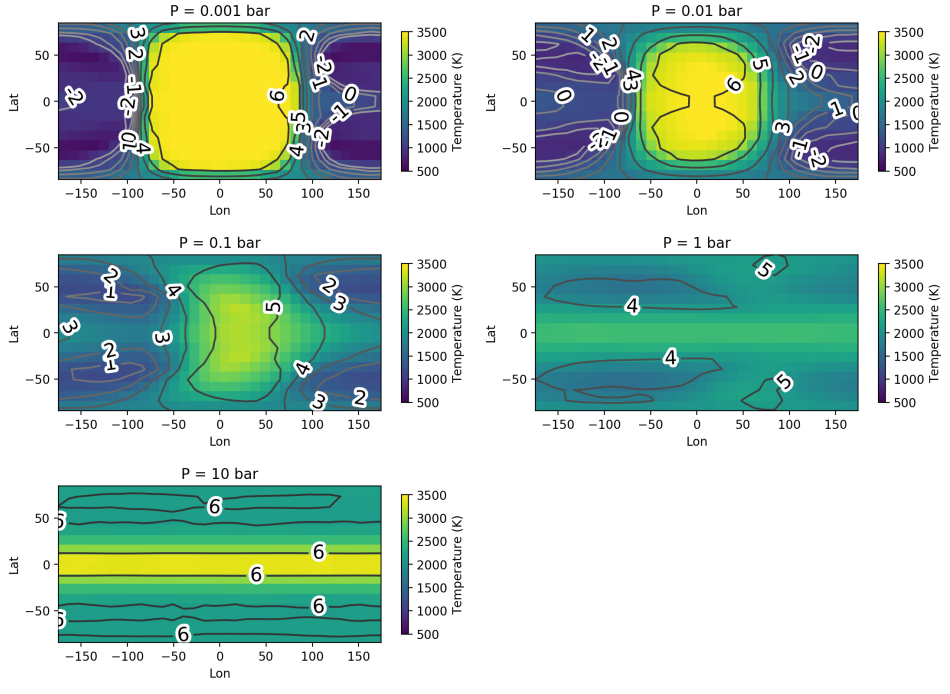

Figure 4.11: Brightness temperature maps in 2D as produced by our GCM using solar abundances at five different pressures. Contours show the ratio of the simulated advective timescale over the predicted dissociation timescale for H_2, on a log scale.

that the dayside is in equilibrium with respect to other thermally dissociated molecules as well, however this remains to be calculated for each species.

4.4.2 Comparison to Spitzer phase-curves of WASP-12b

Previous studies of the phase curve of WASP-12b have revealed a complicated system, as data have shown that the planet deviates from simple model predictions. Results from Spitzer photometry show a sinusoidal phase curve typical of an UHJ in the first bandpass around 3.6μm with a hot dayside and cool nightside, but two additional peaks at quadrature in the second bandpass at 4.5μm were found (Cowan et al., 2012; Bell et al., 2019). We compare the brightness temperatures of the planet's emission in Spitzer to our measured blackbody temperatures derived from WFC3 data. We use the fit results from Bell et al. (2019) to determine the equivalent brightness at each HST orbit from both Spitzer bandpasses, and convert this to a brightness temperature for the planet (Table 4.2). This allows for a quantitative comparison of our work with previous studies. Differences between the results are expected due to the changes in opacities between the HST wavelength range and those measured by Spitzer,

that lead to different pressure levels and species probed by the observations. We present this comparison below.

The phase curves from Spitzer at 3.6 and 4.5 μm have been seen as evidence of gas stripped from the planet, that emits in the infra-red and is responsible for the double peaked feature in the 4.5μm phase curve Cowan et al. (2012); Bell et al. (2019). This gas would need to be either sufficiently cool or CO rich such that it were visible in the 4.5μm phase curve, but not at 3.6μm. Hence the natural prediction is that the double-peaked nature of the 4.5μm phase curve should not be seen in the HST/G141 bandpass, as at these wavelengths CO is not a dominant opacity, and any gas sufficiently cool to not be seen at 3.6 μm should also not affect the spectrum around 1.4 μm. Our results are consistent with this hypothesis, as we measure a significant decrease in temperature going from the dayside to quadrature, in contrast to the double-peaked behaviour at 4.5μm.

While theoretically there is a CO line at 1.6μm, it is about 1000x weaker than that at 4.5μm, resulting in only a few ppm deviation in the phase curve when extrapolating the Spitzer 4.5μm result. Hence we are not able to determine whether there is any additional CO emission from our spectra.

The 3.6μm phase curve exhibits different behaviour than the 4.5μm phase curve. At 3.6μm, the planet's emission is dominated by water, similar to the predictions for the HST/WFC3 G141 bandpass. Hence we expect the behaviour and amplitude of the phase curve at 3.6μm to be similar to phase curves taken with HST WFC3/G141. The 3.6μm phase offset measured in Spitzer is seen to vary, but our HST results are more consistent with the observations from 2013 where only a small offset was seen. However, the planetary phases at which we measure temperatures in this work do not cover enough of the phase curve to measure a hot-spot offset, but remain consistent with small-to-no westward offset.

Instrument	before	Dayside T_p mean	after	Quadrature T_p K	Observation Year
HST G141 (this work)	3108±520	3186±410	3270±557	2124±314	2011
Spitzer Ch1	2720±49	2522±44	2319±74	2340±75	2010
(3.6μm)	2400±70	2576±43	2746±51	2032±87	2013
Spitzer Ch2	2759±59	2721±49	2684±80	2904±84	2010
(4.5μm)	2689±71	2612±47	2534±62	3024±91	2013

Table 4.2: Measured blackbody temperatures from HST compared to brightness temperatures in Spitzer, binned to the same phases, derived from Bell et al. (2019).

4.4.3 Pointing Stability between visits

We explore further whether the pointing drift between visits can be explained and how this could be mitigated in future observations.

Our measured pointing offsets (shown in Figure 4.2) are within the nominal expectation for HST's target acquisition precision and fine guidance sensor (FGS) operation. The target acquisition was performed under the default mode for each visit, with a re-acquisition occurring after each earth occultation. This has an expected jitter of $\sim$7mas (0.05 pix) as well as a $\sim$50mas drift over 12h or more (approximately 0.5 pixels) which is attributed to changes in the thermal properties of the FGS (from HST).

Hence, the measured drift within each orbit, as well as the offset between the first visit (quadrature) and the second visit (transit), are within the limits of nominal HST performance. Notably, the third visit (eclipse) is almost perfectly aligned in position with the first visit (quadrature). We first verified with STScI that no additional manoeuvres were performed and that FGS acquisition was executed as normal. We also measured that the reference star HD258439 that was observed with two orbits at the end of each visit, exhibited the same movement on the detector as WASP-12 between visits, demonstrating that the FGS acquisition was not at fault. Hence, we conclude that some change in the instrument, such as in the optical path through the location of the detector in the focal plane, occurred during the second visit alone, and is responsible for the observed shift of the spectrum. We confirmed with STScI that such behaviour is within the expected performance of the telescope. This also implies that the very close alignment between the first and third visit was by chance better than the nominal pointing precision of HST.

It is not clear from our observations how likely visits observed within a short time-span are to be well aligned on the detector. However it may be possible in the future to ensure that the position of the spectrum on the detector is well aligned with a previous visit, e.g. through routines such as a "real time interaction" target acquisition, that are not recommended due to the additional requirements on scheduling and man-hours (HST, 2020).

4.4.4 Partial phase curves in the future with HST, JWST, and other spectroscopic space facilities

Full phase curves remain the best avenue for obtaining longitudinally resolved absolute emission spectra of exoplanets, in particular phase curves anchored by an eclipse at the start and end of the visit to allow for evaluation of any residual systematics or drift. Currently full phases curve are only possible for $\sim$1 day period planets with HST, and $<$2 day periods with JWST, so an alternative is needed, particularly for longer periods. Partial phase curves are a cheap alternative that may allow for some of the same science to be accomplished, in particular when looking for changes in spectral features with longitude.

Archival data of transits and eclipses will only be accessible with this technique should the chance alignment of the dispersed spectra on the detector be better than 0.1 pixels, assuming the visits were already taken with identical observing modes. Performance may be different

for spatially scanned data, as there can be additional drift of the telescope within an exposure, depending on the adopted scan rate of the telescope. It has been shown that typical performance of the spatial scanning mode results in drifts below ∼15mas (∼0.11 pixels) for 77% of data taken in this mode (Stevenson & Fowler, 2019). Further study would be needed to verify that performance at this level, or with a lower pointing precision, would be sufficient to analyze spatially scanned data with this technique. It is however likely that at least 10% of observations will not have a sufficient pointing stability for our method, as these observations are deemed to have failed, with a pointing drift of >1 pixel (Stevenson & Fowler, 2019).

Both JWST and the ARIEL mission are scheduled to observe phase curves of exoplanets in the near future. As JWST observations are expected to operate at an increased pointing precision relative to HST, of better than 17mas scatter per axis (JWST User Documentation), this technique should be applicable to JWST data. JWST will be in high demand over, so full phase curves are only expected to be taken of a few key targets. Additionally these targets will be limited to short period planets, as the single visit duration is limited to 48h. Hence common mode techniques such as ours will allow for some climate studies of planets not observed by full phase curves (e.g. see Stevenson 2020 for specific applications to JWST and non-transiting planets). Although the live performance of the telescope will not be known until data are analyzed, in particular relating to any wavelength-dependent noise components, common-mode methods such as this technique will be needed to characterize the performance alongside classical fits to the systematics.

In summary partial phase curves will likely require dedicated observing programs to succeed, but should be considered for future spectroscopic space based facilities, such as JWST and ARIEL. We recommend special care should be taken when observing targets in eclipse and transit in the future as additional science beyond the goals of the program may be possible if their alignment on the detector is ensured.

4.5 Conclusions

We present the first emission spectrum of an exoplanet measured in quadrature outside of a phase curve. We measure the brightness T=2124±314 K. We present our new technique for extracting planet spectra at different phases from spectroscopic phase curves, based on common mode methods. We show how this technique succeeds in extracting spectra of WASP-12b obtained with HST/WFC3 G141 in emission at eclipse and quadrature, but also how it fails at transit where we find the data are offset in position on the detector.

We obtain relative emission spectra of WASP-12b at eclipse and quadrature, and find that the planet exhibits a decrease in temperature with longitude expected for nominal day-night redistribution of 1062±516 K. This result is in line with the findings from full-orbit Spitzer phase curves, that suggest the presence of cool gas in the system not visible at shorter wavelengths (Bell et al., 2019).

We find that our extracted spectrum is steeper than expected from global circulation models, and while we do not have a clear explanation for this, we find that this cannot be explained by

non-equilibrium water fractions or increased local temperature. We also calculate from our global circulation models that the dayside atmospheric pressures probed by our observations should be equilibrium with respect to thermal dissociation of water and hydrogen.

We outline how to the success of this data analysis technique in the future, either through continuous phase curve observations or by careful monitoring of the PSF of individual visits in a partial phase curve. This will likely be a useful observing method for JWST and ARIEL, where partial phase curves have a greater chance of succeeding. Our new technique may also open a window for further studies on archival data, as well verification of existing results from full orbit phase curves.

Acknowledgements

We would like to thank the STScI helpdesk and in particular Varun Bajaj for fielding our many questions on the WFC3 performance. We would also like the thank Dr. Channon Visscher for their insights on dissociation timescales.

J.M.D acknowledges support from the Amsterdam Academic Alliance (AAA) Program, and the European Research Council (ERC) European Union's Horizon 2020 research and innovation programme (grant agreement no. 679633; Exo-Atmos). This work is part of the research programme VIDI New Frontiers in Exoplanetary Climatology with project number 614.001.601, which is (partly) financed by the Dutch Research Council (NWO).

4.6 Appendix

Central λ	Eclipse Fp/Fs	(ppm) Error	Quad Fp/Fs	(ppm) Error
1.14	-750	159	-553	224
1.16	-34	152	38	216
1.19	-602	150	-62	212
1.22	-390	148	89	210
1.25	-617	149	-506	211
1.27	-590	147	285	208
1.30	-69	147	70	207
1.33	-69	147	-577	208
1.35	14	150	-204	213
1.38	269	152	126	215
1.41	131	154	-2	217
1.44	287	157	491	222
1.46	276	161	-85	227
1.49	143	162	-14	229
1.52	891	167	242	235
1.55	76	171	-157	241
1.57	700	174	543	246
1.60	332	180	274	255

Table 4.3: Extracted eclipse and quadrature spectra.

Wavelength	Dilution (%)	Error
1.133	3.39	0.13
1.160	4.68	0.13
1.187	4.81	0.13
1.214	5.04	0.14
1.242	5.39	0.14
1.269	5.71	0.15
1.296	5.89	0.15
1.323	5.97	0.15
1.350	6.14	0.17
1.377	5.55	0.18
1.405	5.74	0.20
1.432	5.39	0.21
1.459	5.51	0.23
1.486	5.74	0.24
1.513	5.70	0.23
1.541	6.09	0.26
1.568	6.47	0.26
1.595	6.77	0.28

Table 4.4: Dilution correction for the contribution of WASP-12B/C to the planet spectra. The dilution here is defined as the flux of the companions relative to the flux of WASP-12A, shown here as a percentage.

Chapter 5

The brightness temperature of the nightside of WASP-18b

Jean-Michel Désert, Jacob Arcangeli

in preparation

Abstract

Short-period gas giant exoplanets tidally locked to their parent stars on circular orbits have permanent daysides and nightsides. The hottest of these hot-Jupiters, the ultra-hot Jupiters, have dayside temperature exceeding 2000 K and often feature a day and night temperature difference greater than 1000 K. Such giant planets have begun to emerge as a planetary laboratory for understanding gas chemistry and atmospheric physical processes, including cloud formation, in new regimes.

We apply our new phase-curve extraction method to the previously analyzed archetype of an UHJ, WASP-18b. We re-analyse the HST/WFC3 phase curve of WASP-18b (Arcangeli et al., 2019) in order to free the data from any instrumental assumption and look for atmospheric signatures that could emerge from different planet longitudes. Previous analysis was not able to reveal any spectral variations as function of the orbital phase of this planet, in part due to the uncertainty in the shape, frequency, and amplitude of the long-term instrumental systematics. We show that, by applying a common-mode method that does not assume a functional form for the systematics, we are able to extract the relative planetary spectrum at each phase. These spectra are consistent with previous analysis for the dayside spectrum, but in addition allows for the measurement of the nightside spectrum.

The newly extracted spectra are compared to previous studies, and are used to infer the brightness temperature of the nightside, found to be 1612±171 K. From the dayside and nightside brightness temperatures, we derive a very low Bond albedo ($A_B = 0.006 \pm 0.006$) and an inefficient energy budget, consistent with previous studies for this planet.

5.1 Introduction

Short-period gas giant exoplanets, the hot-Jupiters (HJs), are expected to be on circularised orbits and tidally locked into synchronous rotation, with permanent daysides that face their host stars and permanent nightsides. A subset of these exoplanets, the Ultra-hot Jupiters (UHJs), are the hottest close-in giant planets known to date. These UHJs have dayside temperatures reaching $\gtrapprox$ 2000 K (Parmentier et al. 2018; Kreidberg et al. 2018; Arcangeli et al. 2019; Lothringer et al. 2018; Bell & Cowan 2018). While these objects are *bona fide* planets, their atmospheres reach temperatures at low pressures comparable to stellar atmospheres. The strongly irradiated dayside of these planets exhibit several remarkable features, including thermal inversions (e.g., Haynes et al. 2015; Evans et al. 2017; Sheppard et al. 2017), evidence for stronger thermal irradiation and/or poor heat redistribution as their dayside temperature increase (Baxter et al. 2020), lack of strong water absorption as caused by molecular dissociation and H- opacities that leads to lower radiative cooling efficiency (Arcangeli et al. 2018; Kreidberg et al. 2018; Kitzmann et al. 2018; Lothringer et al. 2018; Parmentier & Crossfield 2018), presence of neutral and ionized metals (e.g., Hoeijmakers et al. 2018, 2019; Pino et al. 2020; Ben-Yami et al. 2020) and evidence for heat transport through molecular dissociation and recombination (Bell & Cowan 2018; Komacek & Tan 2018; Mansfield et al. 2018; Parmentier et al. 2018) and cloud formation (Armstrong et al. 2016. Overall, UHJs have emerged as planetary laboratory for understanding gas chemistry, atmospheric heat redistribution, day/night contrast, cloud formation and ultimately their energy budget. These objects currently challenge our understanding of planetary atmospheres and the models we use to interpret observations.

The overall thermal budget of a planet's atmosphere is defined by the thermal absorption and emission of both the dayside and the nightside hemispheres. This is particularly true for tidally locked planets or non-eccentric orbits. It is therefore necessary to measure both the dayside and nightside thermal emission for these planets. While the brightness temperatures of HJ daysides have been measured for a large number of objects (Triaud et al., 2015; Garhart, 2019; Baxter et al., 2020), measurements of their nightside brightness temperatures remains more sparse (Komacek et al., 2017; Keating et al., 2019). The thermal flux from the nightside of several hot Jupiters has been measured essentially using broad band photometric measurements (Knutson et al., 2007; Snellen et al., 2009; Borucki et al., 2009; Cowan et al., 2012; Dang et al., 2018; Zhang et al., 2018; Shporer et al., 2019). There are remarkable features related to night sides that have emerged from these phase curves observations, namely the sharp day-night contrasts measured, the nightsides of HJs which appear to be at roughly the same temperature of 1000 K while their dayside temperatures increase linearly with equilibrium temperature, the trend in which the atmospheres of the hottest planets are less efficient at redistributing the stellar energy absorbed on their daysides to their nightside, and the lack of a clear trend in phase offsets with equilibrium temperature (e.g., Perez-Becker & Showman 2013; Komacek & Showman 2016; Keating et al. 2019. One hypothesis has been suggested that nightside clouds could be playing a noticeable role in modulating the thermal emission from HJs, and could be responsible for the uniformly hot nightside temperatures on short-period gas giants (Keating et al., 2019).

One way to measure the nightside emission of a planet is to gather phase-curve observations. Phase-curves have been used successfully to study the change in regime from the dayside to the nightside of several UHJs (Knutson et al., 2007; Cowan et al., 2007). More specifically, it has been found that efficient dissipation is needed in the atmosphere to match the large observed day-night contrasts (Knutson et al. 2007; Stevenson et al. 2014b; Kreidberg et al. 2018; Arcangeli et al. 2019. In fact, the day-night contrasts are often so large that spectra of the planet taken at different phases are dominated by the hot-spot whenever it is visible. In this context, transmission spectra of the limb and emission spectra from various planetary longitudes are key avenues for studying the changes in chemistry with longitude in these atmospheres, and potentially looking for evidence of clouds (Schwarz et al., 2015).

Retrieving the physical information from phase curves poses several challenges. Recent works have shown the inherent difficulties to extracting phase-curve variations from data taken with the Hubble Space Telescope (HST). This is, in part, due to the long-term systematics of HST that operate on the same timescale as the phase variations. Additionally, stellar ellipsoidal variations can introduce another degeneracy that renders the extraction of the longitudinal flux extremely challenging (Arcangeli et al., 2019). These phase-curve extractions typically use a range of models for the instrumental and astrophysical phase-curve variations, that can lead to different temperature maps inverted from the same observation. This is because the degeneracies between the astrophysical signals and instrumental systematics prevent the retrieval of a unique thermal map (Kreidberg et al., 2018).

We recently demonstrated that a common-mode correction can be applied to HST/WFC3/G141 data, that allows for a unique extraction of spectra of such planets as viewed from any orbital phases Arcangeli 2020. The strength of this method is that it assumes no analytic form for the systematics or for the phase-curve variations, and naturally removes any effect of stellar ellipsoidal variations. The base assumption of this method is that the systematics are largely wavelength-independent, which has been shown to hold true for such observations with HST as they are close to photon-noise limited Deming et al. 2013; Kreidberg et al. 2014b; Stevenson et al. 2014b. While this method removes the information about the absolute amplitude of the spectrum, relative amplitudes can still be measured to constrain temperature changes and potentially chemistry. Therefore, this new method offer the possibility to extract information from a phase curve that could not have been accessible before, such has the nightside, because it is free of any assumptions for the instrumental corrections.

Currently, one of the best target to measure spectra at various orbital phase without any assumptions for the instrumental correction is WASP-18b. The phase curve of WASP-18b has been measured with HST/WFC3/G141, where a functional form was used to deal with instrumental effects (Arcangeli et al., 2019), which provides a reference point for this new technique.

WASP-18b is an ultra-hot Jupiter, being among the hottest close-in gas giants known so far. Its ultra-short period cause very high irradiation from its F-type star and, hence leads to a extreme temperature difference between day- and nightside. It is thus an interesting target to test variations in the atmospheric properties as function of the orbital phase, as well as measure the heat redistribution efficiency and albedo, and thus derive its overall

energy budget. Ultimately, this target provide us with an opportunity to test an archetype of atmosphere from an Ultra-hot Jupiter.

We start by presenting our technique and methods in Section 5.2.2. We then present our new results for WASP-18b in Section 5.3, as well as an evaluation of the systematics removal. We compare our results to published spectra and theory in Section 5.4.

5.2 Data and Methods

5.2.1 Data

The data used are from the full-orbit phase curve of WASP-18b taken with HST (part of GO:13467, PI:Bean). The phase curve was previously published in (Arcangeli et al., 2019).

We use our existing pipeline to extract the lightcurves at each wavelength, and apply the common-mode correction described in Arcangeli (2020). We perform on additional correction to the data to account for a visit-drift of the telescope, described in Section 5.2.3.

5.2.2 Time dependent systematics correction

In order to remove the instrument systematics and extract the planet signal we use the technique outlined in (Arcangeli, 2020), which is essentially a common-mode correction in two steps. In the first step, we divide each spectroscopic phase curve by the uncorrected raw white-light phase curve (integrated over the full wavelength range) to remove any common-mode instrument systematics, stellar ellipsoidal or long term variations. This produces a common-mode corrected spectrum for each exposure. We combine the exposures of each HST orbit to produce a single common-mode corrected spectrum per orbit.

The second step is to divide these common-mode corrected spectra by a reference spectrum of the star (the stellar spectrum taken during secondary eclipse), corrected in the first step for instrument systematics, to produce a relative spectrum of the planet (Fp/Fs) at each phase up to a normalisation constant.

5.2.3 Wavelength dependent systematics correction

We check for the presence of wavelength-dependent residuals across the visit by comparing the two in-eclipse stellar fluxes taken at the beginning and end of the observations. In the raw white-light curve (show in Figure 1 of Arcangeli et al. 2019), these eclipses are already very well alligned, with a drop of only 540ppm ($<$0.6%) in raw flux going from the first to the second eclipse. The ratio of the two extracted stellar spectra, taken from the two measured eclipses (star alone), if well corrected should lie at one. However, this ratio yields a slope of about 400 ppm over the full wavelength range, which implies additional systematics have not been corrected. We investigate this slope and we find that there are residuals in the positional drift of the dispersed spectrum on the detector, over the course of the first visit, that can reproduce this systematic slope. This is identical to (Arcangeli, 2020), where

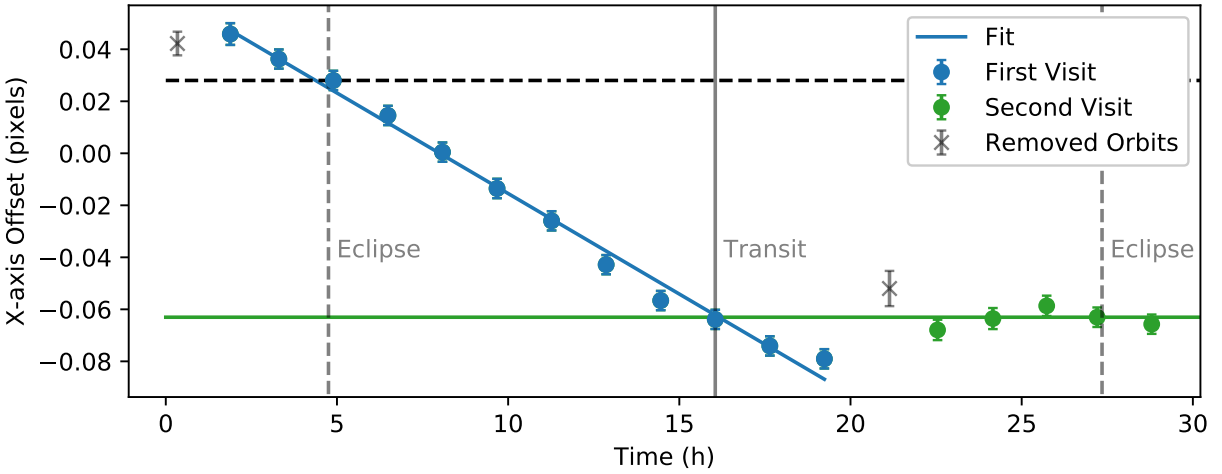

Figure 5.1: Measured positional shifts of spectra in the dispersion direction at each orbit over the full light curve are shown by the data points with errorbars. Data in blue were taken before the half-orbit break, and data in green were taken after the break. The blue line is the linear slope used to calculate the positional-drift-corrected stellar spectrum for orbits in the first visit. The ratio of the first eclipse to the second eclipse is fixed to 1:0 during the first eclipse, and 0:1 in transit.

positional shifts introduced a slope in the extracted HST spectra. The key difference is that in the phase curve of WASP-18b there are two reference baselines, that allow for a correction of the systematic effects caused by the positional shifts of the spectra. We measured the positional shift of the spectrum on the detector over the course of the observations, by cross-correlating the spectrum of each orbit with a reference spectrum averaged over the whole visit, the results of which are shown in Figure 5.1.

We use our measured positional shifts to apply a final correction to our data and remove this additional slope see in the spectra, described below. This correction is performed in addition to the common mode correction of Arcangeli (2020). We define the stellar spectrum at each time in the first visit to be a linear combination of the stellar spectra taken during the first and second eclipse, while using only the second eclipse for the second visit (Figure 5.1). We find that this correction reduces the slope between the two in-eclipse spectra to within the errors of the observations. The relative contribution of the first and second eclipse to each orbit is determined by a fit to the offsets by a linear slope, shown by the blue line in Figure 5.1. This allows us to remove the slope introduced by the positional drift as it is divided out by our new stellar spectra. It also corrects for continuous stellar variability, if present, between the two eclipses, however, WASP-18 is known to be quiet and no evidence for stellar variability was found by Arcangeli et al. (2018) and Arcangeli et al. (2019). Finally, we have tested that this method also provides a better correction than an interpolation as it is not as sensitive to the under-sampling of the spectrum.

5.2.4 Testing the corrections and Noise level

We estimate the quality of our systematic correction by comparing the systematics-corrected in-eclipse orbits to a flat line at different wavelengths. As the star alone is observed during these two separate orbits, the scatter between the exposures within each in-eclipse orbit shows the level to which the correction was successful. Both eclipses show the same level of scatter. Ellipsoidal variations mean that the star does vary in brightness over the course of an eclipse, but only at the few ppm as the duration of the eclipse is short.

We find that we reach close to the propagated photon noise precision, $<$20% above photon noise for 10 bins or more (Figure 5.2). This implies that the star and the instrumental systematics within an orbit are very well corrected by the common-mode method, and that any residual wavelength dependent effects such as stellar variability are small.

5.3 Results

5.3.1 Measuring brightness temperatures

We measure the brightness temperature from the common-mode corrected spectra at each phase by fitting a blackbody emission model for the planet. This model consists of a blackbody ratio for the planet and star, using the values of (Hellier et al., 2009), with an additional additive constant of normalization between the model and the data, since the data are relative spectra in wavelength. We perform a joint fit to the planets temperature and

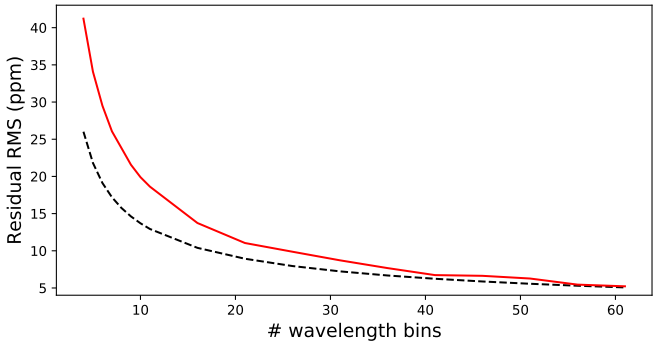

Figure 5.2: Scatter of in-eclipse exposures after common-mode correction has been applied, plotted against number of wavelength channels used.

the normalization constant, and report the measured values in Table 5.1. Below we discuss several key features from this extracted thermal phase curve.

5.3.2 Dayside emission spectra

An immediate outcome of the common-mode extraction of the planet's spectra at any orbital phases is the dayside emission, which can be directly compared to the previously measured HST/WFC3 spectra by Sheppard et al. (2017), Arcangeli et al. (2018), and Arcangeli et al. (2019). In the current paper, we extract the dayside emission spectra of WASP-18b in a novel way: we measure both the emission spectra before and after the eclipse, unlike the classical method that produces one emission spectrum extracted from the combined information of the emission from before and after the eclipse, and an assumption on how the planet and star flux change in between. The emission spectra we measure in the present case is different since it is derived from the first orbit before eclipse and the first orbit after eclipse. We checked that the two spectra, before and after eclipses, are consistent with each other for each eclipse. Therefore we combined the spectra obtained for the two eclipses together, and end-up with one spectrum measured before eclipse and one spectrum measured after eclipse (see Figure 5.4).

5.3.3 Thermal phase curve

For the phase-resolved spectra extracted above, we bin each HST orbit to produce a relative spectrum per orbit, labelled and coloured in Figure 5.3 by their midpoint in orbital phase. These phase resolved relative spectra are generally featureless, with a continuous (smooth) changing slope as function of the orbital phase, which we interpret as a longitudinal change of the brightness temperature. For this interpretation, we assume that the planet emission

is disk averaged for each individual orbital phase, and that the emission at each phase can be approximated by blackbodies.

We perform simple blackbody ratio fit to each of the orbit relative spectra, to recover the thermal phase curve of the planet. Here we assume a blackbody curve for the stellar spectrum, with a temperature of 6400 K (Hellier et al., 2009). We highlight that these may not be the most accurate measures of the brightness temperature since the spectra may not be approximated by blackbodies. Nevertheless, this approach remains a good estimate of the temperature from the slope of the spectra alone given the precision of our extracted spectra. We demonstrates that there is a good agreement between our extracted temperatures and the previous estimates at every phases Arcangeli et al. (2019), with temperatures only a few 100K lower extracted here for phases 0.6-0.8.

5.3.4 Nightside emission spectrum

Previous analysis of the same data was not able to retrieve the emission of the nightside of WASP-18b (Arcangeli et al., 2019). The main reason for this is that a functional form of the instrumental systematics was applied that was found to be highly degenerate with the nightside emission. Our new method, which uses the common mode extraction, provides a way to estimate the thermal emission of the planet's nightside from it's emission spectrum in the HST/WFC3/G141 bandpass, as measured before and after the planet transit. We combine the common mode corrected spectra obtained from the orbit before transit (phase 0.93) and the orbit after transit (phase 0.08) to form our nightside spectrum. We measure the nightside brightness temperature to be 1612 ± 171 K, with a constant value $C = 60 \pm 42$ ppm. We present the extracted nightside spectrum of WASP-18b in Figure 5.6.

5.3.5 Propagation of uncertainties

The uncertainties on the final spectra for the common-correction are propagated throughout the common-mode correction as described in Arcangeli (2020). This includes propagating the uncertainty on the white-light curve, which is used to divide out the systematics, through to the final spectra at each phase.

In Figure 5.5 the errorbars on our fitted temperatures appear significantly larger than the uncertainties on the white-light curve of Arcangeli et al. (2019). This is due to two effects, the first is that we fit a blackbody temperature to a relative spectrum, and therefore must fit for an additional parameter which is the normalization of the blackbody. The corner plot in Figure 5.7 shows the degeneracy between the fitted temperature and normalization, which is a large part of the uncertainty on the final fitted temperatures. The second effect is that the common-mode correction propagates the uncertainty on the white-light curve (or template systematics) through to the final spectra. This results in a systematic uncertainty on each spectrum in addition to the random noise present in the data, which can be seen by the minimal scatter between orbit temperatures shown in Figure 5.5. The uncertainties on the white-light curve in Arcangeli et al. (2019) include only the uncertainty on the extracted

light curve, and not the propagation of the uncertainties on the parameters of the systematics fit, and hence appear significantly smaller.

5.4 Discussion

5.4.1 Comparison to previous results

Our extracted spectra with the presented in this paper can be compared to the previous direct-fit method applied in Arcangeli et al. (2019), as well as the atmospheric circulation models used in that work. The key differences in approach are that, in this work, no model is assumed for the systematics or the planet's phase variation, but also the spectra extracted are relative measurements in wavelength rather than absolute planet to star flux ratios as obtain with the classical method for phase curve analysis.

We first compare the new dayside emission spectra of WASP-18b near eclipse, as measured before and after eclipses, and that is presented in this paper to the dayside emission spectra of this planet that has been extracted in classical fashions, i.e., from the fit of secondary eclipses Arcangeli et al. 2018, 2019. The full comparison of the new extracted emission spectra is made using three different methods, and two different observations in 5.4. We emphasise that the spectrum from Arcangeli et al. (2018) results in the combination of five different eclipses, while the spectra presented in Arcangeli et al. (2019) and in the current paper are from the two eclipses measured within the semi-continous phase curve observation. This step provides further confidence in the accuracy and robustness of the novel method to extract the relative emission spectra presented in Arcangeli (2020) and that is used in the current paper. We describe below how the brightness temperatures is measured at every orbital phase, including right before and after eclipses.

The next feature we can compare is the phase curve extracted with both methods. As seen in Figure 5.5, both extractions point towards a small hot spot offset, which confirms that the lack of offset is not dependent on the use of an instrumental functional form for its correction. However, the largest discrepancy between the two extractions appears to be between phases 0.6-0.8, where our common-mode method recovers a less steep planetary spectrum, approximately 150K less hot in temperature. Hence our extracted temperatures in this work are more consistent with weaker drag models than (Arcangeli et al., 2019).

The discrepancies between the two phase-resolved temperature extractions could be due to a number of key differences. Firstly, the estimation of the temperature from the blackbody fits to our relative spectra may be inaccurate, in particular towards the nightside since there could be spectral features that cause the spectrum to significantly deviate from a blackbody curve.Physically, this difference could be a sign of asymmetry in the temperature map of the planet, as this would not be well captured by the sinusoidal model used in Arcangeli et al. (2019), however the poor phase coverage between 0.2-0.4 in phase does not allow us to conclude on this point.

Finally we compare the nightside brightness temperature to previous measurements. One of the key difference between the two phase-curve spectral extractions is the non-detection

of the nightside in (Arcangeli et al., 2019), compared to the nightside spectrum measured in this work. This non-detection was attributed to the low signal from the nightside coupled with the large uncertainty on visit-long systematics around the nightside. Here we see a clear advantage of the common-mode method, as the systematics are removed using the white-light curve, allowing for the nightside spectrum to be extracted. Similarly, Maxted et al. 2013 measured a nightside brightness temperature T_{bright} at low SNR to be $815K \pm 463$. Although these authors forced the phase curve to reach a minimum at zero, there findings is consistent with our determination of T_{bright} in the WFC3/G141 bandpass at 1 σ level. Similarly, our measurement T_{bright} is consistent with the upper limit measured in the red optical with TESS (Shporer et al., 2019).

5.4.2 Global energy budget

Based on dayside effective temperatures alone, one cannot simultaneously specify Bond albedo and heat recirculation efficiency (Cowan & Agol, 2011). This degeneracy can be broken by having both the dayside and nightside brightness temperatures.

The depth of secondary eclipse is approximately the ratio of the planet's day-side flux, $F_{\rm day}$, to the stellar flux, F_*. We assume that the planet's day and night-side radiate as blackbodies ($F = B_\lambda(T)$) and that the host star emits with a NIR brightness temperature $T_{\rm bright}$. The resulting planet-star flux ratio is:

$$\frac{F_{\rm day}}{F_*} = A_g \left(\frac{R_p}{a}\right)^2 + \frac{B_\lambda(T_{\rm day})}{B_\lambda(T_{\rm bright})}\left(\frac{R_p}{R_*}\right)^2, \tag{5.1}$$

where R_p is the planetary radius and the ratios R_p/a and R_p/R_* are well-constrained. We therefore can measure the wavelength-dependent geometric albedo, A_g, the ratio of the total brightness of the planet at full phase to that of a Lambertian disk with the same cross-section. We find that the geometric albedo is low in the HST/WFC3/G141 bandpass, $A_g = 0.005 \pm 0.006$

However, a planet's energy budget is largely determined by its Bond albedo. The Bond albedo, A_B, is the fraction of the incident stellar flux that is reflected by the planet. Based on a planet in a circular orbit with two isothermal hemispheres and neglecting the planet's remnant heat of formation. Treating the host star as a blackbody, the equilibrium temperature of a planet's day and night hemispheres is, respectively

$$T_{\rm day}^4 = (1 - A_B)(1 - P_n)\left(\frac{R_*^2}{2a^2}\right) T_{\rm eff}^4, \tag{5.2}$$

and

$$T_{\rm night}^4 = (1 - A_B)P_n\left(\frac{R_*^2}{2a^2}\right) T_{\rm eff}^4, \tag{5.3}$$

where R_* and $T_{\rm eff}$ are the star's radius and effective temperature, a is the planet's semi-major axis and P_n quantifies the portion of the absorbed stellar energy advected to the planet's night-side ($P_n = 0$ for no redistribution; $P_n = 0.5$ for full redistribution, Burrows et al.

2006). Hence, by measuring both the day and the night side brightness temperatures, we measure of the Bond albedo, $A_B = 0.006 \pm 0.006$, and heat redistribution, $P_n = 0.127 \pm 0.048$. These measurements confirm what was expected for this planet in terms of low Bond albedo and relatively inefficient day/nightside energy redistribution from previous studies Nymeyer et al. 2011; Iro & Maxted 2013; Schwartz & Cowan 2015.

Arcangeli et al. (2019) illustrates that the uncertainty on the equilibrium temperature limits any conclusions that could be drawn from the dayside alone. However the measurement of both the redistribution efficiency and the Albedo alleviates the uncertainties from the degeneracies between atmospheric metallicity and redistribution efficiency (see Figure-6 Arcangeli et al. 2019), and can significantly constrain 1D and GCM atmospheric models.

5.4.3 Implications for the planet's atmosphere

Infrared phase curves of transiting hot Jupiters present a trend in which the atmospheres of the hottest planets are less efficient at redistributing the stellar energy absorbed on their daysides and thus have a larger day-night temperature contrast than colder planets (Perez-Becker & Showman, 2013; Komacek & Showman, 2016; Keating et al., 2019). Theory predicts that the radiative heating and cooling play the largest role in controlling dayside-nightside temperature differences of HJs, resulting in dayside-nightside temperature differences that increase with increasing stellar irradiation and decrease with increasing pressure (Perez-Becker & Showman, 2013; Komacek & Showman, 2016). WASP-18b being an UHJ with a large phase curve amplitude and lack of hot-spot offset (Maxted et al., 2013; Arcangeli et al., 2019), as well as high surface gravity (Parmentier et al., 2018) could be partly explained by this theory. In fact,our new estimate of the nightside temperature of 1,600 K brings WASP-18b's nightside temperature closer to what is expected from the trend revealed by Keating et al. 2019 as compared to the previous estimate from Maxted et al. 2013. However, it may remain the case that a frictional processes, as expressed in terms of a drag timescale, is necessary to explain that the heat redistribution efficiency drops for this planet.

It has also been suggested that the reduction in phase curve amplitude measured for some UHJs as compared to the hot Jupiters could be due to hydrogen dissociation and recombination (Komacek & Tan, 2018; Keating & Cowan, 2017; Tan & Komacek, 2019). In addition to the shape of the phase curve, the evidence for H- opacity in the atmosphere of WASP-18b further emphasises the need for an efficient atmospheric drag of unknown origin at this point (Arcangeli et al., 2019).

Importantly. the circulation models mentioned above do not include the effects from non-equilibrium chemistry such as clouds. Cloud coverage is expected on the nightside of this planet (Helling et al., 2019a), and has been inferred as a global property of hot Jupiter nightsides from their apparently uniform temperatures (Keating et al., 2019). Cloud coverage on the nightside of WASP-18b would be expected to not exhibit spectral features at this resolution, except as black body emission, although spectra features could be seen from the atmosphere at lower pressures. This seems to be supported in first order by our observation.

Phase	Tp K	σTp K	C ppm	σC ppm	Time h
0.43	2666	175	-760	201	0.0
0.58	2485	111	-569	109	3.4
0.65	2418	101	-505	93	5.0
0.72	2136	86	-285	57	6.5
0.79	1871	127	-143	55	8.1
0.86	1682	149	-77	43	9.7
0.93	1476	242	-33	40	11.3
0.08	1730	147	-91	48	14.5
0.15	1887	188	-150	84	16.1
0.36	2653	132	-745	149	21.0
0.43	2671	145	-766	167	22.5
0.57	2752	140	-862	171	25.7

Table 5.1: Measured blackbody temperatures sorted by time (hours) since start of visit. The phase is the central phase of the orbit, with each orbit having a width of 0.032 in phase.

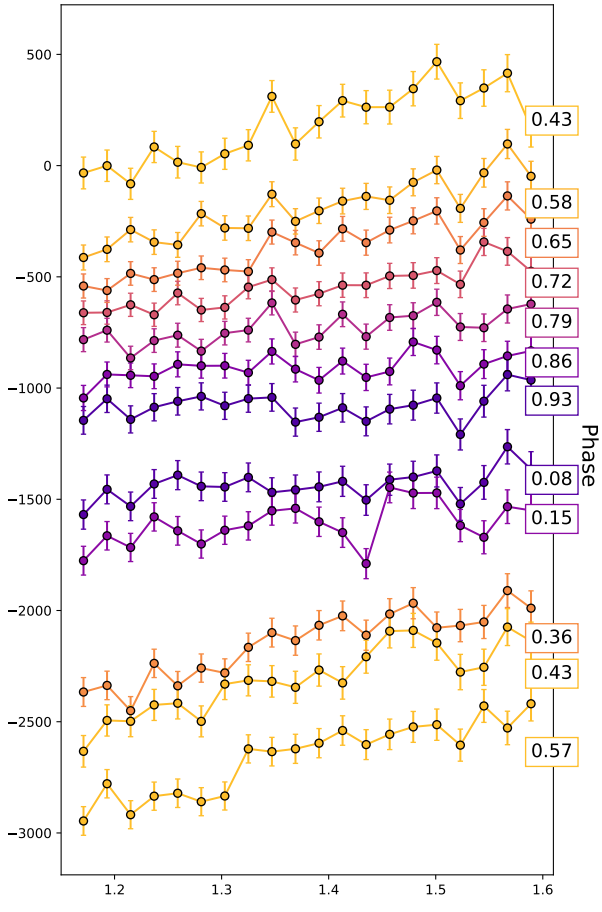

Figure 5.3: Emission spectra for each orbit, offset in y for clarity by time observed and coloured by corresponding phase of orbit.

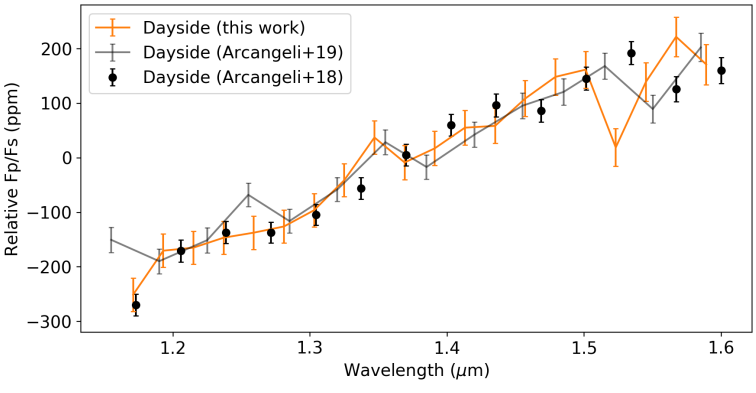

Figure 5.4: Comparison of the extraction of the dayside spectrum of WASP-18b from three different methods, and two sets of data.

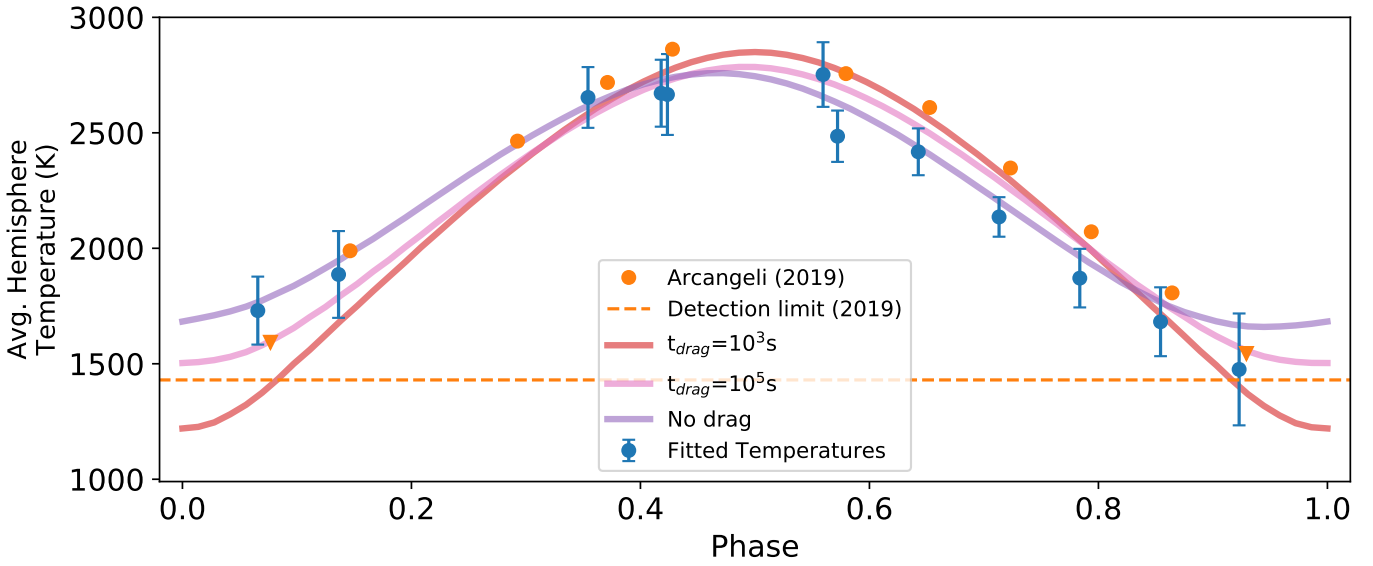

Figure 5.5: Thermal phase curve of WASP-18b, from blackbody fits to orbit spectra (shown in blue). Plotted in orange are the published white-light phase curve results from (Arcangeli et al., 2019), converted to brightness temperatures. Uncertainties on these calculated brightness temperatures are not shown, but the 3σ nightside upper limit is shown by the dotted line in orange.

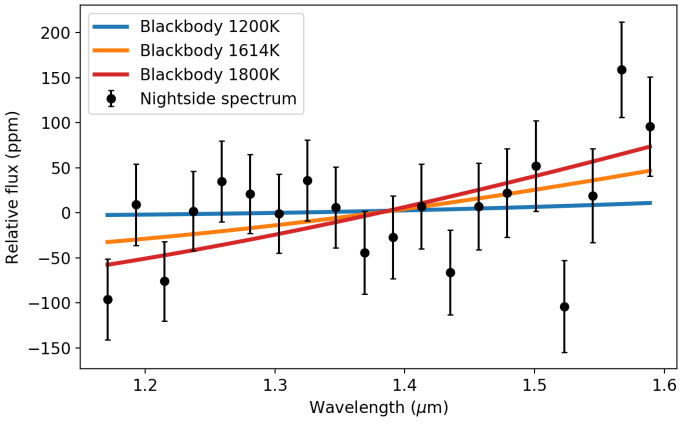

Figure 5.6: Nightside cmmon-mode corrected spectrum of WASP-18b combined from orbits directly before and after transit and compared to blackbody models.

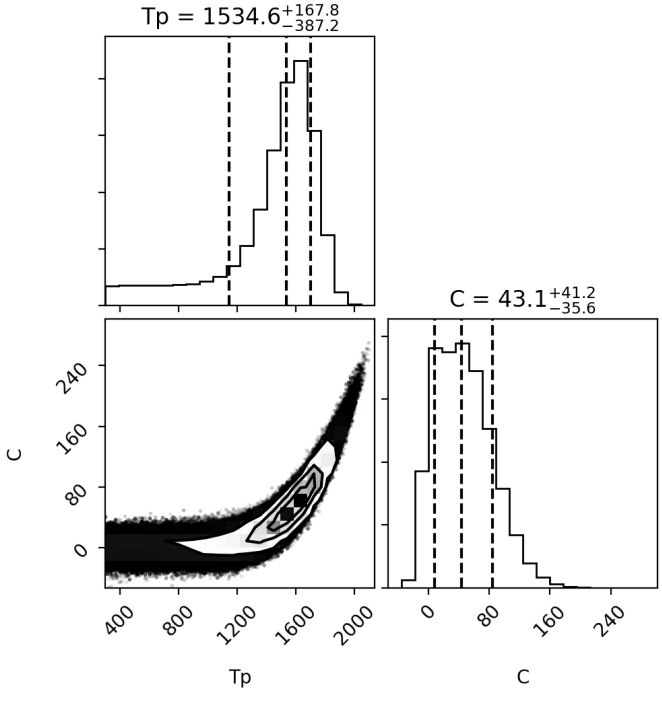

Figure 5.7: Measurement of the brightness temperature from the night side using a MCMC approach.

Bibliography

Adcroft, A., Campin, J.-M., Hill, C., & Marshall, J. 2004, *Implementation of an Atmosphere Ocean General Circulation Model on the Expanded Spherical Cube*, Monthly Weather Review, 132, 2845

Allart, R., Lovis, C., Pino, L., et al. 2017, *Search for water vapor in the high-resolution transmission spectrum of HD 189733b in the visible*, A&A, 606, A144

Amundsen, D. S., Mayne, N. J., Baraffe, I., et al. 2016, *The UK Met Office global circulation model with a sophisticated radiation scheme applied to the hot Jupiter HD 209458b*, A&A, 595, A36

Anglada-Escudé, G., Amado, P. J., Barnes, J., et al. 2016, *A terrestrial planet candidate in a temperate orbit around Proxima Centauri*, Nature, 536, 437–440

Arcangeli, J., Désert, J.-M., Line, M. R., et al. 2018, *H^- Opacity and Water Dissociation in the Dayside Atmosphere of the Very Hot Gas Giant WASP-18b*, ApJ, 855, L30

Arcangeli, J., Désert, J.-M., Parmentier, V., et al. 2019, *Climate of an ultra hot Jupiter. Spectroscopic phase curve of WASP-18b with HST/WFC3*, A&A, 625, A136

Arcangeli, J. e. a. 2020, *WASP-12b paper*, A&A, 625, A136

Armstrong, D. J., de Mooij, E., Barstow, J., et al. 2016, *Variability in the atmosphere of the hot giant planet HAT-P-7 b*, Nature Astronomy, 1, 0004

Bakos, G. Á., Csubry, Z., Penev, K., et al. 2013, *HATSouth: A Global Network of Fully Automated Identical Wide-Field Telescopes*, PASP, 125, 154

Barman, T. S., Hauschildt, P. H., & Allard, F. 2001, *Irradiated Planets*, ApJ, 556, 885

Barstow, J. K., Aigrain, S., Irwin, P. G. J., & Sing, D. K. 2017, *A Consistent Retrieval Analysis of 10 Hot Jupiters Observed in Transmission*, ApJ, 834, 50

Batalha, N. M. 2014, *Exploring exoplanet populations with NASA's Kepler Mission*, Proceedings of the National Academy of Science, 111, 12647

Batygin, K., Stanley, S., & Stevenson, D. J. 2013, *Magnetically Controlled Circulation on Hot Extrasolar Planets*, ApJ, 776, 53

Batygin, K. & Stevenson, D. J. 2010, *Inflating Hot Jupiters with Ohmic Dissipation*, ApJ, 714, L238

Baxter, C., Désert, J.-M., Parmentier, V., et al. 2020, *Spitzer Survey: Hot*, å, 639

Bean, J. L., Miller-Ricci Kempton, E., & Homeier, D. 2010, *A ground-based transmission spectrum of the super-Earth exoplanet GJ 1214b*, Nature, 468, 669

Beatty, T. G., Madhusudhan, N., Tsiaras, A., et al. 2017, *Evidence for Atmospheric Cold-trap Processes in the Noninverted Emission Spectrum of Kepler-13Ab Using HST/WFC3*, AJ, 154, 158

B

Bell, K. L. & Berrington, K. A. 1987, *Free-free absorption coefficient of the negative hydrogen ion*, Journal of Physics B Atomic Molecular Physics, 20, 801

Bell, T. J. & Cowan, N. B. 2018, *Increased Heat Transport in Ultra-hot Jupiter Atmospheres through H_2 Dissociation and Recombination*, ApJ, 857, L20

Bell, T. J., Nikolov, N., Cowan, N. B., et al. 2017, *The Very Low Albedo of WASP-12b from Spectral Eclipse Observations with Hubble*, ApJ, 847, L2

Bell, T. J., Zhang, M., Cubillos, P. E., et al. 2019, *Mass loss from the exoplanet WASP-12b inferred from Spitzer phase curves*, MNRAS, 489, 1995

Ben-Yami, M., Madhusudhan, N., Cabot, S. H. C., et al. 2020, *Neutral Cr and V in the Atmosphere of Ultra-hot Jupiter WASP-121 b*, ApJ, 897, L5

Benneke, B. 2015, *Strict Upper Limits on the Carbon-to-Oxygen Ratios of Eight Hot Jupiters from Self-Consistent Atmospheric Retrieval*, arXiv e-prints, arXiv:1504.07655

Bergfors, C., Brandner, W., Daemgen, S., et al. 2013, *Stellar companions to exoplanet host stars: Lucky Imaging of transiting planet hosts*, MNRAS, 428, 182

Bergfors, C., Brandner, W., Henning, T., & Daemgen, S. 2011, *Stellar companions to exoplanet host stars with Astralux*, in IAU Symposium, Vol. 276, The Astrophysics of Planetary Systems: Formation, Structure, and Dynamical Evolution, ed. A. Sozzetti, M. G. Lattanzi, & A. P. Boss, 397–398

Berta, Z. K., Charbonneau, D., Désert, J.-M., et al. 2012, *The Flat Transmission Spectrum of the Super-Earth GJ1214b from Wide Field Camera 3 on the Hubble Space Telescope*, ApJ, 747, 35

Birkby, J. L. 2018, *Exoplanet Atmospheres at High Spectral Resolution*, arXiv e-prints, arXiv:1806.04617

Birkby, J. L., de Kok, R. J., Brogi, M., et al. 2013, *Detection of water absorption in the day side atmosphere of HD 189733 b using ground-based high-resolution spectroscopy at 3.2μm.*, MNRAS, 436, L35

Birkby, J. L., de Kok, R. J., Brogi, M., Schwarz, H., & Snellen, I. A. G. 2017, *Discovery of Water at High Spectral Resolution in the Atmosphere of 51 Peg b*, AJ, 153, 138

Bolton, S. J. & Bolton. 2010, *The Juno Mission*, in IAU Symposium, Vol. 269, Galileo's Medicean Moons: Their Impact on 400 Years of Discovery, ed. C. Barbieri, S. Chakrabarti, M. Coradini, & M. Lazzarin, 92–100

Borucki, W. J., Koch, D., Jenkins, J., et al. 2009, *Kepler's Optical Phase Curve of the Exoplanet HAT-P-7b*, Science, 325, 709

Borucki, W. J., Koch, D. G., Basri, G., et al. 2011, *Characteristics of Planetary Candidates Observed by Kepler. II. Analysis of the First Four Months of Data*, ApJ, 736, 19

Boss, A. P. 1997, *Giant planet formation by gravitational instability.*, Science, 276, 1836

Bourrier, V., Kitzmann, D., Kuntzer, T., et al. 2019, *Optical phase curve of the ultra-hot Jupiter WASP-121b*, arXiv e-prints, arXiv:1909.03010

Brogi, M., de Kok, R. J., Albrecht, S., et al. 2016, *Rotation and Winds of Exoplanet HD 189733 b Measured with High-dispersion Transmission Spectroscopy*, ApJ, 817, 106

Brogi, M., de Kok, R. J., Birkby, J. L., Schwarz, H., & Snellen, I. A. G. 2014, *Carbon monoxide and water vapor in the atmosphere of the non-transiting exoplanet HD 179949 b*, A&A, 565, A124

Brogi, M., Giacobbe, P., Guilluy, G., et al. 2018, *Exoplanet atmospheres with GIANO. I. Water in the transmission spectrum of HD 189 733 b*, A&A, 615, A16

Brogi, M., Line, M., Bean, J., Désert, J. M., & Schwarz, H. 2017, *A Framework to Combine Low- and High-resolution Spectroscopy for the Atmospheres of Transiting Exoplanets*, ApJ, 839, L2

Brogi, M., Snellen, I. A. G., de Kok, R. J., et al. 2012, *The signature of orbital motion from the dayside of the planet τ Boötis b*, Nature, 486, 502

Brogi, M., Snellen, I. A. G., de Kok, R. J., et al. 2013, *Detection of Molecular Absorption in the Dayside of Exoplanet 51 Pegasi b?*, ApJ, 767, 27

Brown, T. M. 2001, *Transmission Spectra as Diagnostics of Extrasolar Giant Planet Atmospheres*, ApJ, 553, 1006

Bryson, S., Coughlin, J., Batalha, N. M., et al. 2020, *A Probabilistic Approach to Kepler Completeness and Reliability for Exoplanet Occurrence Rates*, The Astronomical Journal, 159, 279

Burrows, A., Budaj, J., & Hubeny, I. 2008, *Theoretical Spectra and Light Curves of Close-in Extrasolar Giant Planets and Comparison with Data*, ApJ, 678, 1436

Burrows, A., Marley, M., Hubbard, W. B., et al. 1997, *A Nongray Theory of Extrasolar Giant Planets and Brown Dwarfs*, ApJ, 491, 856

Burrows, A., Sudarsky, D., & Hubeny, I. 2006, *Theory for the Secondary Eclipse Fluxes, Spectra, Atmospheres, and Light Curves of Transiting Extrasolar Giant Planets*, ApJ, 650, 1140

Cabot, S. H. C., Madhusudhan, N., Welbanks, L., Piette, A., & Gandhi, S. 2020, *Detection of neutral atomic species in the ultra-hot jupiter WASP-121b*, arXiv e-prints, arXiv:2001.07196

Cartier, K. M. S., Beatty, T. G., Zhao, M., et al. 2017, *Near-infrared Emission Spectrum of WASP-103b Using Hubble Space Telescope/Wide Field Camera 3*, AJ, 153, 34

Casasayas-Barris, N., Pallé, E., Yan, F., et al. 2019, *Atmospheric characterization of the ultra-hot Jupiter MASCARA-2b/KELT-20b. Detection of CaII, FeII, NaI, and the Balmer series of H ($H\alpha$, $H\beta$, and $H\gamma$) with high-dispersion transit spectroscopy*, A&A, 628, A9

Castelli, F. & Kurucz, R. L. 2004, *Is missing Fe I opacity in stellar atmospheres a significant problem?*, A&A, 419, 725

Chabrier. 2014, *Giant Planet and Brown Dwarf Formation*, in Protostars and Planets VI, ed. H. Beuther, R. S. Klessen, C. P. Dullemond, & T. Henning, 619

Chandrasekhar, S. 1945a, *On the Continuous Absorption Coefficient of the Negative Hydrogen Ion*, ApJ, 102, 223

Chandrasekhar, S. 1945b, *On the Continuous Absorption Coefficient of the Negative Hydrogen Ion. II.*, ApJ, 102, 395

Charbonneau, D., Allen, L. E., Megeath, S. T., et al. 2005, *Detection of Thermal Emission from an Extrasolar Planet*, ApJ, 626, 523

Charbonneau, D., Brown, T. M., Noyes, R. W., & Gilliland, R. L. 2002, *Detection of an Extrasolar Planet Atmosphere*, ApJ, 568, 377

Collier Cameron, A., Bouchy, F., Hébrard, G., et al. 2007, *WASP-1b and WASP-2b: two new transiting exoplanets detected with SuperWASP and SOPHIE*, MNRAS, 375, 951

Cowan, N. B. & Agol, E. 2008, *Inverting Phase Functions to Map Exoplanets*, ApJ, 678, L129

Cowan, N. B. & Agol, E. 2011, *The Statistics of Albedo and Heat Recirculation on Hot Exoplanets*, ApJ, 729, 54

Cowan, N. B., Agol, E., & Charbonneau, D. 2007, *Hot nights on extrasolar planets: mid-infrared phase variations of hot Jupiters*, MNRAS, 379, 641

Cowan, N. B., Machalek, P., Croll, B., et al. 2012, *Thermal Phase Variations of WASP-12b: Defying Predictions*, ApJ, 747, 82

Cridland, A. J., Bosman, A. D., & van Dishoeck, E. F. 2020, *Impact of vertical gas accretion on the carbon-to-oxygen ratio of gas giant atmospheres*, A&A, 635, A68

Crossfield, I. J. M., Barman, T., Hansen, B. M. S., Tanaka, I., & Kodama, T. 2012, *Re-evaluating WASP-12b: Strong Emission at 2.315 μm, Deeper Occultations, and an Isothermal Atmosphere*, ApJ, 760, 140

Crossfield, I. J. M. & Kreidberg, L. 2017, *Trends in Atmospheric Properties of Neptune-size Exoplanets*, AJ, 154, 261

Dang, L., Cowan, N. B., Schwartz, J. C., et al. 2018, *Detection of a westward hotspot offset in the atmosphere of hot gas giant CoRoT-2b*, Nature Astronomy, 2, 220

Daylan, T., Günther, M. N., Mikal-Evans, T., et al. 2019, *TESS observations of the WASP-121 b phase curve*, arXiv e-prints, arXiv:1909.03000

de Kok, R. J., Brogi, M., Snellen, I. A. G., et al. 2013, *Detection of carbon monoxide in the high-resolution day-side spectrum of the exoplanet HD 189733b*, A&A, 554, A82

Deming, D., Brown, T. M., Charbonneau, D., Harrington, J., & Richardson, L. J. 2005, *A New Search for Carbon Monoxide Absorption in the Transmission Spectrum of the Extrasolar Planet HD 209458b*, ApJ, 622, 1149

Deming, D., Fraine, J. D., Sada, P. V., et al. 2012, *Infrared Eclipses of the Strongly Irradiated Planet WASP-33b, and Oscillations of Its Host Star*, ApJ, 754, 106

Deming, D., Harrington, J., Seager, S., & Richardson, L. J. 2006, *Strong Infrared Emission from the Extrasolar Planet HD 189733b*, ApJ, 644, 560

Deming, D., Wilkins, A., McCullough, P., et al. 2013, *Infrared Transmission Spectroscopy of the Exoplanets HD 209458b and XO-1b Using the Wide Field Camera-3 on the Hubble Space Telescope*, ApJ, 774, 95

Désert, J.-M., Bean, J., Miller-Ricci Kempton, E., et al. 2011a, *Observational Evidence for a Metal-rich Atmosphere on the Super-Earth GJ1214b*, ApJ, 731, L40

Désert, J.-M., Charbonneau, D., Demory, B.-O., et al. 2011b, *The Hot-Jupiter Kepler-17b: Discovery, Obliquity from Stroboscopic Starspots, and Atmospheric Characterization*, ApJS, 197, 14

Désert, J.-M., Charbonneau, D., Fortney, J. J., et al. 2011c, *The Atmospheres of the Hot-Jupiters Kepler-5b and Kepler-6b Observed during Occultations with Warm-Spitzer and Kepler*, ApJS, 197, 11

Désert, J.-M., Lecavelier des Etangs, A., Hébrard, G., et al. 2009, *Search for Carbon Monoxide in the Atmosphere of the Transiting Exoplanet HD 189733b*, ApJ, 699, 478

Désert, J. M., Vidal-Madjar, A., Lecavelier Des Etangs, A., et al. 2008, *TiO and VO broad band absorption features in the optical spectrum of the atmosphere of the hot-Jupiter <ASTROBJ>HD 209458b</ASTROBJ>*, A&A, 492, 585

Diamond-Lowe, H., Stevenson, K. B., Bean, J. L., Line, M. R., & Fortney, J. J. 2014, *New Analysis Indicates No Thermal Inversion in the Atmosphere of HD 209458b*, ApJ, 796, 66

Dobbs-Dixon, I., Cumming, A., & Lin, D. N. C. 2010, *Radiative Hydrodynamic Simulations of HD209458b: Temporal Variability*, ApJ, 710, 1395

Dressing, C. D. & Charbonneau, D. 2013, *The Occurrence Rate of Small Planets around Small Stars*, ApJ, 767, 95

Durisen, R. H., Boss, A. P., Mayer, L., et al. 2007, *Gravitational Instabilities in Gaseous Protoplanetary Disks and Implications for Giant Planet Formation*, in Protostars and Planets V, ed. B. Reipurth, D. Jewitt, & K. Keil, 607

Eistrup, C., Walsh, C., & van Dishoeck, E. F. 2018, *Molecular abundances and C/O ratios in chemically evolving planet-forming disk midplanes*, A&A, 613, A14

Espinoza, N., Rackham, B. V., Jordán, A., et al. 2019, *ACCESS: a featureless optical transmission spectrum for WASP-19b from Magellan/IMACS*, MNRAS, 482, 2065

Espinoza, N., Rackham, B. V., Jordán, A., et al. 2018, *ACCESS: a featureless optical transmission spectrum for WASP-19b from Magellan/IMACS*, Monthly Notices of the Royal Astronomical Society, 482, 2065–2087

Evans, T. M., Sing, D. K., Kataria, T., et al. 2017, *An ultrahot gas-giant exoplanet with a stratosphere*, Nature, 548, 58

Evans, T. M., Sing, D. K., Wakeford, H. R., et al. 2016, *Detection of H_2O and Evidence for TiO/VO in an Ultra-hot Exoplanet Atmosphere*, ApJ, 822, L4

Feng, Y. K., Line, M. R., Fortney, J. J., et al. 2016, *The Impact of Non-uniform Thermal Structure on the Interpretation of Exoplanet Emission Spectra*, ApJ, 829, 52

Foreman-Mackey, D. 2016, *corner.py: Scatterplot matrices in Python*, The Journal of Open Source Software, 1, 24

Foreman-Mackey, D., Hogg, D. W., Lang, D., & Goodman, J. 2013, *emcee: The MCMC Hammer*, Publications of the Astronomical Society of the Pacific, 125, 306–312

Fortney, J. J., Lodders, K., Marley, M. S., & Freedman, R. S. 2008, *A Unified Theory for the Atmospheres of the Hot and Very Hot Jupiters: Two Classes of Irradiated Atmospheres*, ApJ, 678, 1419

Fortney, J. J., Saumon, D., Marley, M. S., Lodders, K., & Freedman, R. S. 2006, *Atmosphere, Interior, and Evolution of the Metal-rich Transiting Planet HD 149026b*, ApJ, 642, 495

Freedman, R. S., Lustig-Yaeger, J., Fortney, J. J., et al. 2014, *Gaseous Mean Opacities for Giant Planet and Ultracool Dwarf Atmospheres over a Range of Metallicities and Temperatures*, ApJS, 214, 25

Freedman, R. S., Marley, M. S., & Lodders, K. 2008, *Line and Mean Opacities for Ultracool Dwarfs and Extrasolar Planets*, ApJS, 174, 504

Fromang, S., Leconte, J., & Heng, K. 2016, *Shear-driven instabilities and shocks in the atmospheres of hot Jupiters*, A&A, 591, A144

Fu, G., Deming, D., Knutson, H., et al. 2017, *Statistical Analysis of Hubble/WFC3 Transit Spectroscopy of Extrasolar Planets*, ApJ, 847, L22

Fulton, B. J., Petigura, E. A., Howard, A. W., et al. 2017, *The California-Kepler Survey. III. A Gap in the Radius Distribution of Small Planets*, AJ, 154, 109

Garhart, E. 2019, *Statistical Characterization of Hot Jupiter Atmospheres Using Spitzer's Secondary Eclipses*, Master's thesis, Arizona State University

Gaudi, B. S., Stassun, K. G., Collins, K. A., et al. 2017, *A giant planet undergoing extreme-ultraviolet irradiation by its hot massive-star host*, Nature, 546, 514–518

Gautier, D., Hersant, F., Mousis, O., & Lunine, J. I. 2001, *Enrichments in Volatiles in Jupiter: A New Interpretation of the Galileo Measurements*, ApJ, 550, L227

Gillon, M., Jehin, E., Lederer, S. M., et al. 2016, *Temperate Earth-sized planets transiting a nearby ultracool dwarf star*, Nature, 533, 221–224

Goodman, J. 2009, *Thermodynamics of Atmospheric Circulation on Hot Jupiters*, ApJ, 693, 1645

Gordon, S. & McBride, B. J. 1994, *Computer Program for Calculation of Complex Chemical Equilibrium Compositions and Applications. I. Analysis, Reference Publication RP-1311*

Gould, A., Dorsher, S., Gaudi, B. S., & Udalski, A. 2006, *Frequency of Hot Jupiters and Very Hot Jupiters from the OGLE-III Transit Surveys toward the Galactic Bulge and Carina*, Acta Astron., 56, 1

Grillmair, C. J., Charbonneau, D., Burrows, A., et al. 2007, *A Spitzer Spectrum of the Exoplanet HD 189733b*, ApJ, 658, L115

Guillot, T. & Hueso, R. 2006, *The composition of Jupiter: sign of a (relatively) late formation in a chemically evolved protosolar disc*, MNRAS, 367, L47

Haynes, K., Mandell, A. M., Madhusudhan, N., Deming, D., & Knutson, H. 2015, *Spectroscopic Evidence for a Temperature Inversion in the Dayside Atmosphere of Hot Jupiter WASP-33b*, ApJ, 806, 146

Helled, R. & Lunine, J. 2014, *Measuring Jupiter's water abundance by Juno: the link between interior and formation models*, MNRAS, 441, 2273

Hellier, C., Anderson, D. R., Collier Cameron, A., et al. 2009, *An orbital period of 0.94days for the hot-Jupiter planet WASP-18b*, Nature, 460, 1098

Helling, C., Gourbin, P., Woitke, P., & Parmentier, V. 2019a, *Sparkling nights and very hot days on WASP-18b: the formation of clouds and the emergence of an ionosphere*, A&A, 626, A133

Helling, C., Iro, N., Corrales, L., et al. 2019b, *Understanding the atmospheric properties and chemical composition of the ultra-hot Jupiter HAT-P-7b. I. Cloud and chemistry mapping*, A&A, 631, A79

Heng, K. 2012, *On the Existence of Shocks in Irradiated Exoplanetary Atmospheres*, ApJ, 761, L1

Herman, M. K., de Mooij, E. J. W., Jayawardhana, R., & Brogi, M. 2020, *Search for TiO and Optical Night-side Emission from the Exoplanet WASP-33b*, arXiv e-prints, arXiv:2006.10743

Hindle, A. W., Bushby, P. J., & Rogers, T. M. 2019, *Shallow-water Magnetohydrodynamics for Westward Hotspots on Hot Jupiters*, ApJ, 872, L27

Hoeijmakers, H. J., de Kok, R. J., Snellen, I. A. G., et al. 2015, *A search for TiO in the optical high-resolution transmission spectrum of HD 209458b: Hindrance due to inaccuracies in the line database*, A&A, 575, A20

Hoeijmakers, H. J., Ehrenreich, D., Heng, K., et al. 2018, *Atomic iron and titanium in the atmosphere of the exoplanet KELT-9b*, Nature, 560, 453

Hoeijmakers, H. J., Ehrenreich, D., Kitzmann, D., et al. 2019, *A spectral survey of an ultra-hot Jupiter. Detection of metals in the transmission spectrum of KELT-9 b*, A&A, 627, A165

Horne, K. 1986, *An optimal extraction algorithm for CCD spectroscopy.*, PASP, 98, 609

Howard, A. W., Marcy, G. W., Bryson, S. T., et al. 2012, *Planet Occurrence within 0.25 AU of Solar-type Stars from Kepler*, ApJS, 201, 15

HST. 2020, *HST Primer for Cycle 28*

Huang, X. & Cumming, A. 2012, *Ohmic Dissipation in the Interiors of Hot Jupiters*, ApJ, 757, 47

Hubeny, I., Burrows, A., & Sudarsky, D. 2003, *A Possible Bifurcation in Atmospheres of Strongly Irradiated Stars and Planets*, ApJ, 594, 1011

Huitson, C. M., Sing, D. K., Pont, F., et al. 2013, *An HST optical-to-near-IR transmission spectrum of the hot Jupiter WASP-19b: detection of atmospheric water and likely absence of TiO*, MNRAS, 434, 3252

Huitson, C. M., Sing, D. K., Vidal-Madjar, A., et al. 2012, *Temperature-pressure profile of the hot Jupiter HD 189733b from HST sodium observations: detection of upper atmospheric heating*, MNRAS, 422, 2477

Iro, N. & Maxted, P. 2013, *On the heat redistribution of the hot transiting exoplanet WASP-18b*, Icarus, 226, 1719–1723

Jen, C. K. 1933, *The Continuous Electron Affinity Spectrum of Hydrogen*, Phys. Rev., 43, 540

John, T. L. 1988, *Continuous absorption by the negative hydrogen ion reconsidered*, A&A, 193, 189

Johnson, T. V., Mousis, O., Lunine, J. I., & Madhusudhan, N. 2012, *Planetesimal Compositions in Exoplanet Systems*, ApJ, 757, 192

Kataria, T., Showman, A. P., Fortney, J. J., et al. 2015, *The Atmospheric Circulation of the Hot Jupiter WASP-43b: Comparing Three-dimensional Models to Spectrophotometric Data*, ApJ, 801, 86

Keating, D. & Cowan, N. B. 2017, *Revisiting the Energy Budget of WASP-43b: Enhanced Day-Night Heat Transport*, ApJ, 849, L5

Keating, D., Cowan, N. B., & Dang, L. 2019, *Uniformly hot nightside temperatures on short-period gas giants*, Nature Astronomy, 3, 1092

Kirkpatrick, J. D., Kelly, D. M., Rieke, G. H., et al. 1993, *M Dwarf Spectra from 0.6 to 1.5 Microns: A Spectral Sequence, Model Atmosphere Fitting, and the Temperature Scale*, ApJ, 402, 643

Kitzmann, D., Heng, K., Rimmer, P. B., et al. 2018, *The Peculiar Atmospheric Chemistry of KELT-9b*, ApJ, 863, 183

Knutson, H. A., Charbonneau, D., Allen, L. E., Burrows, A., & Megeath, S. T. 2008, *The 3.6-8.0 μm Broadband Emission Spectrum of HD 209458b: Evidence for an Atmospheric Temperature Inversion*, ApJ, 673, 526

Knutson, H. A., Charbonneau, D., Allen, L. E., et al. 2007, *A map of the day-night contrast of the extrasolar planet HD 189733b*, Nature, 447, 183

Knutson, H. A., Charbonneau, D., Cowan, N. B., et al. 2009, *Multiwavelength Constraints on the Day-Night Circulation Patterns of HD 189733b*, ApJ, 690, 822

Knutson, H. A., Howard, A. W., & Isaacson, H. 2010, *A Correlation Between Stellar Activity and Hot Jupiter Emission Spectra*, ApJ, 720, 1569

Knutson, H. A., Lewis, N., Fortney, J. J., et al. 2012, *3.6 and 4.5 μm Phase Curves and Evidence for Non-equilibrium Chemistry in the Atmosphere of Extrasolar Planet HD 189733b*, ApJ, 754, 22

Komacek, T. D. & Showman, A. P. 2016, *Atmospheric Circulation of Hot Jupiters: Dayside-Nightside Temperature Differences*, ApJ, 821, 16

Komacek, T. D., Showman, A. P., & Tan, X. 2017, *Atmospheric Circulation of Hot Jupiters: Dayside-Nightside Temperature Differences. II. Comparison with Observations*, ApJ, 835, 198

Komacek, T. D. & Tan, X. 2018, *Effects of Dissociation/Recombination on the Day-Night Temperature Contrasts of Ultra-hot Jupiters*, Research Notes of the American Astronomical Society, 2, 36

Kreidberg, L. 2015, *batman: BAsic Transit Model cAlculatioN in Python*, PASP, 127, 1161

Kreidberg, L., Bean, J. L., Désert, J.-M., et al. 2014a, *Clouds in the atmosphere of the super-Earth exoplanet GJ1214b*, Nature, 505, 69

Kreidberg, L., Bean, J. L., Désert, J.-M., et al. 2014b, *A Precise Water Abundance Measurement for the Hot Jupiter WASP-43b*, ApJ, 793, L27

Kreidberg, L., Line, M. R., Parmentier, V., et al. 2018, *Global Climate and Atmospheric Composition of the Ultra-hot Jupiter WASP-103b from HST and Spitzer Phase Curve Observations*, AJ, 156, 17

Lacis, A. A. & Oinas, V. 1991, *A description of the correlated-k distribution method for modelling nongray gaseous absorption, thermal emission, and multiple scattering in vertically inhomogeneous atmospheres*, J. Geophys. Res., 96, 9027

Leconte, J., Lai, D., & Chabrier, G. 2011a, *Distorted, non-spherical transiting planets: impact on the transit depth and on the radius determination (Corrigendum)*, A&A, 536, C1

Leconte, J., Lai, D., & Chabrier, G. 2011b, *Distorted, nonspherical transiting planets: impact on the transit depth and on the radius determination*, A&A, 528, A41

Lenzuni, P., Chernoff, D. F., & Salpeter, E. E. 1991, *Rosseland and Planck Mean Opacities of a Zero-Metallicity Gas*, ApJS, 76, 759

Li, J. & Goodman, J. 2010, *Circulation and Dissipation on Hot Jupiters*, ApJ, 725, 1146

Line, M. R. & Parmentier, V. 2016, *The Influence of Nonuniform Cloud Cover on Transit Transmission Spectra*, ApJ, 820, 78

Line, M. R., Wolf, A. S., Zhang, X., et al. 2013, *A Systematic Retrieval Analysis of Secondary Eclipse Spectra. I. A Comparison of Atmospheric Retrieval Techniques*, ApJ, 775, 137

Lissauer, J. J. 1993, *Planet formation.*, ARA&A, 31, 129

Lockwood, A. C., Johnson, J. A., Bender, C. F., et al. 2014, *Near-IR Direct Detection of Water Vapor in Tau Boötis b*, ApJ, 783, L29

Lodders, K. 2004, *Jupiter Formed with More Tar than Ice*, ApJ, 611, 587

Lodders, K. & Fegley, B. 2002, *Atmospheric Chemistry in Giant Planets, Brown Dwarfs, and Low-Mass Dwarf Stars. I. Carbon, Nitrogen, and Oxygen*, Icarus, 155, 393

Lodders, K., Palme, H., & Gail, H. P. 2009, *Abundances of the Elements in the Solar System*, Landolt Börnstein, 4B, 712

Longstaff, E. S., Casewell, S. L., Wynn, G. A., Maxted, P. F. L., & Helling, C. 2017, *Emission lines in the atmosphere of the irradiated brown dwarf WD0137-349B*, MNRAS, 471, 1728

Lothringer, J. D., Barman, T., & Koskinen, T. 2018, *Extremely Irradiated Hot Jupiters: Non-oxide Inversions, H^- Opacity, and Thermal Dissociation of Molecules*, ApJ, 866, 27

Madhusudhan, N. 2019, *Exoplanetary Atmospheres: Key Insights, Challenges, and Prospects*, ARA&A, 57, 617

Madhusudhan, N., Agúndez, M., Moses, J. I., & Hu, Y. 2016, *Exoplanetary Atmospheres—Chemistry, Formation Conditions, and Habitability*, Space Sci. Rev., 205, 285

Madhusudhan, N., Crouzet, N., McCullough, P. R., Deming, D., & Hedges, C. 2014, *H_2O Abundances in the Atmospheres of Three Hot Jupiters*, ApJ, 791, L9

Madhusudhan, N., Mousis, O., Johnson, T. V., & Lunine, J. I. 2011, *Carbon-rich Giant Planets: Atmospheric Chemistry, Thermal Inversions, Spectra, and Formation Conditions*, ApJ, 743, 191

Madhusudhan, N. & Redfield, S. 2015, *Optimal measures for characterizing water-rich super-Earths*, International Journal of Astrobiology, 14, 177

Mandell, A. M., Haynes, K., Sinukoff, E., et al. 2013, *Exoplanet Transit Spectroscopy Using WFC3: WASP-12 b, WASP-17 b, and WASP-19 b*, ApJ, 779, 128

Mansfield, M., Bean, J. L., Line, M. R., et al. 2018, *An HST/WFC3 Thermal Emission Spectrum of the Hot Jupiter HAT-P-7b*, AJ, 156, 10

Marboeuf, U., Mousis, O., Ehrenreich, D., et al. 2008, *Composition of Ices in Low-Mass Extrasolar Planets*, ApJ, 681, 1624

Marboeuf, U., Thiabaud, A., Alibert, Y., Cabral, N., & Benz, W. 2014, *From planetesimals to planets: volatile molecules*, A&A, 570, A36

Marcy, G. W. & Butler, R. P. 1996, *A Planetary Companion to 70 Virginis*, ApJ, 464, L147

Marley, M. S. & McKay, C. P. 1999, *Thermal Structure of Uranus' Atmosphere*, Icarus, 138, 268

Marley, M. S., Saumon, D., & Goldblatt, C. 2010, *A Patchy Cloud Model for the L to T Dwarf Transition*, ApJ, 723, L117

Martin, R. G. & Livio, M. 2012, *On the evolution of the snow line in protoplanetary discs*, Monthly Notices of the Royal Astronomical Society: Letters, 425, L6–L9

Maxted, P. F. L., Anderson, D. R., Doyle, A. P., et al. 2013, *Spitzer 3.6 and 4.5 μm full-orbit light curves of WASP-18*, MNRAS, 428, 2645

Mayor, M. & Queloz, D. 1995, *A Jupiter-mass companion to a solar-type star*, Nature, 378, 355

Mazeh, T. & Faigler, S. 2010, *Detection of the ellipsoidal and the relativistic beaming effects in the CoRoT-3 lightcurve*, A&A, 521, L59

Menou, K. 2012, *Magnetic Scaling Laws for the Atmospheres of Hot Giant Exoplanets*, ApJ, 745, 138

Ment, K., Dittmann, J. A., Astudillo-Defru, N., et al. 2019, *A Second Terrestrial Planet Orbiting the Nearby M Dwarf LHS 1140*, AJ, 157, 32

Merritt, S. R., Gibson, N. P., Nugroho, S. K., et al. 2020, *Non-detection of TiO and VO in the atmosphere of WASP-121b using high-resolution spectroscopy*

Mikal-Evans, T., Sing, D. K., Goyal, J. M., et al. 2019, *An emission spectrum for WASP-121b measured across the 0.8-1.1 μm wavelength range using the Hubble Space Telescope*, MNRAS, 488, 2222

Mikal-Evans, T., Sing, D. K., Kataria, T., et al. 2020, *Confirmation of water emission in the dayside spectrum of the ultrahot Jupiter WASP-121b*, MNRAS, 496, 1638

Miller, N., Fortney, J. J., & Jackson, B. 2009, *Inflating and Deflating Hot Jupiters: Coupled Tidal and Thermal Evolution of Known Transiting Planets*, ApJ, 702, 1413

Mollière, P., van Boekel, R., Dullemond, C., Henning, T., & Mordasini, C. 2015, *Model Atmospheres of Irradiated Exoplanets: The Influence of Stellar Parameters, Metallicity, and the C/O Ratio*, ApJ, 813, 47

Morton, T. D. & Swift, J. 2014, *The Radius Distribution of Planets around Cool Stars*, ApJ, 791, 10

Moses, J. I., Visscher, C., Fortney, J. J., et al. 2011, *Disequilibrium Carbon, Oxygen, and Nitrogen Chemistry in the Atmospheres of HD 189733b and HD 209458b*, ApJ, 737, 15

Mousis, O., Lunine, J. I., Madhusudhan, N., & Johnson, T. V. 2012, *Nebular Water Depletion as the Cause of Jupiter's Low Oxygen Abundance*, ApJ, 751, L7

Mousis, O., Lunine, J. I., Pasek, M., et al. 2009, *A primordial origin for the atmospheric methane of Saturn's moon Titan*, Icarus, 204, 749

Nugroho, S. K., Kawahara, H., Masuda, K., et al. 2017, *High-resolution Spectroscopic Detection of TiO and a Stratosphere in the Day-side of WASP-33b*, AJ, 154, 221

Nymeyer, S., Harrington, J., Hardy, R. A., et al. 2011, *Spitzer Secondary Eclipses of WASP-18b*, ApJ, 742, 35

Öberg, K. I., Murray-Clay, R., & Bergin, E. A. 2011, *The Effects of Snowlines on C/O in Planetary Atmospheres*, ApJ, 743, L16

Owen, T., Mahaffy, P., Niemann, H. B., et al. 1999, *A low-temperature origin for the planetesimals that formed Jupiter*, Nature, 402, 269

Page, T. L. 1939, *The continuous atomic absorption of light (Council report on the progress of astronomy)*, MNRAS, 99, 385

Pannekoek, A. 1930, *The theoretical contours of absorption lines*, MNRAS, 91, 139

Pannekoek, A. 1931, *The theoretical contours of absorption lines. (Second paper)*, MNRAS, 91, 519

Parmentier, V. & Crossfield, I. J. M. 2018, Exoplanet Phase Curves: Observations and Theory, 116

Parmentier, V., Fortney, J. J., Showman, A. P., Morley, C., & Marley, M. S. 2016, *Transitions in the Cloud Composition of Hot Jupiters*, ApJ, 828, 22

Parmentier, V., Guillot, T., Fortney, J. J., & Marley, M. S. 2015, *A non-grey analytical model for irradiated atmospheres. II. Analytical vs. numerical solutions*, A&A, 574, A35

Parmentier, V., Line, M. R., Bean, J. L., et al. 2018, *From thermal dissociation to condensation in the atmospheres of ultra hot Jupiters: WASP-121b in context*, A&A, 617, A110

Parmentier, V., Showman, A. P., & Lian, Y. 2013, *3D mixing in hot Jupiters atmospheres. I. Application to the day/night cold trap in HD 209458b*, A&A, 558, A91

Patra, K. C., Winn, J. N., Holman, M. J., et al. 2020, *The continuing search for evidence of tidal orbital decay of hot Jupiters*

Pepper, J., Kuhn, R. B., Siverd, R., James, D., & Stassun, K. 2012, *The KELT-South Telescope*, PASP, 124, 230

Pepper, J., Pogge, R. W., DePoy, D. L., et al. 2007, *The Kilodegree Extremely Little Telescope (KELT): A Small Robotic Telescope for Large-Area Synoptic Surveys*, PASP, 119, 923

Perez-Becker, D. & Showman, A. P. 2013, *Atmospheric Heat Redistribution on Hot Jupiters*, ApJ, 776, 134

Perna, R., Menou, K., & Rauscher, E. 2010a, *Magnetic Drag on Hot Jupiter Atmospheric Winds*, ApJ, 719, 1421

Perna, R., Menou, K., & Rauscher, E. 2010b, *Ohmic Dissipation in the Atmospheres of Hot Jupiters*, ApJ, 724, 313

Perri, F. & Cameron, A. G. W. 1974, *Hydrodynamic Instability of the Solar Nebula in the Presence of a Planetary Core*, Icarus, 22, 416

Petigura, E. A., Howard, A. W., & Marcy, G. W. 2013, *Prevalence of Earth-size planets orbiting Sun-like stars*, Proceedings of the National Academy of Science, 110, 19273

Petigura, E. A., Marcy, G. W., Winn, J. N., et al. 2018, *The California-Kepler Survey. IV. Metal-rich Stars Host a Greater Diversity of Planets*, AJ, 155, 89

Pino, L., Désert, J.-M., Brogi, M., et al. 2020, *Neutral Iron Emission Lines from the Dayside of KELT-9b: The GAPS Program with HARPS-N at TNG XX*, ApJ, 894, L27

Piskorz, D., Benneke, B., Crockett, N. R., et al. 2016, *Evidence for the Direct Detection of the Thermal Spectrum of the Non-Transiting Hot Gas Giant HD 88133 b*, ApJ, 832, 131

Piskorz, D., Benneke, B., Crockett, N. R., et al. 2017, *Detection of Water Vapor in the Thermal Spectrum of the Non-transiting Hot Jupiter Upsilon Andromedae b*, AJ, 154, 78

Pollacco, D. L., Skillen, I., Collier Cameron, A., et al. 2006, *The WASP Project and the SuperWASP Cameras*, PASP, 118, 1407

Pollack, J. B., Hubickyj, O., Bodenheimer, P., et al. 1996, *Formation of the Giant Planets by Concurrent Accretion of Solids and Gas*, Icarus, 124, 62

Rafikov, R. R. 2005, *Can Giant Planets Form by Direct Gravitational Instability?*, ApJ, 621, L69

Rafikov, R. R. 2006, *Atmospheres of Protoplanetary Cores: Critical Mass for Nucleated Instability*, ApJ, 648, 666

Rauscher, E. & Kempton, E. M. R. 2014, *The Atmospheric Circulation and Observable Properties of Non-synchronously Rotating Hot Jupiters*, ApJ, 790, 79

Rauscher, E. & Menou, K. 2010, *Three-dimensional Modeling of Hot Jupiter Atmospheric Flows*, ApJ, 714, 1334

Rauscher, E. & Menou, K. 2012, *The Role of Drag in the Energetics of Strongly Forced Exoplanet Atmospheres*, ApJ, 745, 78

Rodler, F., Lopez-Morales, M., & Ribas, I. 2012, *Weighing the Non-transiting Hot Jupiter τ Boo b*, ApJ, 753, L25

Rogers, T. M. 2017, *Constraints on the magnetic field strength of HAT-P-7 b and other hot giant exoplanets*, Nature Astronomy, 1, 0131

Rogers, T. M. & Komacek, T. D. 2014, *Magnetic Effects in Hot Jupiter Atmospheres*, ApJ, 794, 132

Santerne, A., Díaz, R. F., Moutou, C., et al. 2012, *SOPHIE velocimetry of Kepler transit candidates. VII. A false-positive rate of 35% for Kepler close-in giant candidates*, A&A, 545, A76

Schoonenberg, D. & Ormel, C. W. 2017, *Planetesimal formation near the snowline: in or out?*, A&A, 602, A21

Schwartz, J. C. & Cowan, N. B. 2015, *Balancing the energy budget of short-period giant planets: evidence for reflective clouds and optical absorbers*, MNRAS, 449, 4192

Schwartz, J. C., Kashner, Z., Jovmir, D., & Cowan, N. B. 2017, *Phase Offsets and the Energy Budgets of Hot Jupiters*, ApJ, 850, 154

Schwarz, H., Brogi, M., de Kok, R., Birkby, J., & Snellen, I. 2015, *Evidence against a strong thermal inversion in HD 209458b from high-dispersion spectroscopy*, A&A, 576, A111

Seager, S., Sasselov, D. D., & Scott, D. 1999, *A New Calculation of the Recombination Epoch*, ApJ, 523, L1

Sedaghati, E., Boffin, H. M. J., MacDonald, R. J., et al. 2017, *Detection of titanium oxide in the atmosphere of a hot Jupiter*, Nature, 549, 238

Sestovic, M., Demory, B.-O., & Queloz, D. 2018, *Investigating hot-Jupiter inflated radii with hierarchical Bayesian modelling*, A&A, 616, A76

Sharp, C. M. & Burrows, A. 2007, *Atomic and Molecular Opacities for Brown Dwarf and Giant Planet Atmospheres*, ApJS, 168, 140

Sheppard, K. B., Mandell, A. M., Tamburo, P., et al. 2017, *Evidence for a Dayside Thermal Inversion and High Metallicity for the Hot Jupiter WASP-18b*, ApJ, 850, L32

Showman, A. P., Cooper, C. S., Fortney, J. J., & Marley, M. S. 2008, *Atmospheric Circulation of Hot Jupiters: Three-dimensional Circulation Models of HD 209458b and HD 189733b with Simplified Forcing*, ApJ, 682, 559

Showman, A. P., Fortney, J. J., Lian, Y., et al. 2009, *Atmospheric Circulation of Hot Jupiters: Coupled Radiative-Dynamical General Circulation Model Simulations of HD 189733b and HD 209458b*, ApJ, 699, 564

Showman, A. P. & Guillot, T. 2002, *Atmospheric circulation and tides of "51 Pegasus b-like" planets*, A&A, 385, 166

Showman, A. P. & Polvani, L. M. 2011, *Equatorial Superrotation on Tidally Locked Exoplanets*, ApJ, 738, 71

Shporer, A., Wong, I., Huang, C. X., et al. 2019, *TESS Full Orbital Phase Curve of the WASP-18b System*, AJ, 157, 178

Silburt, A., Gaidos, E., & Wu, Y. 2015, *A Statistical Reconstruction of the Planet Population around Kepler Solar-type Stars*, ApJ, 799, 180

Sing, D. K., Fortney, J. J., Nikolov, N., et al. 2016, *A continuum from clear to cloudy hot-Jupiter exoplanets without primordial water depletion*, Nature, 529, 59

Sing, D. K., Lecavelier des Etangs, A., Fortney, J. J., et al. 2013, *HST hot-Jupiter transmission spectral survey: evidence for aerosols and lack of TiO in the atmosphere of WASP-12b*, MNRAS, 436, 2956

Snellen, I. A. G., de Kok, R. J., de Mooij, E. J. W., & Albrecht, S. 2010, *The orbital motion, absolute mass and high-altitude winds of exoplanet HD209458b*, Nature, 465, 1049

Snellen, I. A. G., de Mooij, E. J. W., & Albrecht, S. 2009, *The changing phases of extrasolar planet CoRoT-1b*, Nature, 459, 543

Snellen, I. A. G., Stuik, R., Navarro, R., et al. 2012, Society of Photo-Optical Instrumentation Engineers (SPIE) Conference Series, Vol. 8444, Ground-based search for the brightest transiting planets with the Multi-site All-Sky CAmeRA: MASCARA, 84440I

Southworth, J. 2011, *Homogeneous studies of transiting extrasolar planets - IV. Thirty systems with space-based light curves*, MNRAS, 417, 2166

Southworth, J., Hinse, T. C., Dominik, M., et al. 2009, *Physical Properties of the 0.94-Day Period Transiting Planetary System WASP-18*, ApJ, 707, 167

Southworth, J., Mancini, L., Ciceri, S., et al. 2015, *High-precision photometry by telescope defocusing - VII. The ultrashort period planet WASP-103*, MNRAS, 447, 711

Spiegel, D. S., Silverio, K., & Burrows, A. 2009, *Can TiO Explain Thermal Inversions in the Upper Atmospheres of Irradiated Giant Planets?*, ApJ, 699, 1487

Stevenson, K. B. 2020, *A New Method for Studying Exoplanet Atmospheres Using Planetary Infrared Excess*, ApJ, 898, L35

Stevenson, K. B., Bean, J. L., Madhusudhan, N., & Harrington, J. 2014a, *Deciphering the Atmospheric Composition of WASP-12b: A Comprehensive Analysis of its Dayside Emission*, ApJ, 791, 36

Stevenson, K. B., Bean, J. L., Seifahrt, A., et al. 2014b, *Transmission Spectroscopy of the Hot Jupiter WASP-12b from 0.7 to 5 μm*, AJ, 147, 161

Stevenson, K. B., Désert, J.-M., Line, M. R., et al. 2014c, *Thermal structure of an exoplanet atmosphere from phase-resolved emission spectroscopy*, Science, 346, 838

Stevenson, K. B. & Fowler, J. 2019, *Analyzing Eight Years of Transiting Exoplanet Observations Using WFC3's Spatial Scan Monitor*, Space Telescope WFC Instrument Science Report

Stevenson, K. B., Line, M. R., Bean, J. L., et al. 2017, *Spitzer Phase Curve Constraints for WASP-43b at 3.6 and 4.5 μm*, AJ, 153, 68

Sudarsky, D., Burrows, A., & Pinto, P. 2000, *Albedo and Reflection Spectra of Extrasolar Giant Planets*, ApJ, 538, 885

Swain, M., Deroo, P., Tinetti, G., et al. 2013, *Probing the extreme planetary atmosphere of WASP-12b*, Icarus, 225, 432

Swain, M. R., Vasisht, G., & Tinetti, G. 2008, *The presence of methane in the atmosphere of an extrasolar planet*, Nature, 452, 329

Tan, X. & Komacek, T. D. 2019, *The Atmospheric Circulation of Ultra-hot Jupiters*, ApJ, 886, 26

Thorngren, D. P. & Fortney, J. J. 2018, *Bayesian Analysis of Hot-Jupiter Radius Anomalies: Evidence for Ohmic Dissipation?*, AJ, 155, 214

Tinetti, G., Vidal-Madjar, A., Liang, M.-C., et al. 2007, *Water vapour in the atmosphere of a transiting extrasolar planet*, Nature, 448, 169

Toomre, A. 1964, *On the gravitational stability of a disk of stars.*, ApJ, 139, 1217

Toon, O. B., McKay, C. P., Ackerman, T. P., & Santhanam, K. 1989, *Rapid calculation of radiative heating rates and photodissociation rates in inhomogeneous multiple scattering atmospheres*, J. Geophys. Res., 94, 16287

Torres, G., Fischer, D. A., Sozzetti, A., et al. 2012, *Improved Spectroscopic Parameters for Transiting Planet Hosts*, ApJ, 757, 161

Triaud, A. H. M. J., Gillon, M., Ehrenreich, D., et al. 2015, *WASP-80b has a dayside within the T-dwarf range*, MNRAS, 450, 2279

Tsai, S.-M., Kitzmann, D., Lyons, J. R., et al. 2018, *Toward Consistent Modeling of Atmospheric Chemistry and Dynamics in Exoplanets: Validation and Generalization of the Chemical Relaxation Method*, ApJ, 862, 31

Tsiaras, A., Waldmann, I. P., Rocchetto, M., et al. 2016, *A New Approach to Analyzing HST Spatial Scans: The Transmission Spectrum of HD 209458 b*, ApJ, 832, 202

Tsiaras, A., Waldmann, I. P., Tinetti, G., Tennyson, J., & Yurchenko, S. N. 2019, *Water vapour in the atmosphere of the habitable-zone eight-Earth-mass planet K2-18 b*, Nature Astronomy, 3, 1086

Turner, J. D., de Mooij, E. J. W., Jayawardhana, R., et al. 2020, *Detection of Ionized Calcium in the Atmosphere of the Ultra-hot Jupiter KELT-9b*, ApJ, 888, L13

Unsold, A. 1938, Physik der sternamospharen, MIT besonderer berucksichtigung der sonne

Vidal-Madjar, A., Lecavelier des Etangs, A., Désert, J. M., et al. 2003, *An extended upper atmosphere around the extrasolar planet HD209458b*, Nature, 422, 143

Visscher, C., Lodders, K., & Fegley, Bruce, J. 2006, *Atmospheric Chemistry in Giant Planets, Brown Dwarfs, and Low-Mass Dwarf Stars. II. Sulfur and Phosphorus*, ApJ, 648, 1181

Wakeford, H. R. & Sing, D. K. 2015, *Transmission spectral properties of clouds for hot Jupiter exoplanets*, A&A, 573, A122

Wakeford, H. R., Sing, D. K., Evans, T., Deming, D., & Mandell, A. 2016, *Marginalizing Instrument Systematics in HST WFC3 Transit Light Curves*, ApJ, 819, 10

Walsh, K. J., Morbidelli, A., Raymond, S. N., O'Brien, D. P., & Mandell, A. M. 2011, *A low mass for Mars from Jupiter's early gas-driven migration*, Nature, 475, 206–209

Wildt, R. 1939, *Negative Ions of Hydrogen and the Opacity of Stellar Atmospheres.*, ApJ, 90, 611

Wilkins, A. N., Delrez, L., Barker, A. J., et al. 2017, *Searching for Rapid Orbital Decay of WASP-18b*, ApJ, 836, L24

Wong, I., Knutson, H. A., Kataria, T., et al. 2016, *3.6 and 4.5 μm Spitzer Phase Curves of the Highly Irradiated Hot Jupiters WASP-19b and HAT-P-7b*, ApJ, 823, 122

Wong, I., Knutson, H. A., Lewis, N. K., et al. 2015, *3.6 and 4.5 μm Phase Curves of the Highly Irradiated Eccentric Hot Jupiter WASP-14b*, ApJ, 811, 122

Wright, J. T., Marcy, G. W., Howard, A. W., et al. 2012, *The Frequency of Hot Jupiters Orbiting nearby Solar-type Stars*, ApJ, 753, 160

Yadav, R. K. & Thorngren, D. P. 2017, *Estimating the Magnetic Field Strength in Hot Jupiters*, ApJ, 849, L12

Yan, F., Casasayas-Barris, N., Molaverdikhani, K., et al. 2019, *Ionized calcium in the atmospheres of two ultra-hot exoplanets WASP-33b and KELT-9b*, A&A, 632, A69

Youdin, A. N. & Mitchell, J. L. 2010, *The Mechanical Greenhouse: Burial of Heat by Turbulence in Hot Jupiter Atmospheres*, ApJ, 721, 1113

Zellem, R. T., Lewis, N. K., Knutson, H. A., et al. 2014, *The 4.5 μm Full-orbit Phase Curve of the Hot Jupiter HD 209458b*, ApJ, 790, 53

Zhang, M., Knutson, H. A., Kataria, T., et al. 2018, *Phase Curves of WASP-33b and HD 149026b and a New Correlation between Phase Curve Offset and Irradiation Temperature*, AJ, 155, 83

Zhou, Y., Apai, D., Lew, B. W. P., & Schneider, G. 2017, *A Physical Model-based Correction for Charge Traps in the Hubble Space Telescope's Wide Field Camera 3 Near-IR Detector and Its Applications to Transiting Exoplanets and Brown Dwarfs*, AJ, 153, 243

Zhu, X., Talaat, E. R., Baker, J. B. H., & Yee, J.-H. 2005, *A self-consistent derivation of ion drag and Joule heating for atmospheric dynamics in the thermosphere*, Annales Geophysicae, 23, 3313

Publications

Here are listed the publications included in this thesis. The relative contribution of every coauthor is represented by their place in the author list.

Chapter 2: H- Opacity and Water Dissociation in the Dayside Atmosphere of the Very Hot Gas Giant WASP-18b
Astrophysical Journal Letters, 2018, Volume 855 Number 2, L30
J. Arcangeli, J.-M. Désert, M. R. Line, J. L. Bean, V. Parmentier, K. B. Stevenson, L. Kreidberg, J. J. Fortney, M. Mansfield, A. P. Showman

Chapter 3: Climate of an Ultra Hot Jupiter: Spectroscopic phase curve of WASP-18b with HST/WFC3
Astronomy & Astrophysics, 2019, Volume 625, A136
J. Arcangeli, J.-M. Désert, V. Parmentier, K. B. Stevenson, J. L. Bean, M. R. Line, L. Kreidberg, J. J. Fortney, A. P. Showman

Chapter 4: A new approach to spectroscopic phase curves: The emission spectrum of WASP-12b observed in quadrature with HST/WFC3
submitted to Astronomy & Astrophysics
J. Arcangeli, J.-M. Désert, V. Parmentier, S.-M. Tsai, K. B. Stevenson

Chapter 5: The brightness temperature of the nightside of WASP-18b
in preparation
J.-M. Désert, **J. Arcangeli**

Nederlandse samenvatting

In deze thesis gebruik ik waarnemingen van de HST/WFC3 en Spitzer in het nabij-infrarood om de atmosferen van ultra-hete Jupiters te meten en te karakteriseren. Ik beschrijf het eerste voorbeeld van een ultra-hete Jupiter met een uitleg van zijn chemische processen in hoofdstuk 2. In dit hoofdstuk observeren we het spectrum van de thermische emissie van de dagzijde van WASP-18b, en bevinden we dat eerdere pogingen om deze en vergelijkbare hete objecten te modelleren enkele belangrijke processen missen. Wij hebben deze effecten toegevoegd in onze modellen, om precies te zijn: het effect van de dissociatie van moleculen zoals water en TiO en de ondoorzichtigheid in het continuüm dat wordt veroorzaakt door het negatieve waterstof ion H-. We bevinden dat we de waarnemingen kunnen evenaren met een model van een atmosfeer met een compositie vergelijkbaar met die van de zon, in lijn met koudere gasreuzen.

In hoofdstuk 3 zetten we onze studie van WASP-18b voort met een observatie van alle schijngestalten in het nabij-infrarood met HST/WFC3. We nemen een groot dag-nacht contrast waar wat duidt op zeer slechte atmosferische circulatie. We bemerken dat de helderheid van de nachtzijde lager is dan onze detectielimieten doordat de temperatuur zo laag is en door de onzekerheden die de langetermijn systematiek van de instrumenten met zich meebrengen. Dit wordt verergerd door ellipsvormige variaties in de ster teweeggebracht door het zwaartekrachtsveld van de planeet. Het bewijs dat we hiervoor vinden, bevestigt onafhankelijke waarnemingen van de TESS satelliet in het zichtbare deel van het spectrum. We vergelijken onze resultaten met circulatiemodellen van de atmosfeer en vinden dat we wederom extra natuurkunde nodig hebben om de data te verklaren, in dit geval door een atmosferische weerstand toe te voegen. We bekijken wat de oorzaak van zulk een weerstand zou kunnen zijn en we ontdekken dat het consequent is met een weerstand op de geïoniseerde winden geïnduceerd door de Lorentzkracht in een Jupiter-achtig magnetisch veld.

Hoofdstuk vier beschrijft een nieuwe techniek die we hebben ontwikkeld voor het analyseren van spectroscopische schijngestaltedata. Deze techniek zorgt ervoor dat we oude, voorheen ongepubliceerde spectra van WASP-12b, nog een UHJ, konden gebruiken; van deze planeet was enkel een paar fases waargenomen. Hiermee hebben we de eerste limieten op het klimaat van WASP-12b verkregen. Ook bekijken we hoe onze nieuwe techniek in de toekomst gebruikt kan worden om onvolledige schijngestaltedata waar te nemen.

Uiteindelijk gebruiken we onze nieuwe techniek in hoofdstuk vijf voor de data met schijngestalten van WASP-18b, die we in hoofdstukken 2 en 3 hebben gebruikt. Hiermee tonen we aan dat we de spectra van verschillende schijngestalten kunnen waarnemen en ook de thermische veranderingen van de planeet. Deze nieuwe extractie onthult spectrale variaties die nog niet eerder toegankelijk waren met de klassieke methoden.

Acknowledgements

I have been in a very privileged position to start and finish a doctorate in Astronomy. There is no chance that I would have reached the end without all of the help I have had along the way, from every direction, and for that I am very thankful.

Firstly I would like to thank Jean-Michel for offering me this opportunity in the first place. I'm not sure I did too convincing a job of selling myself in my application, but you invited me to interview (which was a pretty cool process itself) and finally offered me the position. It has been a lot of fun seeing the evolution of this group, which has now grown to become a force of its own. I've learned so much from working with you on papers, proposals, and talks that I know will help me in all my future challenges. I wish you all the best with the puzzles astronomy will continue to present; you have built an amazing group that will no doubt be at the forefront of exoplanets for many years to come.

Speaking of which I want to acknowledge all of the members of our group, because you have all provided a fantastic atmosphere and helped me along my path in your own ways. Thanks to Kamen, for the sage advice and wealth of knowledge you shared with us all. Thanks to Lorenzo, for dragging a few words of Italian out of me, for your expertise, and for your infectious energy for new problems. Claire, thanks for all the support over the years, you are in touching distance now! Thanks Vatsal for keeping me up-to-date with everything in astronomy, gossip or otherwise. Bob, you've put up with my code with hardly a complaint despite literally fixing it, so that deserves a thanks, and thanks Niloo for being so enthusiastic that I can't help but smile. I will miss this group a lot, so I hope we can stay in touch.

Carsten, I want to thank you for being such a stable support. I know I didn't use you as much as I should but I am grateful for all the help that you gave. Thanks to all the members of the Cookie meeting (as it should be remembered), or the Exoplanets and Disks meeting to be specific. It was always great to hear your opinions and updates, and I learned a lot from all of you, new and old members alike.

I'd like to also thank the committee for reading and commenting on my thesis, whatever those comments might be. I'm very lucky to have such an array of distinguished researchers assess my work.

I'm not quite sure how to thank the conference organisers that have run all the schools and conferences that I attended throughout my PhD, but I'd like to do so. Those experiences really helped motivate me, and I met a lot of great people and collaborators over the years.

Of course my thesis is hardly all my own work, and I owe a great deal of thanks to all my collaborators who worked so hard on each of their contributions. Thanks to Vivien and Mike whose models really are the backbone of this thesis. Thanks also to Jacob, Kevin, Laura, Jonathan, Adam, Shami, and Christiane for lending me their brains and ears. Thanks to those at API who I have not yet thanked as well, including Susan and Renee for dealing with just about every problem that comes up, Milena in particular for your guiding hand when first moving over to Amsterdam, and Martin for tackling every IT problem I came across.

Finally thanks to my family for getting me to this point. I know you all enjoyed the excuse to visit Amsterdam, and it was great to have you. I hope that the considerable effort you put into my education has paid off. Thanks Helen of course, for making this whole adventure a lot of fun. Every step of this journey has been made easy thanks to you. On to the next one!